LUND UNIVERSITY

Spectroscopy along Decay Chains of Element 114, Flerovium

Såmark-Roth, Anton

2021

Document Version:
Publisher's PDF, also known as Version of record

Link to publication

Citation for published version (APA):
Såmark-Roth, A. (2021). *Spectroscopy along Decay Chains of Element 114, Flerovium*. Lund University.

Total number of authors:
1

LUND UNIVERSITY

PO Box 117
221 00 Lund
+46 46-222 00 00

Spectroscopy along Decay Chains of Element 114, Flerovium

ANTON SÅMARK-ROTH | DEPARTMENT OF PHYSICS | LUND UNIVERSITY

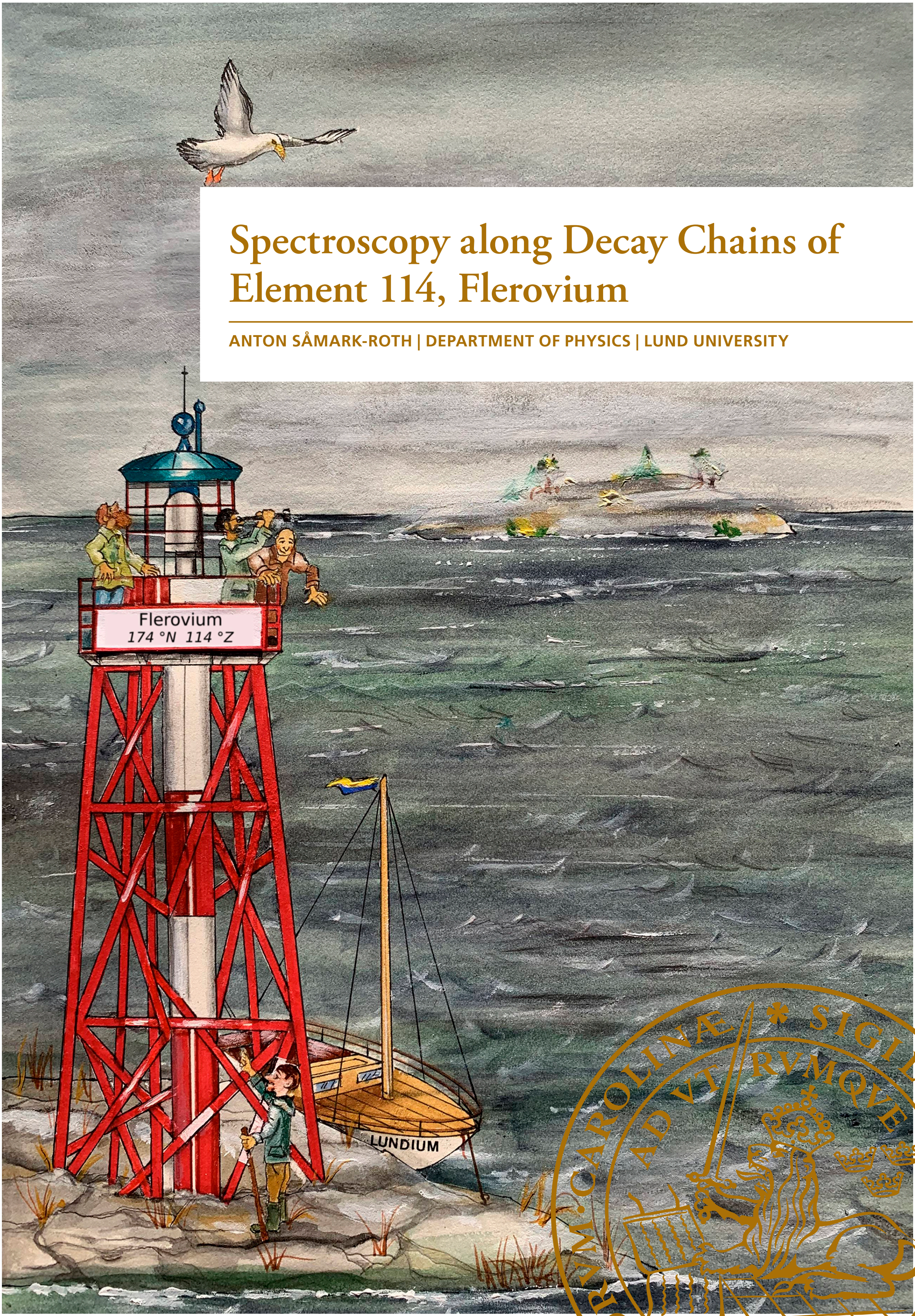

Spectroscopy along Decay Chains of Element 114, Flerovium

by Anton Såmark-Roth

LUND
UNIVERSITY

Dissertation for the degree of
Doctor of Philosophy

Thesis advisors: Prof. Dirk Rudolph, Dr. Luis G. Sarmiento Pico

Faculty opponent: Prof. Piet Van Duppen

Academic dissertation which, by due permission of the Faculty of Science at Lund University, will be publicly defended on Friday, the 18th of June 2021 at 13:15 in the Rydberg lecture hall (Rydbergssalen) at the Department of Physics, Sölvegatan 14 A, Lund, for the degree of Doctor of Philosophy.

Organization
LUND UNIVERSITY
Department of Physics
Box 118, SE–221 00 LUND
Sweden

Document name
DOCTORAL DISSERTATION

Date of disputation
2021-06-18

Sponsoring organization

Author(s)
Anton Såmark-Roth

Title and subtitle
Spectroscopy along Decay Chains of Element 114, Flerovium

Abstract

This thesis focusses on a nuclear spectroscopy experiment conducted to study α-decay chains stemming from isotopes of flerovium (element $Z = 114$). An upgraded TASISpec decay station was placed behind the gas-filled separator TASCA at the GSI Helmholtzzentrum für Schwerionenforschung in Darmstadt, Germany. The fusion-evaporation reactions ^{48}Ca + ^{242}Pu and ^{48}Ca + ^{244}Pu provided a total of 29 flerovium decay chains. The measurement of two new types of even-even flerovium decay chains, starting from ^{286}Fl and ^{288}Fl, respectively, marked the discoveries of (i) an excited state in ^{282}Cn and (ii) the isotope ^{280}Ds. The observations gave further insights into the location of the coveted Island of Stability. With fifteen new decay chains starting from ^{289}Fl, the global data set was doubled for this isotope. Measured decay properties of these chains could provide new evidence of α-decay fine structure of odd-A superheavy nuclei, as predicted by theoretical calculations.

The papers included in this thesis cover various aspects of the flerovium experiment. The chapters complement the publications with background information and further details. They include an introduction to the research field of superheavy nuclei, detector development efforts, a description of the experimental setup as well as information on the data analysis and the simulations performed. The chapters also provide a summary of the main results and overarching outlook perspectives.

In Paper I, the processing of digitised silicon preamplifier signals were applied to short-lived α-decaying nuclei North-East of Pb. Further preparatory aspects of the experiment as well as applied spectroscopic tools, are covered in Paper III. The TASISpec decay station was upgraded with novel Compex germanium detectors, and their characterisation is given in Paper II. Paper V presents detailed information on the data analysis and statistical assessments applied to the flerovium decay chains. Highlights from the even-even Fl-decay chains are presented in Paper IV and as a press release in Paper VII. Finally, the main findings of the odd-A, ^{289}Fl, decay chains form Paper VI.

Key words
Superheavy elements, flerovium, nuclear structure, spectroscopy, alpha decay, electromagnetic decay, spontaneous fission, germanium detectors

Classification system and/or index terms (if any)

Supplementary bibliographical information

Language
English

ISSN and key title

ISBN
978-91-7895-835-1 (print)
978-91-7895-836-8 (pdf)

Recipient's notes

Number of pages
222

Price

Security classification

I, the undersigned, being the copyright owner of the abstract of the above-mentioned dissertation, hereby grant to all reference sources the permission to publish and disseminate the abstract of the above-mentioned dissertation.

Signature

Date 2021-05-06

Spectroscopy along Decay Chains of Element 114, Flerovium

by Anton Såmark-Roth

LUND
UNIVERSITY

A doctoral thesis at a university in Sweden takes either the form of a single, cohesive research study (monograph) or a summary of research papers (compilation thesis), which the doctoral student has written alone or together with one or several other author(s).

In the latter case the thesis consists of two parts. An introductory text puts the research work into context and summarizes the main points of the papers. Then, the research publications themselves are reproduced, together with a description of the individual contributions of the authors. The research papers may either have been already published or are manuscripts at various stages (in press, submitted, or in draft).

Cover illustration front: Captain Didrik along with the crew members Anders, Dan-Åke and Peter glance toward the Island of Stability at the end of *Expedition Flerovium.* Art by Sverker Holmberg.

Cover illustration back: The Chart of Nuclides featured in *Expedition Flerovium.*

Funding information: This work is supported by the Knut and Alice Wallenberg foundation (KAW 2015.0021), in part by the Swedish Research Council (Vetenskapsrådet, VR 2016-3969), and the Royal Physiographic Society in Lund.

Faculty of Science, Department of Physics

ISBN: 978-91-7895-835-1 (print)
ISBN: 978-91-7895-836-8 (pdf)

Printed in Sweden by Media-Tryck, Lund University, Lund 2021

Till
Mamma och Pappa

Contents

2 Background

3 Detector Development

4 Experiment

5 Data Analysis and Simulations

Author's contributions

Contributions are listed according to the CRediT authorship contribution statements.

Publications included in this thesis

Paper I

Low-lying states in ^{219}Ra and ^{215}Rn: sampling microsecond α-decaying nuclei

A. Såmark-Roth, L.G. Sarmiento, D. Rudolph, J. Ljungberg, B.G. Carlsson, C. Fahlander, U. Forsberg, P. Golubev, I. Ragnarsson, D. Ackermann, L.-L. Andersson, M. Block, H. Brand, D.M. Cox, A. Di Nitto, Ch.E. Düllmann, K. Eberhardt, J. Even, J.M. Gates, J. Gerl, K.E. Gregorich, C.J. Gross, R.-D. Herzberg, F.P. Heßberger, E. Jäger, J. Khuyagbaatar, B. Kindler, I. Kojouharov, J.V. Kratz, J. Krier, N. Kurz, B. Lommel, A. Mistry, C. Mokry, J.P. Omtvedt, P. Papadakis, J. Runke, K. Rykaczewski, M. Schädel, H. Schaffner, B. Schausten, P. Thörle-Pospiech, N. Trautmann, T. Torres, A. Türler, A. Ward, N. Wiehl, and A. Yakushev

Phys. Rev. C **98**, 044307 (2018).
DOI: 10.1103/PhysRevC.98.044307

A. Såmark-Roth: Software, Formal analysis, Validation, Visualization, Writing - original draft, Writing - review & editing

Paper II

Compex: a cubic germanium detector

A. Såmark-Roth, D.M. Cox, J. Eberth, P. Golubev, D. Rudolph, L.G. Sarmiento, G. Tocabens, M. Ginsz, B. Pirard, and P. Quirin

Eur. Phys. J A **56**, 141 (2020).
DOI: 10.1140/epja/s10050-020-00155-3

A. Såmark-Roth: Conceptualization, Supervision, Project administration, Resources, Software, Investigation, Formal analysis, Validation, Visualization, Writing - original draft, Writing - review & editing

Paper III

Spectroscopic Tools Applied to Flerovium Decay Chains

D.M. Cox, **A. Såmark-Roth**, D. Rudolph, L.G. Sarmiento, C. Fahlander, U. Forsberg, P. Golubev, J.A.M. Heery, A. Yakushev, H. M. Albers, M. Block, H. Brand, R.M. Clark, Ch.E. Düllmann, J. Eberth, J.M. Gates, F. Giacoppo, M. Götz, S. Götz, R.-D. Herzberg, E. Jäger, B. Kindler, J. Khuyagbaatar, I. Kojouharov, J.V. Kratz, J. Krier, N. Kurz, L. Lens, B. Lommel, A. Mistry, C.-C. Meyer, C. Mokry, P. Papadakis, J.L. Pore, J. Runke, P. Thörle-Pospiech, N. Trautmann, H, Schaffner, B. Schausten, and J. Uusitalo

J. Phys. Conf. Ser. **1643** 012125 (2020).
DOI: 10.1088/1742-6596/1643/1/012125

A. Såmark-Roth: Project administration, Software, Investigation, Formal analysis, Validation, Visualization, Writing - original draft, Writing - review & editing

Paper IV

Spectroscopy along Flerovium Decay Chains: Discovery of ^{280}Ds and an Excited State in ^{282}Cn

A. Såmark-Roth, D.M. Cox, D. Rudolph, L.G. Sarmiento, B.G. Carlsson, J.L. Egido, P. Golubev, J. Heery, A. Yakushev, S. Åberg, H.M. Albers, M. Albertsson, M. Block, H. Brand, T. Calverley, R. Cantemir, R.M. Clark, Ch.E. Düllmann, J. Eberth, C. Fahlander, U. Forsberg, J.M. Gates, F. Giacoppo, M. Götz, S. Götz, R.-D. Herzberg, Y. Hrabar, E. Jäger, D. Judson, J. Khuyagbaatar, B. Kindler, I. Kojouharov, J.V. Kratz, J. Krier, N. Kurz, L. Lens, J. Ljungberg, B. Lommel, J. Louko, C.-C. Meyer, A. Mistry, C. Mokry, P. Papadakis, E. Parr, J.L. Pore, I. Ragnarsson, J. Runke, M. Schädel, H. Schaffner, B. Schausten, D.A. Shaughnessy, P. Thörle-Pospiech, N. Trautmann, and J. Uusitalo

Phys. Rev. Lett. **126**, 032503 (2021).
DOI: 10.1103/PhysRevLett.126.032503
Editor's Suggestion & Featured in Physics

A. Såmark-Roth: Project administration, Software, Investigation, Formal analysis, Validation, Writing - review & editing

Paper V

Spectroscopy along Flerovium Decay Chains

A. Såmark-Roth, D.M. Cox, D. Rudolph, L.G. Sarmiento, B.G. Carlsson, J.L. Egido, P. Golubev, J. Heery, A. Yakushev, S. Åberg, H.M. Albers, M. Albertsson, M. Block, H. Brand, T. Calverley, R. Cantemir, R.M. Clark, Ch.E. Düllmann, J. Eberth, C. Fahlander, U. Forsberg, J.M. Gates, F. Giacoppo, M. Götz, S. Götz, R.-D. Herzberg, Y. Hrabar, E. Jäger, D. Judson, J. Khuyagbaatar, B. Kindler, I. Kojouharov, J.V. Kratz, J. Krier, N. Kurz, L. Lens, J. Ljungberg, B. Lommel, J. Louko, C.-C. Meyer, A. Mistry, C. Mokry, P. Papadakis, E. Parr, J.L. Pore, I. Ragnarsson, J. Runke, M. Schädel, H. Schaffner, B. Schausten, D.A. Shaughnessy, P. Thörle-Pospiech, N. Trautmann, and J. Uusitalo

Manuscript to be submitted to Phys. Rev. C. It has not yet been subject to internal revision of the co-authors. Once published accessible via hyperlink Paper V in pdf version.

A. Såmark-Roth: Project administration, Software, Investigation, Formal analysis, Validation, Visualization, Writing - original draft, Writing - review & editing

Paper VI

Spectroscopy along Flerovium Decay Chains: Fine Structure in odd-A ^{289}Fl

D.M. Cox, **A. Såmark-Roth**, D. Rudolph, L.G. Sarmiento, B.G. Carlsson, J.L. Egido, P. Golubev, J. Heery, A. Yakushev, S. Åberg, H.M. Albers, M. Albertsson, M. Block, H. Brand, T. Calverley, R. Cantemir, R.M. Clark, Ch.E. Düllmann, J. Eberth, C. Fahlander, U. Forsberg, J.M. Gates, F. Giacoppo, M. Götz, S. Götz, R.-D. Herzberg, Y. Hrabar, E. Jäger, D. Judson, J. Khuyagbaatar, B. Kindler, I. Kojouharov, J.V. Kratz, J. Krier, N. Kurz, L. Lens, J. Ljungberg, B. Lommel, J. Louko, C.-C. Meyer, A. Mistry, C. Mokry, P. Papadakis, E. Parr, J.L. Pore, I. Ragnarsson, J. Runke, M. Schädel, H. Schaffner, B. Schausten, D.A. Shaughnessy, P. Thörle-Pospiech, N. Trautmann, and J. Uusitalo

Manuscript to be submitted to Phys. Rev. Lett. It has not yet been subject to internal revision of the co-authors. Once published accessible via hyperlink Paper VI in pdf version.

A. Såmark-Roth: Project administration, Software, Investigation, Formal analysis, Validation, Writing - review & editing

Paper VII

Kärnfysikalisk seglats mot mytomspunnen ö

Johan Joelsson, Daniel Cox, Claes Fahlander, Dirk Rudolph, and
Anton Såmark-Roth

Press release, published 25 Januari 2021, Lund University.

Swedish: www.lu.se/artikel/karnfysikalisk-seglats-mot-mytomspunnen-o
English: www.lunduniversity.lu.se/article/nuclear-physicists-voyage-towards-mythical-island

A. Såmark-Roth: Writing - review & editing

Publications not included in this thesis

β decay of ^{127}Cd and excited states in ^{127}In

Ch. Lorenz, L.G. Sarmiento, D. Rudolph, P. Golubev, T. Eronen, D.A. Nesterenko, A. Kankainen, L. Canete, D.M. Cox, A. Fernandez, U. Forsberg, A. Jungclaus, I. Kojouharov, N. Kurz, N. Lalović, J. Partanen, M. Reponen, S. Rinta-Antila, A. de Roubin, **A. Såmark-Roth**, V. Vaquero, and M. Vilén

Phys. Rev. C **99**, 044310 (2019).
DOI: 10.1103/PhysRevC.99.044310

A. Såmark-Roth: Investigation (supporting), Writing - review & editing (supporting)

α decay of high-spin isomers in $N = 84$ isotones

R.M. Clark, H.L. Crawford, A.O. Macchiavelli, D. Rudolph, **A. Såmark-Roth**, C.M. Campbell, M. Cromaz, P. Fallon, C. Morse, and C. Santamaria

Phys. Rev. C **99**, 024325 (2019).
DOI: 10.1103/PhysRevC.99.024325

A. Såmark-Roth: Validation (equal), Writing - review & editing (supporting)

Enhancement of α-particle formation near ^{100}Sn

R.M. Clark, A.O. Macchiavelli, H.L. Crawford, P. Fallon, D. Rudolph, **A. Såmark-Roth**, C.M. Campbell, M. Cromaz, C. Morse, and C. Santamaria

Phys. Rev. C **101**, 034313 (2020).
DOI: 10.1103/PhysRevC.101.034313

A. Såmark-Roth: Validation (equal), Writing - review & editing (supporting)

Identification of the New Isotope ^{244}Md

J.L. Pore, J.M. Gates, R. Orford, C.M. Campbell, R.M. Clark, H.L. Crawford, N.E. Esker, P. Fallon, J.A. Gooding, J.T. Kwarsick, A.O. Macchiavelli, C. Morse, D. Rudolph, **A. Såmark-Roth**, C. Santamaria, R.S. Shah, and M.A. Stoyer

Phys. Rev. Lett. **124**, 252502 (2020).
DOI: 10.1103/PhysRevLett.124.252502

A. Såmark-Roth: Investigation (supporting), Writing - review & editing (supporting)

Conference contributions

Associated paper is indicated.

9th Workshop on the Chemistry of the Heaviest Elements
2017-10-10, Ascona, Switzerland
Talk: *Sub-microsecond α-particle emitters* (Paper I)

Workshop on decay spectroscopy of the heaviest elements and related topics
2018-05-09, Stralsund, Germany
Talk: *Low-lying states in ^{219}Ra and ^{215}Rn: sampling microsecond α-decaying nuclei* (Paper I)

TASCA Workshop 2018
2018-09-25, Darmstadt, Germany
Talk: *Low-lying states in ^{219}Ra and ^{215}Rn: sampling microsecond α-decaying nuclei* (Paper I)

Swedish Nuclear Physics Meeting 2018
2018-10-17, Uppsala, Sweden
Talk: *Toward Flerovium Spectroscopy and Lundium* (Paper II)

NUSPRASEN Workshop 2019
2019-02-25, Darmstadt, Germany
Invited talk: *Toward Flerovium Spectroscopy and Lundium* (Paper II)

International Conference on the Chemistry and Physics of the Transactinide Elements (TAN19)
2019-08-30, Wilhelmshaven, Germany
Talk: *Nuclear spectroscopy along ^{287,289}Fl decay chains* (Paper III)

Swedish Nuclear Physics Meeting 2019
2019-10-24, Lund, Sweden
Talk: *Nuclear spectroscopy along flerovium decay chains* (Paper III)

NUSTAR Annual Meeting 2021
2021-02-25, Video conference
Invited talk: *Spectroscopy along Flerovium Decay Chains* (Paper IV)

Popular science contributions

Kulturnatten - Open house
2019-09-21, Lund, Sweden
Responsible for the activity: *Strålande natur* ("Radiating nature")
Sources of terrestrial radiation were discussed with the general public.

Stämde allting i serien Chernobyl?
2019-07-31, Morgonpasset i P3, Sveriges Radio
Radio interview (in Swedish): https://sverigesradio.se/sida/avsnitt/1350248?programid=4765

Periodiska systemet - Grundämnena som nyckel till makt
2019-02-28, Vetandets Värld, Sveriges Radio
Radio interview (in Swedish): https://sverigesradio.se/avsnitt/1242855

Acknowledgements

Home office, Lomma, Sweden *2021-05-08*

It is with mixed feelings that the PhD thesis now is coming to an end. As I soon embark on a new journey, I look back on the last four and a half years with a smile on my face.

First of all, it has been a true privilege to be part of the Lund nuclear structure group in the experimental investigations on superheavy nuclei.

Dirk, to me you exemplify the ideal supervisor. Your dedication to nuclear structure and to the well-being of the entire team creates an environment that any PhD student can flourish in. I can rely on you, and if all goes well it will be an honor to be able to refer to you as my “Doktorvater”.

Pico, without your computer and DAQ expertise, my PhD time would have been a lot more difficult. Thanks for the important support when I thought I had “deleted” flerovium chains, the music influences (“Quimbara”) and that you so thoughtfully checked in with friendly chats now and then.

Danny, you have been the perfect “rubber duck”. I am so grateful for all the proofreading you have done, the English you have taught me (including “rubber duck”) and the knowledge on various aspects of spectroscopy experiments you shared with me. I will also remember the wonderful road trips we did together, transporting our Compex babies around.

Pavel, thanks for your detector magic and for being a repeated source of laughter.

Yuliia, between subjects of nuclear energy and exercising, talking to you, my day became brighter. I wish you the best of luck with your thesis.

Claes, thanks for your wise questions, feedback on Expedition Flerovium and positive aura spreading to all of us in the group.

To previous PhD students of the group, but especially Ulrika, your work has been a great inspiration and I am grateful for having been able to pick your brain when I had the opportunity.

I want to direct a big thanks to the people at GSI and the TASCA group. The experiment’s success is much owed to the steady operation of the separator you have built and maintained. Among the experiment collaborators across the world, I would like to give a special thanks to you, Jacob, and your dedicated work setting up TASISpec, but also to Rod and the others who stayed at the

GSI guest house. Throughout, the sometimes hectic periods of the experiment, you made breakfasts and dinners something I looked forward to.

Thanks, Gillis, Martin, Jimmy, Ingemar and Sven, theorists from upstairs, for the fun and fruitful discussions at the “nuclear physics coffee”.

Nathaly, Oscar, Nicholai and Yuliia, my office mates. Thanks for making the B213 office a safe place to return to, as well as easy and pleasant to work from. And thanks for putting up with my occasional singing and dancing.

Throughout the regular working days, the highlight of the day was often lunch. Markus, thanks for your positive spirit always taking everyone out to eat. With Alex, Rob and Jason as part of the regular company, we have spent many hours lively discussing all kinds of perspectives on life. It has been great to get to know you.

Thanks Emil for our delightful Helsingborg train rides.

Finally, it has been a pleasure to get to know the people working at the division and in the B200 corridor throughout my PhD studies: Guillaume, Moa, Johan, Stina, Linus, Christian, Nataša, Vytenis, Johan, Pontus, Julius, Charlotta, Joakim, Kristina, Hanno, Francesco, Mikael, Per, Jan, Göran, Kevin, Yulia and Jane.

Christian och Jesper, tack för er trogna vänskap.

Catharina, Liselott och Per, er omtänksamhet och tro på mig ger mig energi och jag ska se till att ni får de allra bästa platserna på nobelmiddagen.

Adrian, det är en trygghet att vända sig till dig. Tack för din och Saras fina återkoppling på Expedition Flerovium.

Mina kollegor på hemmakontoret, Ulrica, Lovisa och snart lillebror, ni ger mig mening, glädje och motivation. Utan er hade det inte blivit något. Älskar er.

Mamma och Pappa, er kärlek och stöd har tagit mig så långt. Denna avhandling är till er.

Expedition Flerovium (SV)

En kort populärvetenskaplig berättelse om experimentet

Till minne av Anders

Anders hade, så länge han kunde minnas, drömt om att få utforska den kärnfysikaliska världen, det vill säga utkanterna av nuklidkartan. Han satt på färjan som just hade lämnat hamnen vid Blybergets kust. Kursen var riktad mot Aktinidön, utgångspunkt för denna världs upptäckare. Nu skulle drömmen äntligen gå i uppfyllelse.

Bakom Blyberget skymtade Anders Stabilitetsbergen och dess långa mäktiga bergskedja. Anders hade växt upp en bit sydväst längs med Stabilitetsbergen, vid breddgraderna kring Tenn. Här hade han tidigt fascinerats av den kärnfysikaliska naturen. Naturen strålade i huvudsak av tre olika partiklar. Dessa kallades för alfa-, beta-, och gammapartiklar. I vår värld kan alfapartiklarna liknas med stora delfiner, betapartiklarna med clownfiskar och gammapartiklarna med små plankton. Partiklarna trivdes bra nära havsnivån vid kusterna men som allra bäst i havets djup. På stränderna och i det grunda vattnet längs kusterna var alfa-, beta- och gammapartiklarna som långsammast och röda. Ju

Nuklidkartan

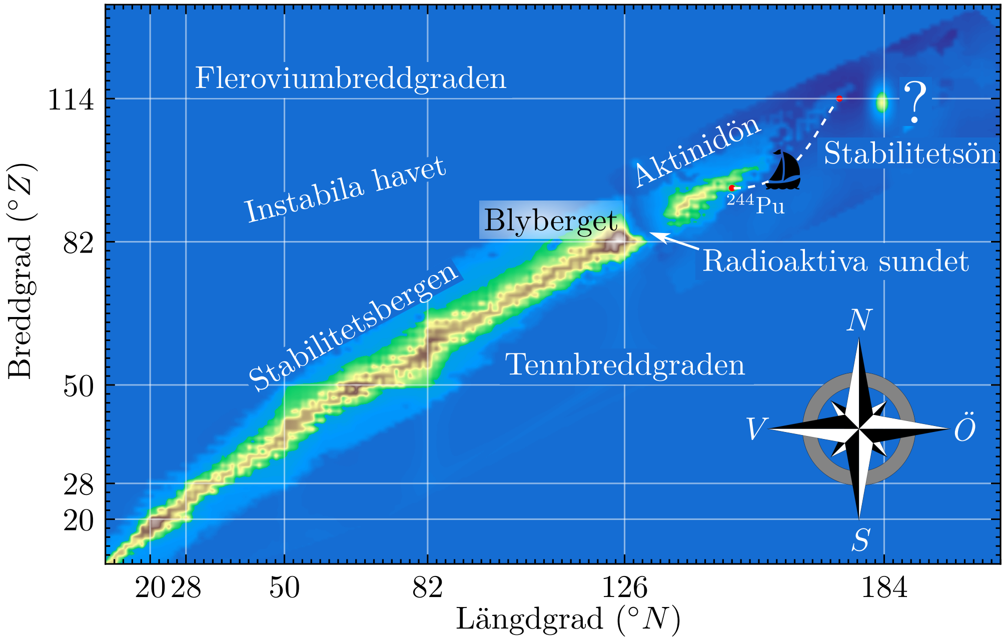

längre från kusten man tog sig och havet blev djupare, desto snabbare blev partiklarna. De blev gula, gröna, blåa och de allra snabbaste var sällsynt lila.

Det var första gången som Anders var så långt nordöst som Blyberget. Det Radioaktiva sundet som han nu färdades över hade han bara hört talas om. Naturen var mycket annorlunda här jämfört med den vid Stabilitetsbergen. Istället för mestadels beta- och gammapartiklar, strålade det här av alfapartiklar. Sundet var väldigt djupt, och det fanns gott om turkosa och till och med lila alfapartiklar. Det var ett spännande område, men redan väl utforskat.

Till skillnad från Stabilitetsbergen var Aktinidön ett instabilt lågland som sakta föll sönder. Så småningom skulle den täckas av vatten. Ibland sågs det också starkt blått ljus från marken, ett tecken på att den föll samman. Aktinidön var värd för flertalet hamnar. Det var härifrån många av denna världs upptäckare var baserade. Titt som tätt, gav sig olika besättningar ut på expeditioner i sina skepp. Det fanns de som drog nytta av sydliga fissionsvindar, med vilka man kunde nå exotiska havsdelar sydöst om Stabilitetsbergen. Andra specialiserade sig på nordliga fusionsvindar som kunde föra expeditionen mot oupptäckta områden i nordöst.

Anders hade ett särskilt intresse för dessa nordliga fusionsvindar. Det var därför han inte kunde låta bli att besöka värdshuset Supertung, som det första han gjorde när han anlänt till Aktinidön. Han sätter sig vid bardisken. Så småningom tar en äldre dam och herre platserna bredvid honom. De är pratsamma och det är Anders tacksam för. Maria och Sven, som de heter, visar sig vara erfarna utforskare. När Anders berättar om sin nyfikenhet för nordliga expeditioner, blir de exalterade och Sven säger “Äntligen! Här har vi någon som liknar oss när vi var unga. Det finns så mycket spännande att utforska. Har du hört ryktet om Stabilitetsön?”. Det hade Anders. Maria förklarar “Som du känner till så har vi framgångsrikt kunnat koppla de högsta topparna längs Stabilitetsbergen till särskilda längd- och breddgrader. För länge sedan förutsågs att det skulle finnas ytterligare en ö på nuklidkartan. Denna ö skulle ligga nordöst om Aktinidön, på längd- och breddgrader som ännu ej utforskats. Eftersom våra beräkningar visade på att denna mytomspunna ö kunde vara mer stabil än Aktinidön, fick den namnet Stabilitetsön.” Anders inflikar: “Är ni alltså två av de berömda utforskarna?” Sven och Maria nickar. Wow, tänker Anders, här får han en pratstund med två av de legendarer som det hade berättats om då han var yngre. Sven fortsätter att berätta. “Enligt våra beräkningar så borde ön ligga längs med 184:e längdgraden och 114:e breddgraden, känd som Fleroviumbreddgraden. Med utvecklingen av snabbare båtar och mer känslig mätutrustning, finns det nutida upptäckare som hävdar att de skymtat Stabilitetsön.” Anders är förbluffad, men får ändå ur sig “Jag skulle vilja vara med på en sådan expedition”. Maria och Sven ler och Maria säger “Jag misstänkte det. Med en sån framåtanda som du har, så ska vi hjälpa dig.”

Anders har lämnat värdshuset och är nu på väg till östra Plutoniumhamnen. Enligt Maria och Sven skulle kapten Didrik, som Sven kände väl, och deras båt Lundium var förtöjd där. Upptäckarna på Lundium hade tidigare utforskat havet kring breddgrad 115 och varit de första som uppmätte gammapartiklar så nära Stabilitetsön. Nu skulle de ge sig iväg på en ny expedition med ännu känsligare mätutrustning. I väntan på den kraftiga nordanvinden som krävdes för att nå den avlägsna Fleroviumbreddgraden låg Lundium förtöjd i hamnen.

I hamnen är det stor aktivitet och många människor vid en båt och därför hittar Anders enkelt Lundium. Han frågar en person med långt skägg som viker segel på fördäck om han vet var kaptenen befinner sig. Han svarar “Jo, kapten Didrik, det är han som står där borta i aktern och överser att allting lastas på ordentligt.” Anders tackar och går mot aktern. Innan han hinner presentera sig, säger kapten Didrik “Är det du som är Anders?”. Maria eller Sven hade tydligen redan hunnit prata med Didrik. Han fortsätter “Vi kan behöva förstärkning till vår besättning. Vår trogne fördäcksgast Per bröt benet och kan inte följa med. Du kommer i grevens tid. Det börjar blåsa upp och vi kastar strax loss”.

Bara inom en timme har Lundium tagit sig ut på de nordöstra delarna av det Instabila havet. “Nu är vi äntligen på väg”, säger kapten Didrik. Anders introduceras till Dan-Åke och Peter, de övriga i besättningen. “Dan-Åke är styrman. Peter är vår navigatör. Jag själv är kapten och även ansvarig för storseglet. Anders du får ta hand om förseglet”, säger Didrik. Rollerna är fördelade och med vinden i ryggen seglar de iväg. Till en början är det måttliga vindar och ganska lugnt. Anders passar på att fråga “Hur kommer det sig att det var så många involverade i lastningen?”. Peter svarar “Även om det var lite stressigt att komma iväg, så har vi planerat och förberett för denna expedition i flera år. Vi är själva duktiga seglare, det är därför vi sitter i båten. Skeppsvarvet har utfört ovärderliga uppgraderingar av båtens köl. Segelmakare har skräddarsytt de snabbaste seglen. Experter har tagit fram den känsligaste mätutrustningen. Allt detta möjliggör, tillsammans med oss här på Lundium, att vi kan segla till Fleroviumbreddgraden och göra exklusiva mätningar.” Anders säger ödmjukt, “Vilken ära att få segla med er”.

Efter några lugna dagar blåser det upp ordentligt och alla är på helspänn. Plötsligt hörs en dunk och båten stannar upp. Dan-Åke utbrister “Det är något som fastnat i rodret, jag kan inte styra”. Oro utbryter på däck men Anders agerar snabbt och tar initiativet att dyka ner för att ta en titt. En stor samling tång hade fastnat på rodret och Anders jobbar snabbt för att avlägsna den.

All tid är värdefull. Kapten Didrik berömmer “Bra jobbat Anders! Nu kan vi fortsätta utnyttja den starka vinden och ta oss så långt nordöst som möjligt.”

Efter några tuffa dagar i kulingvindar försvinner vinden helt och det blir stiltje. Lundium har anlänt till Fleroviumbreddgraden. “Alle man, till mätinstrumenten!”, ropar Kapten Didrik. “Innan vinden vänder måste vi samla in så mycket data vi kan.” Mätningarna går bra, de får se många blåa alfapartiklar som bekräftar vad tidigare expeditioner identifierat. På längdgrad 174, ser de plötsligt en ny typ av alfapartikel, med en särskild nyans av turkos. De trodde knappt att det var sant. Med ett stort leende på läpparna, säger Dan-Åke “Wow, det här var ingenting vi förväntade oss”. Kapten Didrik berättar att genom att placera ut den unikt turkosa alfapartikeln på kartan kan man se att Stabilitetsön faktiskt inte borde ligga längs med Fleroviumbreddgraden. Anders förstår och lägger till: “Den finns alltså snarare på nordligare breddgrader”. Vilken genombrytande upptäckt!

Peter tittar noggrannare på den insamlade datan och säger efter en stund “Jag har fler goda nyheter, det är ganska grunt här och det finns sten på botten”. Dan-Åke stämmer in “Underbart, våra känsliga mätinstrument kommer verkligen till god användning”. I rask takt staplar de stenar från botten på varandra och formar en grund. Med ytterligare material bygger de en fyr. När den står klar tar Didrik, Peter och Dan-Åke sig ivrigt upp i fyren. Anders är lång och stannar kvar på marken. Han tror sig kanske skymta Stabilitetsön bakom dimman i horisonten. Kapten Didrik rundar av den framgångsrika “Expedition Flerovium” och säger stolt “Nu har vi skapat ett tydligt riktmärke för alla seglare efter oss. Kanske kan fyren hjälpa framtida expeditioner att nå den mytomspunna ön.”

Nuklidkartan

Koordinaterna

En nuklid är en atomkärna uppbyggd av en unik kombination av neutroner och protoner. Varje par av heltalskoordinater på nuklidkartan representerar en atomkärna. Breddgraden representerar antal protoner i kärnan (betecknas Z), vilket även definierar grundämnet, medan längdgraden representerar antal neutroner (betecknas N). Längs med en breddgrad finns det alltså olika varianter, isotoper, av ett grundämne.

Stabilitetsbergen och Instabila havet

Höjdnivån över havet representerar de olika nuklidernas stabilitet. De flesta kärnor som är lokaliserade längs med Stabilitetsbergen är stabila, det vill säga, de sönderfaller inte. Nuklider lokaliserade nära havsnivån och på det stora Instabila havet är instabila och sönderfaller (se nästa punkt).

Alfa-, beta- och gammapartiklar samt det Radioaktiva sundet

Nukliderna som placerar sig nära samt under havsnivån är instabila. Det innebär att de är radioaktiva. När de sönderfaller sänder de ut olika typer av joniserande strålning som exempelvis alfa-, beta- och gammapartiklar. Ju lägre altitud, desto kortare livstider har kärnorna, med andra ord, desto mer instabila är de. Atomkärnor i det Radioaktiva sundet är särskilt kortlivade och kan ha livstider på endast mikrosekunder. Ofta har den utsända strålningen från mer instabila kärnor högre energi. Genom att mäta alfa-, beta- och gammapartiklarnas energi erhålls en inblick i hur atomkärnan fungerar och dess stabilitet. I berättelsen symboliserar partiklarnas färger deras energier, från regnbågens spektrum med lägst energi som röd och högst energi som lila.

Aktinidön och ^{244}Pu

Aktinidön är värd för de tyngst naturligt förekommande nukliderna, i huvudsak isotoper av grundämnena uran och torium. Eftersom de har livstider på flera miljarder år återfinns de fortfarande i relativt stor mängd på jorden. Nuklider på Aktinidön kan sönderfalla med något som kallas spontan fission. Då delar kärnan upp sig i två lättare kärnor och mycket energi frigörs. De sydliga fissionsvindarna i berättelsen symboliserar skapandet av lättare kärnor. Tvärtemot, så representerar de nordliga fusionsvindarna fusionsprocessen, det vill säga när två kärnor smälter samman och skapar en tyngre kärna. I experimentet är det fusion mellan kärnor av ^{244}Pu och ^{48}Ca som skapar det supertunga grundämnet flerovium. ^{244}Pu betecknas den isotop av grundämne 94, plutonium, med 150 neutroner.

Markerade bredd- och längdgrader

Atomkärnor med ett så kallat magiskt antal protoner och/eller neutroner uppvisar extra stabilitet, det vill säga de är mer resistenta mot att radioaktivt sönderfalla samt är i större utsträckning stabila. Det var Maria Göppert Mayer som först lyckades förklara bakgrunden till dessa magiska tal med den mycket framgångsrika skalstrukturmodellen för atomkärnan.

Tenn är ett exempel på ett grundämne som har ett magiskt antal protoner (50) i kärnan. Därför finns det ett stort antal stabila isotoper längs med Tenn-breddgraden och de gestaltas med höga bergstoppar på nuklidkartan. De största magiska talen som hittills bestämts är 82 och 126 för protoner respektive neutroner. Atomkärnor med just så många protoner och/eller neutroner finns på Blyberget, som därför är extra högt.

Nästa magiska tal har ännu inte kunnat fastställas, men det har vanligen förutspåtts att atomkärnor av grundämne flerovium (alltså längs med Flerovium-breddgraden) med 114 protoner och särskilt isotopen med 184 neutroner kan vara nästa kärna som har både magiskt antal protoner och neutroner. Just i närheten av dessa magiska tal, är det möjligt att väldigt långlivade, till och med stabila, så kallade supertunga kärnor existerar. Sökandet efter denna Stabilitetsö har fascinerat kärnfysiker ända sedan den först förutsågs av teoretiker på slutet av 1960-talet av bland andra lundafysikern Sven-Gösta Nilsson.

Visualisering

Visualiseringen av Nuklidkartan baseras på tabulerade halveringstider[1]. Finjusteringar har gjorts med överlagring av Gaussiska toppar samt skalstrukturkorrigering[2]. Inspiration har tagits från tidigare liknande verk.

Fleroviumfyren har målats av Sverker Holmberg.

---

[1] Nuclear Wallet Cards Search: `https://www.nndc.bnl.gov/nudat2/indx_sigma.jsp`

[2] P. Möller *et al.*, At. Data. Nucl. Data Tables **109-110**, 1 (2016).

Expedition Flerovium (EN)

A short popular science story about the experiment

In memory of Anders

Anders had, for as long as he could remember, dreamed of exploring the world of nuclear physics, that is, the edges of the Chart of Nuclides. He was sitting on the ferry that had just left the harbor on the shores of Lead Peak. The course was aimed for Actinide Island, the starting point for this world's discoverers. His dream was finally about to come true.

Behind Lead Peak, the Stability Mountains and its long mighty mountain range loomed. Anders had grown up a bit southwest along the Stability Mountains, at the latitudes around Tin. Here he had from early years been fascinated by nuclear physics' nature. Nature radiated mainly from three different particles. These were called alpha, beta, and gamma particles. In our world, the alpha particles can be likened to large dolphins, the beta particles to clownfish, and the gamma particles to small plankton. The particles thrived well near sea level on the coasts but at their best in the depths of the sea. On the beaches and in the shallow water along the coasts, the alpha, beta and gamma particles were

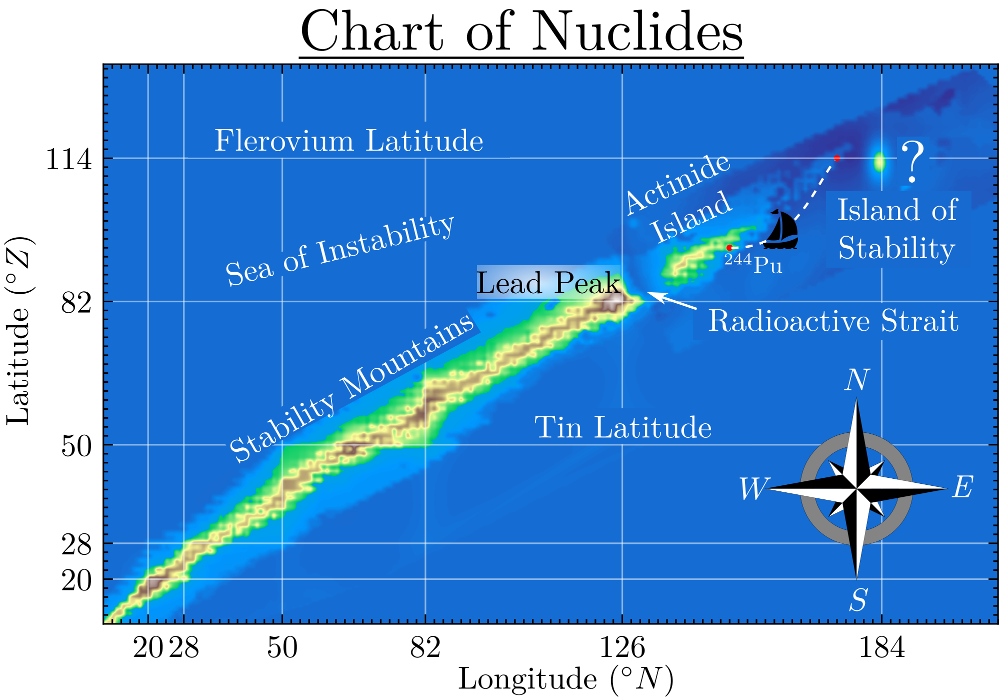

the slowest and red. The further from the coast you went and the sea became deeper, the faster the particles became. They turned yellow, green, blue and the fastest were purple.

It was the first time that Anders was as far northeast as Lead Peak. He had only heard of the Radioactive Strait over which he now traveled. Nature was very different here compared to that at the Stability Mountains. Instead of mostly beta and gamma particles, nature here radiated from alpha particles. The strait was very deep, and there was plenty of turquoise and even purple alpha particles. It was an exciting area, but already well explored.

Unlike the Stability Mountains, the Actinide Island, is an unstable lowland that is slowly falling apart. Far in the future, it would be covered by water. Sometimes strong blue light was also seen from the ground, a sign that it was collapsing. The Actinide Island was the host for many ports. It was from here that many of the discoverers of this world were based. All the time, different crews set out on expeditions in their ships. There were those who took advantage of southern fission winds, with which one could reach exotic seas southeast of the Stability Mountains. Others specialized in northern fusion winds that could lead the expedition to undiscovered areas in the northeast.

Anders had a special interest in these northern fusion winds. That was why he could not help but visit the Superheavy inn when he arrived to the Actinide Island. He takes a seat at the bar. Soon an elderly lady and gentleman take the seats next to him. They are talkative and Anders is grateful for that. Maria and Sven, as they are named, turn out to be experienced explorers. When Anders talks about his curiosity for northern expeditions, they get excited and Sven says "Finally! Here we have someone similar to us when we were young. There is so much exciting to explore. Have you heard the rumor of the Island of Stability?". Anders had and Maria explains "As you know, we have been able to successfully connect the highest peaks along the Stability Mountains to special longitudes and latitudes. It was long ago predicted that there would be another island on the Chart of Nuclides. This island would be located northeast of the Actinide Island, at longitudes and latitudes not yet explored. Because our calculations showed that this mythical island could be more stable than the Actinide Island, it was named the Island of Stability." Anders interjects: "So are you two of the famous explorers?" Sven and Maria nod. Wow, Anders thinks, here he gets a chat with two of the legends that had been told about when he was younger. Sven continues "According to our calculations, the island should lie along the 184th longitude and the 114th latitude, known as the Flerovium Latitude. With the development of faster boats and more sensitive measuring equipment, there are now discoverers who claim to have glimpsed the Island of Stability." Anders is amazed, but still manages to say ”I would like to be part of such an expedition”. Maria and Sven smile and Maria says “I suspected that. With such a forward-thinking spirit as you have, we will help you.”

Anders has left the inn and is now on his way to the eastern Plutonium harbor. According to Maria and Sven, Captain Didrik, whom Sven knew well, and their boat Lundium were moored there. The discoverers at Lundium had previously explored the sea around latitude 115 and were the first to measure gamma particles so close to the Island of Stability. Now they would set off on a new expedition with even more sensitive measuring equipment. While waiting for the strong north wind that was required to reach the distant Flerovium Latitude, Lundium was moored in the harbor.

In the harbor there is a lot of activity and many people in the vicinity of one specific boat and therefore Anders easily finds Lundium. He asks a person with a long beard who folds sails on the foredeck if he knows where the captain is. He replies “Yes, Captain Didrik, he is the one standing there in the stern and overlooking that everything is loaded properly.” Anders thanks and walks towards the stern. Before he has time to introduce himself, Captain Didrik says “Are you Anders?”. Maria or Sven had apparently already talked to Didrik. He continues “We may need reinforcements for our crew. Our faithful front deck crew member Per broke his leg and can not join. You’re in the nick of time. It is starting to blow up and we take off soon”.

In just one hour, Lundium has set out on the northeastern parts of the Sea of Instability. “Now we are finally on our way,” says Captain Didrik. Anders is introduced to Dan-Åke and Peter, the others in the crew. “Dan-Åke is the helmsman. Peter is our navigator. I myself am the captain and also responsible for the mainsail. Anders, you get to take care of things at the bow”, says Didrik. The roles are distributed and with the wind in the back they sail away. At first it is moderate winds and quite calm. Anders takes the opportunity to ask “How come there were so many involved in the loading?”. Peter answers “Although it was a bit stressful to get away, we have been planning and preparing for this expedition for several years. We are good sailors ourselves, that is why we are in the boat. The shipyard has performed invaluable upgrades to the boat’s keel. Sailmakers have tailored the fastest sails. Experts have developed the most sensitive measuring equipment. All this enables, together with us here at Lundium, that we can sail to the Flerovium Latitude and make exclusive measurements.” Anders says humbly, “What an honor to sail with you”.

After a few quiet days, it blows up properly and everyone is on full swing. Suddenly a thump is heard and the boat stops. Dan-Åke exclaims “There is something stuck in the rudder, I can not steer.” Anxiety erupts on deck but Anders acts quickly and takes the initiative to dive down to take a look. A large collection of seaweed had got stuck on the rudder and Anders is working fast to remove it. Time is of the essence. Captain Didrik praises “Good job Anders!’ Now we can continue to take advantage of the strong wind and take us as far northeast as possible.”

After a few tough days in gale force winds, the wind disappears completely and there is silence. Lundium has arrived at the Flerovium Latitude. “All men, to the measuring instruments!”, shouts Captain Didrik. “Before the wind returns, we need to collect as much data as we can.” The measurements are going well, they get to see many blue alpha particles that confirm what previous expeditions have observed. At longitude 174, they suddenly see a new type of alpha particle, with a special hue of turquoise. They could hardly believe it was true. With a big smile on his face, Dan-Åke says “Wow, this was not something we expected”. Captain Didrik says that by placing the unique turquoise alpha particle on the map, you can see that the Island of Stability should not actually be along the Flerovium Latitude. Anders understands and adds: “It is thus rather found in more northern latitudes”. What a breakthrough discovery!

Peter looks more closely at the data collected and says after a while “I have more good news, it is quite shallow here and there is rock at the bottom”. Dan-Åke joins in “Wonderful, our sensitive measuring instruments really comes to use”. At a rapid pace, they stack stones from the bottom on top of each other and form a foundation. With additional materials, they build a lighthouse. When it is complete, Didrik, Peter and Dan-Åke eagerly head up the lighthouse. Anders is tall and stays on the ground. He believes he may glimpse the Island of Stability behind the fog on the horizon. Captain Didrik rounds off the successful Expedition Flerovium and proudly says “Now we have created a clear benchmark for all sailors after us. Maybe the lighthouse can help future expeditions to reach the mythical island.”

Chart of Nuclides

Coordinates

A nuclide is an atomic nucleus made up of a unique combination of neutrons and protons. Each pair of integer coordinates on the Chart of Nuclides represents an atomic nucleus. Latitude represents the number of protons in the nucleus (denoted Z), which also defines the element, while longitude represents the number of neutrons (denoted N). Along a latitude, there are different variants, isotopes, of an element.

The Stability Mountains and the Sea of Instability

The altitude above sea level represents the stability of the various nuclides. Most nuclides located along the the Stability Mountains are stable. This means that these nuclides do not decay. Nuclides located near sea level and on the Sea of Instability are unstable and decay (see next point).

Alpha, beta and gamma particles and the Radioactive Strait

The nuclides that are located close to and below sea level are unstable. This means that they are radioactive. When they decay, they emit different types of ionizing radiation such as alpha, beta and gamma particles. The lower the altitude, the shorter the lifetimes of the nuclei, in other words, the more unstable they are. Atomic nuclei in the Radioactive Strait are particularly short-lived and can have lifetimes of only microseconds. Often the radiation emitted from more unstable nuclei has higher energy. By measuring the energy of the alpha, beta and gamma particles, an insight is gained into how the atomic nucleus works and its stability. In the story, the colors of the particles symbolize their energies, from the spectrum of the rainbow with the lowest energy as red and the highest energy as purple.

Actinide Island and ^{244}Pu

The Actinide Island hosts the heaviest naturally occurring nuclides, mainly isotopes of the elements uranium and thorium. Because they have lifetimes of billions of years, they are still found in relatively large amounts on Earth. Nuclides on the Actinide Island can decay with something called spontaneous fission. Then the nucleus splits into two lighter nuclei and a lot of energy is released. The southern fission winds in the story symbolize this creation of lighter nuclei. On the contrary, the northern fusion winds represent the fusion process, that is, when two nuclei fuse together and create a heavier nucleus. In the experiment, it is the fusion between nuclei of ^{244}Pu and ^{48}Ca that creates the superheavy element flerovium. ^{244}Pu is the isotope of element 94, plutonium, with 150 neutrons.

Marked latitudes and longitudes

Atomic nuclei with a so-called magic number of protons and/or neutrons show extra stability, i.e., they are more resistant to radioactive decay and are more stable. It was Maria Göppert Mayer who first managed to explain the background to these magic numbers with the very successful shell structure model for the atomic nucleus.

Tin is an example of an element that has a magic number of protons (50) in the nucleus. Therefore, there are a large number of stable isotopes along the Tin Latitude and they are represented with high mountain peaks on the Chart of Nuclides. The largest magic numbers determined so far are 82 and 126 for protons and neutrons respectively. Atomic nuclei with this many protons and/or neutrons are found on Lead Peak, which is therefore extra high.

The next magic numbers have not yet been determined, but it has generally been predicted that atomic nuclei of the element flerovium (i.e., along the Flerovium Latitude) with 114 protons and especially the isotope with 184 neutrons may be the next nucleus with both magic numbers of protons and neutrons. Just near these magic numbers, it is possible that very long-lived, even stable, so-called superheavy nuclei exist. The search for this Island of Stability has fascinated nuclear physicists ever since it was first predicted by theorists in the late 1960s by, among others, the Lund physicist Sven-Gösta Nilsson.

Visualization

The visualization of the Chart of Nuclides is based on tabulated half-lives[3]. Fine adjustments have been made with an overlay of Gaussian peaks and shell structure correction[4]. Inspiration has been taken from previous similar illustrations.

The Flerovium lighthouse has been painted by Sverker Holmberg.

---

[3] Nuclear Wallet Cards Search: `https://www.nndc.bnl.gov/nudat2/indx_sigma.jsp`

[4] P. Möller *et al.*, At. Data. Nucl. Data Tables **109-110**, 1 (2016).

Chapter 1

Introduction

Since the dawn of the field of nuclear physics in the 1930s, the understanding of the atomic nucleus has grown fast. Today, the primary focus of both experimentalists and theorists is nuclear matter at its extreme. At the heaviest outskirts of the nuclear chart, two exciting research questions drive the research on superheavy nuclei:

- Does a region of long-lived superheavy nuclei exist and if so, where is this *Island of Stability* located?
- What is the heaviest element that can exist in nature?

The focus of the present work lies on increasing our understanding of the structure of superheavy nuclei and contribute to finding answers to the first question. The current status of the research field of superheavy nuclei is outlined in Chapter 2.

The prestiguous quest for new elements has captivated scientists for a long time [1]. As recent as in 2016, the latest line of new superheavy elements with atomic numbers $Z = 113, 115, 117$ & 118 received the names nihonium (Nh), moscovium (Mc), tennessine (Ts) and oganesson (Og), respectively. The nuclear structure group at Lund University was leading a confirmation experiment on element 115, moscovium, back in 2012. The experiment was conducted at the GSI Helmholtzzentrum für Schwerionenforschung, Darmstadt, Germany. Using a highly-efficient α-photon coincidence decay spectroscopy set-up named TASISpec, γ and X rays, stemming from the radioactive decay of nuclei of these superheavy elements, were measured for the first time. The measured X rays comprised first candidates for direct determination of the superheavy atomic numbers while the γ rays provided first glimpses of the intrinsic structure of the rare nuclear species.

In 2016, I had the privelege to join the Lund nuclear structure group as a PhD student and carry on the exciting work of my predecessor, Ulrika Forsberg [2]. The use of modern digitising electronics in the 2012 experiments opened up access to decay characteristics of α-decaying nuclei with half-lives on the order of microseconds. These nuclei were produced as background reaction products in the experiment. I had the opportunity to dive deep into this novel data set and develop algorithms to explore the nuclear structure of some of these short-lived nuclei located North-East of Pb on the nuclear chart. With this work, I was brought up to speed, got acquainted with the research field and my first peer-reviewed article, Paper I, was published.

Following the very successful element-115 experiment, the Lund research group was able to secure a grant from *Knut & Alice Wallenbergs Stiftelse* (KAW) in 2015[1]. The grant provided money for a substantial detector upgrade as well as possibilities for further superheavy-experiment explorations. It also laid the foundation for my PhD position and thesis.

The successor to the TASISpec experimental setup, *Lundium*, is in development at the time of writing. A main ingredient in the Lundium upgrade is the new *Compex* germanium detectors. In the present work, the properties of the Compex detector were scrutinised in measurements which formed Paper II. With the Compex detector, a significant step has been taken towards Lundium and these detector developments are covered in Chapter 3.

The main focus of the PhD thesis revolved around conducting new experiments on superheavy nuclei and moving the research field closer to the coveted Island of Stability. In 2017, we submitted an experiment proposal to perform α-photon coincidence spectroscopy along decay chains of element 114, flerovium, to the GSI Physics Advisory Committee. We were granted 25 days of beam time and the first twelve days were scheduled for late summer of 2018. However, due to a fire incident at GSI, it was not until March 2019 the first experimental run was initiated.

Using four new Compex detectors, an updated TASISpec decay spectroscopy setup was installed at the focal plane of the TASCA gas-filled recoil separator. During four days of so-called parasitic beam time, tools were tested and settings

---

[1] `http://kaw.wallenberg.org/forskning/de-utforskar-de-tyngsta-amnena-i-varlden`

were tuned such that the best possible data would be produced for the main "flerovium run". These measurements formed Paper III which along with the tools and settings of the experimental setup are described in Chapter 4. We continued into the main part of the experiment, and everything worked smoothly from our end. However, due to a low beam intensity, we had to quit early with nine flerovium decay chains measured.

In February of 2020, we returned to GSI for the remaining thirteen days of beam time. Now the accelerator delivered a superb beam intensity, and another twenty decay chains were measured. The experiment was followed by a comprehensive data analysis. This involved, for instance, efforts to enhance and extract the data on the flerovium-decay chains as well as a close inspection of the twenty-nine flerovium decay chains. Finally, statistical assessments accompanied with simulations were performed to facilitate interpretations. This analysis is introduced in Chapter 5, and presented in Paper V.

The measurement of two new types of even-even flerovium decay chains, starting from ^{286}Fl and ^{288}Fl, respectively, marked the discoveries of (i) an excited state in ^{282}Cn and (ii) the isotope ^{280}Ds. These significant discoveries, presented in Paper IV and as a press release in Paper VII, received a lot of attention[2], especially since they give new insights into the location of the Island of Stability. With fifteen new decay chains starting from ^{289}Fl, the global data set had almost been doubled for this isotope. The results on these chains, which are presented in Paper VI, provide new evidence of α-decay fine structure of superheavy nuclei. Chapter 6 summarizes the results of the thesis with an emphasis on the outcome of Paper IV and Paper VI. The results overall demonstrate the richness of nuclear structure that still remains to be explored in the regime of superheavy nuclei. Such concluding remarks, as well as other outlook perspectives end the thesis in Chapter 7.

---

[2] Altmetric attention score of 183 (2021-03-04), see `https://aps.altmetric.com/details/98607563`

Chapter 2

Background

Superheavy Nuclei

At the distant shore of the nuclear landscape, the possible existence of an *Island of Stability* consisting of long-lived superheavy nuclei has been tantalizing nuclear physicists ever since the first predictions in the 1960s [3–5]. The increased stability of the island relates to shell effects based on the presence of magic numbers of protons and neutrons, which many models have commonly placed at the coordinates $Z = 114, 120$, or 126, and $N = 184$ [6]. The large quantum systems formed by the superheavy nuclei are challenging to model precisely with today's theoretical approaches. At the same time, understanding their nuclear structure is particularly rewarding since their pure existence is essentially governed by the subtleties of the nuclear force [7].

The region of the nuclear chart hosting the superheavy nuclei, frequently defined as those with $Z \geq 104$, is illustrated in Fig. 2.1. Great experimental efforts have been undertaken to reach the long-sought island and tremendous advances, also from theoretical perspectives, have been accomplished throughout the last decades. Comprehensive overviews of the field, summarizing state-of-art experimental methods and theoretical approaches, can be found in, for instance, Refs. [8, 9]. Fundamental to the experimental success has been the use of fusion-evaporation reactions. First, an era of cold-fusion reactions led to the discoveries of elements 107-112 at GSI, Germany, in the 80s and 90s [10] as well as element

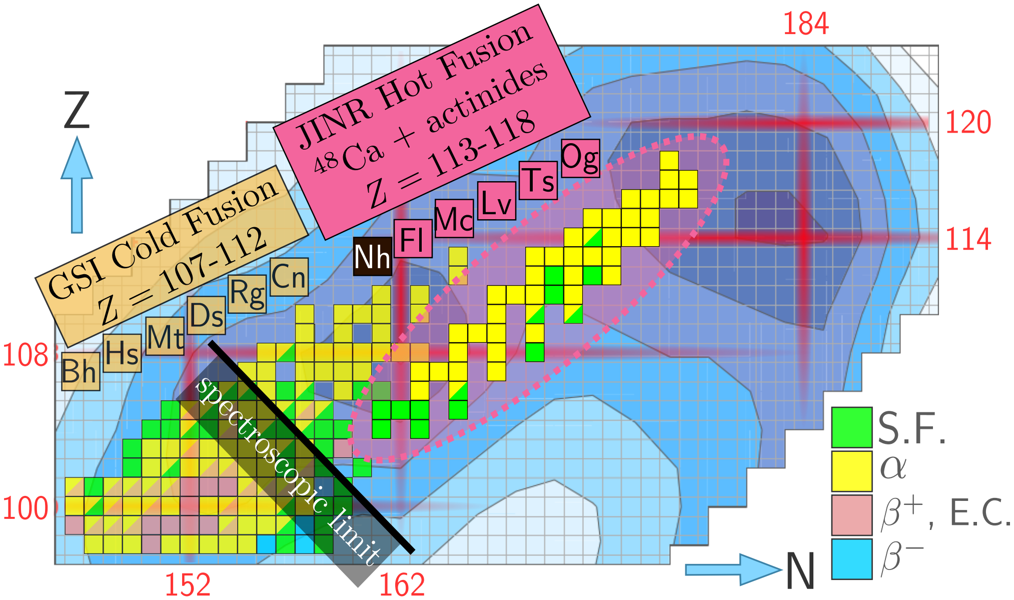

Figure 2.1: Upper end of the chart of atomic nuclei. Superheavy elements 107-112 discovered at GSI, Germany, as well as element 113, Nh, at RIKEN, Japan, and 113-118 at JINR, Russia, in cold and hot fusion-evaporation reactions, respectively, are indicated. Red background lines denote possible spherical ($Z = 114, 120$ and $N = 184$) and deformed ($Z = 100, 108$ and $N = 152, 162$) magic numbers. The combination of $Z = 114$ and $N = 184$ is one of the prominent long-standing predictions for the centre of the Island of Stability. The darker the blue background, the more stable the isotopes are predicted to be due to shell-correction effects. Nuclei produced in the fusion-evaporation reactions with ^{48}Ca form the detached encircled region, as their decay chains all end in spontaneous fission. Their low production cross sections, imply that about one nucleus per day is detected in present-day experiments. In contrast, below the "spectroscopic limit", yields of hundred nuclei per experiments have been achieved already. Figure in part courtesy of Ch.E. Düllmann.

113 at RIKEN, Japan, in the 2000s [11]. In the creation of element 110, darmstadtium, for instance, an intense beam of ^{64}Ni was accelerated and let to fuse together with a target foil made of ^{208}Pb, forming a compound nucleus at rather low excitation energies, therefore denoted *cold*. Around the turn of the millenium, experiments performed at JINR, Dubna, Russia, successfully synthesised elements 113-118 [12]. A beam of doubly-magic ^{48}Ca and actinide targets were employed. As the excitation energy of the compound nuclei produced in these reactions were considerably higher, they were denoted *hot*.

To date, the heaviest isotopes produced are $^{294}_{117}\mathrm{Ts}_{177}$ and $^{294}_{118}\mathrm{Og}_{176}$. Thus, the Island of Stability should be close, but arguably the isotopes created this far are still too neutron deficient. The nuclei produced in the hot fusion-evaporation reactions have been observed to exclusively terminate by spontaneous fission at the end of their respective decay chain. Efforts have been made to create isotopes which would establish links to lighter, known isotopes. However, they have so far been unsuccesful, therefore the observed isotopes form a part of the nuclear chart detached from the rest, as indicated in Fig. 2.1. Combined with low production cross sections on the order of picobarn, this makes for challenging experimental grounds.

Keys to the successful experiments include: (i) High intensity heavy-ion-beam accelerators, which together with the (ii) manufacturing of thick actinide targets have boosted production rates of the superheavy nuclei. With the employment of (iii) state-of-the-art separator devices, either vacuum or gas-filled types, the produced superheavy-element ions could be efficiently pre-selected, while simultaneously unwanted reaction products were strongly suppressed. Finally, by transmitting the created ions to (iv) spectroscopy setups, position sensitive silicon detectors could provide the means to identify the superheavy nuclei based on their localised characteristic α-decay chains terminating with spontaneous fission. For reviews and a thorough introduction of the experimental techniques, the reader is referred to, for instance, Refs. [2, 13, 14].

Accessible spectroscopic observables for the produced nuclei with the silicon detectors have typically been limited to decay energies and lifetimes. The energy released in the α decays, Q_α, provides one probe for the shell stability of the nuclei involved in the decay. This may be seen in Fig. 2.2(a) where Q_α values are plotted as a function of neutron number for nuclei around the magic number $N = 126$. Characteristic for the increased shell stability is a steady decrease followed by a sharp increase in Q_α as the magic number $N = 126$ is crossed. Figure 2.2(b) presents experimental values of Q_α for even-Z superheavy nuclei. With increasing neutron number, Q_α is seen to gradually decrease. This is a strong hint of the anticipated shell closure at $N = 184$, while the less pronounced "kink" at $N = 162$ indicate the existence of a deformed magic subshell [6]. The possible proton magic number $Z = 114$ has already been reached experimentally. Measured Q_α values indicate it is a rather weak shell gap, but more precise data points are desired [16, 17].

Below the "spectroscopic limit", indicated in Fig. 2.1, relatively high production cross sections open up for detailed experimental investigations. Only in the last few years, precise mass measurements with penning traps were performed of $^{256}\mathrm{Lr}$ [18] as well as of neighbouring nuclei utilising a Multireflection

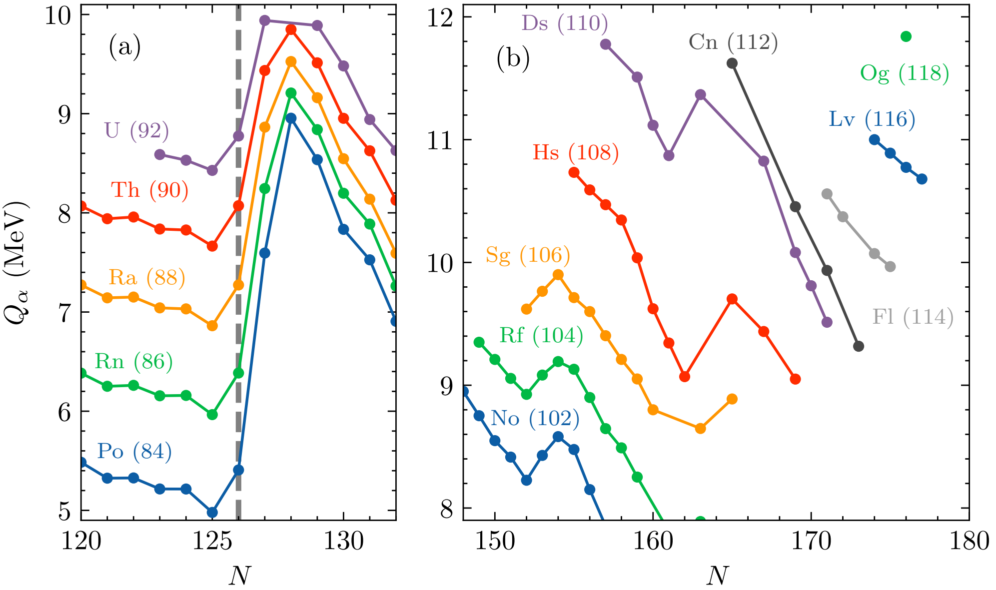

Figure 2.2: Experimental Q_α values [15] around the $N = 126$, indicated with the dashed vertical line, neutron magic number (a) and for the heaviest nuclei in (b). Only even-Z nuclei, as indicated with the element (Z), have been included. For the heaviest elements, many points are subject to tentative assignments or associated with uncertainties which have not been included here. See also Fig. 2.3 and text below.

Time-of-Flight Mass Spectrograph [19]. In-beam spectroscopy experiments have elucidated single-particle shell structure and rotational properties of the superheavy nucleus ^{256}Rf [20] as well as, for instance, configuration assignments to isomeric states [21]. Isotopes up to and around ^{261}Sg may be produced at such large rates that yields of about hundreds of nuclei per experiment can with ease be investigated in detail with decay spectroscopy setups [22].

The region below the “spectroscopic limit”, frequently referred to as the *nobelium region* due to the large microbarn cross section to synthesise ^{254}No, plays a special role in the study of the superheavy nuclei. The rich amount of nuclear structure information here provides an excellent basis for theoretical models. Nevertheless, all models still need to extrapolate towards the next spherical magic numbers. Furthermore, the present models are not sufficiently accurate to pin down the position of the energy gaps and provide reliable predictions of the Island of Stability. Thus, experimental anchor points of the superheavy nuclei produced in the hot fusion-evaporation reactions, are of special value for nuclear theory.

The production cross sections in the ^{48}Ca hot-fusion reactions are the highest for isotopes of elements 114, flerovium, and 115, moscovium, ranging from 5-10 pb [23–25] (see also Fig. 2.4 in Ref. [2]). Recent α-photon coincidence spectroscopy experiments have been able to, for the first time, shed light on the internal structure of nuclei along ^{288}Mc-decay chains [26, 27]. The observation of K X-ray candidates following internal conversion in ^{272}Bh ($Z = 107$) demonstrated the potential for direct determination of the atomic number of these superheavy nuclei. Furthermore, a subsequent experiment provided the first direct measurement of mass numbers along ^{288}Mc-decay chains, thereby confirming previously assigned mass numbers in this region [28].

Perhaps most intriguing for nuclear structure theory, the cutting-edge spectroscopy experiments allowed for the derivation of level schemes and first insights into the low-lying structure of the nuclei in this detached part of the nuclear landscape [26]. The highlight was the identification of an $E1$ transition in ^{276}Mt ($Z = 109$). The observation provided a stringent constraint on nuclear structure theory [29] and consequently prospects for more refined theoretical models. Furthermore, emphasis on high-resolution spectroscopic performance combined with GEANT4 simulations [30], enabled the precise derivation of Q_α values along the ^{288}Mc-decay chain [17].

For even-even nuclei, i.e. those with even numbers of both protons and neutrons, α decays most often proceed from ground state to ground state. In contrast, for odd-A and odd-odd nuclei, the α decays most likely enter excited states in the daughter nuclei instead, as unpaired nucleons typically remain in the same orbital as in the parent nuclei [13, 14]. This is a process usually referred to as the *fine structure* of the α decay [31]. By measuring the intensity of different α decay branches, hints on structural changes between the parent and daughter states can be deduced by calculating hindrance factors [14]. The detection of electromagnetic transitions following the decay of excited states, i.e. γ rays or electrons and X rays following decay by internal conversion, provides not just excitation energies, but also information on their multipole character which in turn gives clues on spins and parities of the involved nuclear states. Being sensitive to the electromagnetic decays also means that the total energy released in the decay, Q_α, may be determined more precisely. This underlines the experimental reach of α-photon(electron) coincidence spectroscopy and provides the main motivation behind the previously successfully conducted experiments.

The present work aims to build upon the successful spectroscopic studies along Mc-decay chains. Using the nuclear reactions ^{48}Ca + ^{242,244}Pu, high-resolution α-photon coincidence spectroscopy is performed along decay chains of flerovium. A special emphasis lies on the structure of the odd-A ^{287,289}Fl-decay chains.

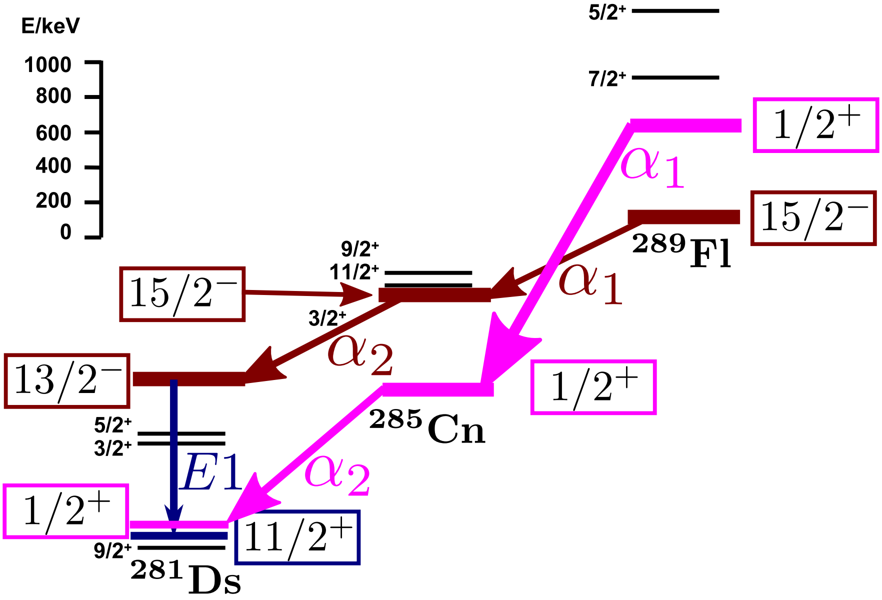

Figure 2.3: Theoretically calculated single-particle energy spectra [32] for the decay chain starting at ^{289}Fl. α-decay sequences of least hindrance and possibly coincident γ-ray emission along with involved states are marked. Figure adapted from Ref. [16].

Furthermore, the hitherto unknown isotope ^{290}Fl is in experimental reach, and measuring its decay characteristics is another objective of the experiment. Its discovery will probe shell-stabilising effects as $N = 184$ is approached.

Figure 2.3 shows theoretically calculated single-particle energy spectra for the decay chain starting at ^{289}Fl [16]. Following the electromagnetic decay of excited states in ^{289}Fl, as populated in the fusion-evaporation reaction, either the $1/2^+$ (marked pink) or the $15/2^-$ (marked brown) single-particle state would be reached. Due to the large spin difference, it is likely that the $1/2^+$ is isomeric and both states predominately α decay. Let us follow the decay sequence of the high-spin state: The first α_1 decay would proceed unhindered into an excited state in the ^{285}Cn daughter, which cannot proceed to lower lying states by electromagnetic decay modes, as the spin differences are way too large. In turn, the excited $15/2^-$ state in ^{285}Cn is likely to proceed via α_2 decay into an excited $13/2^-$ level in the granddaughter ^{281}Ds - which can readily decay by an allowed strong $E1$ γ-ray decay into the $11/2^+$ state, followed by a (converted) $E2/M1$ decay into the predicted $9/2^+$ ground state of ^{281}Ds. By the same arguments, the low-spin state ($1/2^+$) would take on a distinctively different, independent decay path.

This is one set of theoretical predictions and it gives only one example of what can be expected experimentally. However, most contemporary models predict a competition between high-spin and low-spin states for all odd-A decay chains with Z = 114-117 [25]. Thus, experimental data should reveal at least two independent decay paths for many, if not all, of the decay chains of these odd-A superheavy nuclei. This far, decays from isomeric states have merely been hypothesized, see for instance Ref. [16, 25]. The experiment aims to discriminate electromagnetic transitions as well as providing precise Q_α values along the Fl-decay chains. Ultimately, further insights into the above-mentioned matters will be gained, and the work will provide anchor points for nuclear structure theory of the heaviest elements created on Earth.

Chapter 3

Detector Development

Towards Lundium with Compex

The ideal experimental physicist in fundamental nuclear structure passionately wants to acquire data from which it is possible to best aid our theoretical understanding of the atomic nucleus. Central for the experimental physicist is *sensitivity*: With the minimal amount of experimental observations, the physicist seeks to confidently probe phenomena linked to the structural properties of the nucleus. Sensitivity, in the frame of detector development, involves mainly three properties: detection efficiency, detector energy resolution, and background suppression.

Experiments on the structure of superheavy nuclei typically revolve around decay spectroscopy. Here properties of the superheavy nuclei, pre-selected by a separator by means of electromagnetic deflection of ions, are investigated by measuring energy spectra as a result of their radioactive decays. This is best achieved in setups where emitted charged particles are detected in an array of silicon detectors and photons in surrounding germanium detectors. In the current chapter, the background to the upgrade from the *TASISpec* setup to the *Lundium* decay station is described. This upgrade initiates the chapter, and will enable a boost in sensitivity for decay spectroscopy experiments of superheavy nuclei.

A main ingredient in the upgrade to Lundium are the new *Compex* germanium detectors of which development have been a focus of the current thesis. By employing these detectors, improvements on photon detection efficiency as well as energy resolution are foreseen. In order to confidently claim new structural properties of superheavy nuclei, it is of utmost importance to characterise the engaged detectors in detail – in particular since the Compex modules form a new type of detector. For an introduction and description of the Compex detector, the reader is referred to Paper II. This publication covers a characterisation of the Compex detector with source measurements probing detection efficiency and energy resolution. Further measurements were performed with the *Lund scanning system*, wherein pulse shape response of the detector as function of interaction position were investigated.

In the current chapter, background information on the design and construction of the Lund scanning system is given. A summary of the results from the energy resolution and efficiency measurements of the Compex detectors follows. The chapter is concluded with prospects to further improve sensitivity in decay spectroscopy with Lundium through various efforts on background suppression.

3.1 Lundium decay station

The decay spectroscopy setup TASISpec [33] is rendered in Fig. 3.1(a). Here charged particles are measured in a compact box of five double-sided silicon strip detectors placed inside a vacuum chamber with thin (0.5-1.0 mm) aluminium housing. Photons are measured in EUROGAM-type Clover [34, 35] and EUROBALL Cluster [36] composite germanium detectors, accessible through European collaborations. The detectors are positioned as close as possible outside the vacuum chamber.

The foundation of TASISpec is built upon the proficiency to detect low-energy photons. This is mainly because electromagnetic transitions in the region of superheavy nuclei often undergo internal conversion due to their high proton numbers and anticipated small transition energies $< 500\,\text{keV}$. Internal conversion is a process where the deexcitation of the nucleus results in the ejection of electrons orbiting the nucleus. Following the atomic deexcitation, X-ray photons are emitted. For superheavy elements the X rays also assume low energies. For instance, K and L X rays have energies of $\sim 170\,\text{keV}$ and $\sim 30\,\text{keV}$ for flerovium, $Z = 114$, respectively [37]. Just as with γ rays, the X rays provide information on the properties of the electromagnetic transition, which in turn gives important clues on the underlying nuclear structure. Furthermore, they provide the attractive possibility to fingerprint the proton number, Z, of the

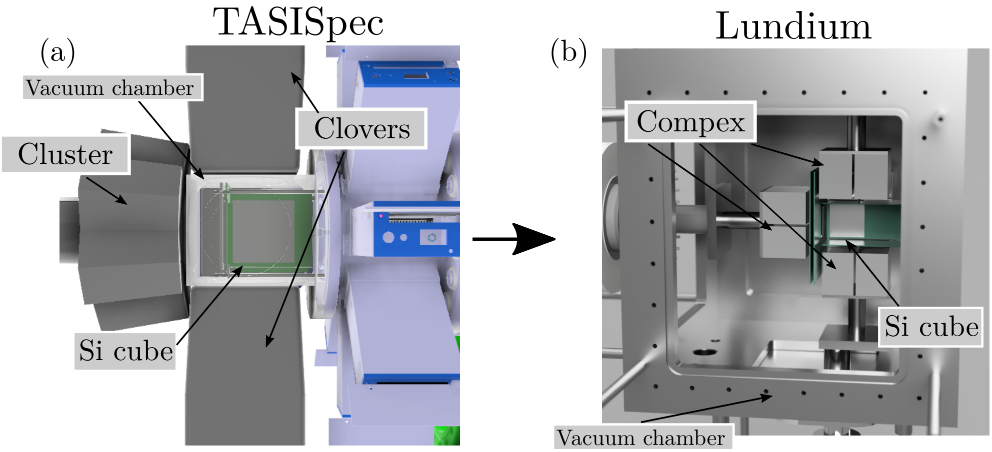

Figure 3.1: Side view of the TASISpec (a) and the Lundium (b) decay stations. The germanium detectors and the side plate of the Lundium chamber, closest to the screen, have been removed. The TASISpec vacuum chamber has been made transparent such that the silicon detectors mounted on green boards are visible. The Compex detectors are without end-caps. Relevant components are indicated. Lundium render with courtesy of D.M. Cox.

decaying nucleus [26, 38].

With an efficiency for detecting charged particles in the silicon detectors at $\sim 80\%$ [33], and coincident photons in the germanium detectors of $\sim 40\%$ at 150 keV [30], TASISpec is one of the most efficient multicoincidence decay spectroscopy setups. However, despite the close proximity of the germanium detectors to TASISpec's compact silicon box (illustrated in Fig. 3.1(a)), there are still a few centimetres between silicon detectors and germanium crystals. For some Clover type detectors, the end-cap to germanium crystal distances are also significant at $>$ 10 mm. In addition, since the Clover and Cluster detectors were initially designed for use at in-beam γ-ray spectroscopy experiments, which employ spherical vacuum chambers, their crystals therefore have coaxial cylindrical or hexagonal-tapered shapes. Combined, these aspects result in an impaired solid angle coverage in the box-shaped geometry, imposed by the optimal particle detection in the silicon detector cube. Furthermore, sources of unwanted material, from e.g. the vacuum chamber, cause significant losses of photon detection efficiency, in particular at low energies, which is crucial for the detection superheavy-element L X rays (see also Fig. 3.2).

TASISpec's succcessor Lundium confronts the above-mentioned possibilities for improvement. Fundamental to the transformation, which is animated in Ref. [39], is the use of new Compex germanium detectors sitting in direct proximity to

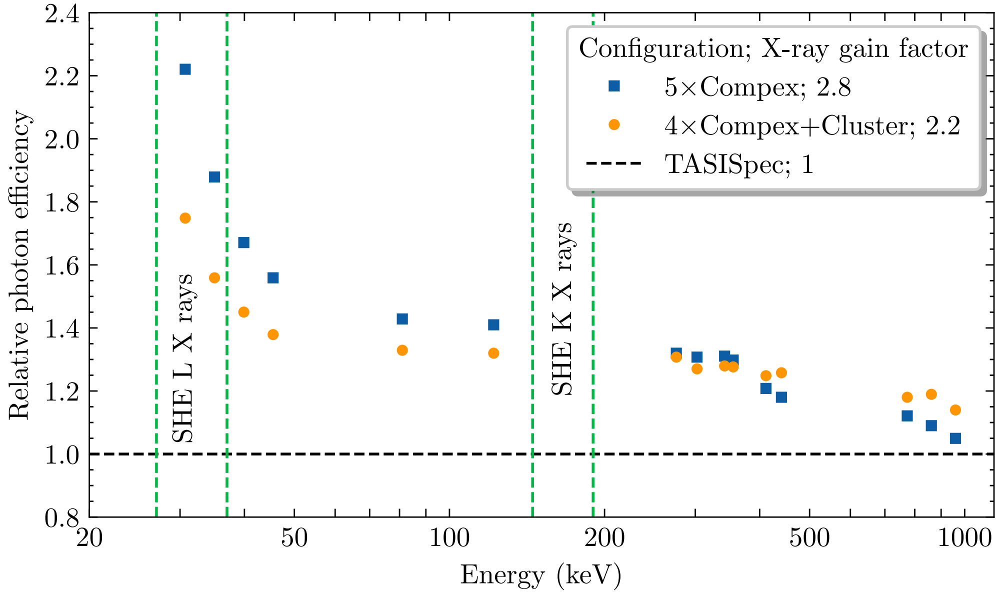

Figure 3.2: Geant4 simulation of the photon detection efficiency of two candidate germanium detector configurations for Lundium relative to TASISpec. Regions of superheavy-element L and K X rays are indicated with the vertical dashed lines (upper and lower limits deduced from $Z = 108$-118 [37, 40]). Based on these regions, X-ray gain factors, defined as the product of the gain in detection efficiency for a coincidence between K and L X-rays, which would provide the decisive measure for Z-fingerprinting of superheavy elements, was calculated. These values are provided to the right of the different configurations in the legend. Data with courtesy of L.G. Sarmiento.

an evolved silicon-detector box *inside* the Lundium chamber. This chamber is depicted in Fig. 3.1(b). Compex, being a portmanteau of compact and exotic, is the first γ-ray detector tailored for use with the box-shaped silicon detector configuration in decay spectroscopy setups. With its coaxial, cubic-shaped, germanium crystals in compact capsules, solid-angle coverage of the germanium detectors in Lundium is significantly improved [Paper II]. Furthermore, since the four germanium crystals of the composite Compex detector are single-encapsulated, they may be operated without their end-caps in vacuum, which combined with the fact that they sit in the same chamber as the silicon box, further optimises the Lundium photon detection efficiency, especially at low energies.

Geant4 simulations, building from Ref. [30], of different germanium detector configurations laid the foundation for the Lundium design. Figure 3.2 shows the gain in photon detection efficiency of two candidate Lundium configurations relative to TASISpec from these simulations. The first configuration comprises only Compex detectors, while in the second a Cluster detector sits slightly closer behind the implantation silicon detector compared to the original TASISpec setup. It is clear that both configurations present significant improvements of the detection efficiency of low-energy photons. As a mean to quantify the improvement and choose a final configuration for Lundium, the X-ray gain factor was introduced, see caption and Fig. 3.2. Persuaded by the best X-ray gain, the 5×Compex configuration was finally chosen for Lundium. Apparent from the simulations is that decay spectroscopy with Lundium paves the way for increased charged particle-photon coincidence detection efficiency.

3.2 Scanning a Compex germanium detector

The new Compex detectors and the unique geometry of their germanium crystals motivate a characterisation of their pulse-shape response. A distorted and weak electric field near the front corners of the cubic crystals could imply long charge collection times which could make them prone to trapping and lead to peak-height deficiency (for more background, see Refs. [41, 42]). In turn, this could have the implication of an unsatisfactory spectroscopic performance.

The identification of any regions with incomplete charge collection was the main motivation for the construction of the Lund scanning system. However, other motivations included the exploration and the possibility to perform correction procedures to optimise a potentially mediocre energy resolution. The scanning system is introduced in Paper II. Here, some additional background information is given while component and operation details of the scanning system are provided for interested readers in Appendix A.

Triggered by the building of the γ-ray tracking spectrometer AGATA [43], scanning systems, being able to characterise the response of its electrically segmented germanium crystals in detail, emerged around Europe. The principle of the standard scanning system investigates the detector response as a function of interaction position (x, y, z) through coincidence techniques, such as that presented in Ref. [44]. Albeit the great spatial resolution possible in these coincidence scans, other methods were explored much due to the very long time it takes to perform a scan. Consecutive scannning systems utilise pulse shape comparison techniques for faster characterisations [45, 46].

Due to absence of time constraints and its simplicity, the coincidence scan technique was selected for the Lund scanning system. Its working principle is illus-

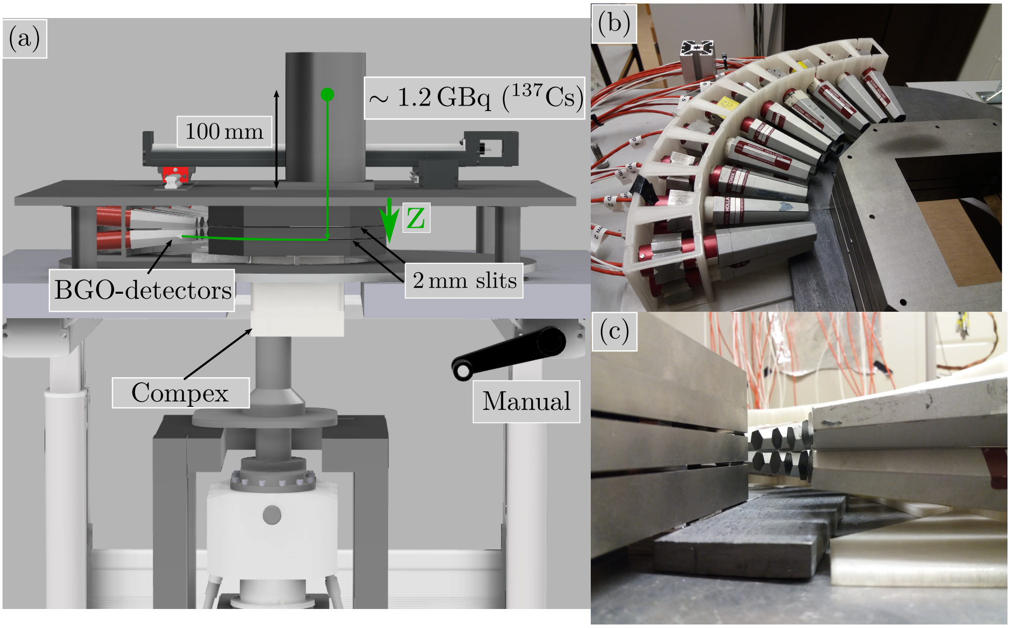

Figure 3.3: (a) The Lund scanning system and the working principle of the coincidence scan method used to determine the z-coordinate. Key measurements and components are indicated. (b) BGO detector configuration on its 3D-printed plastic holding frame outside the horizontal tungsten collimators. (c) BGO detector alignment with the slits and the complementary lead shielding underneath the tungsten.

trated in Fig. 3.3(a). Mounted in a tungsten collimator, a strong ^{137}Cs source creates a pencil beam of γ rays directed precisely onto the Compex germanium detector. Weighing about 25 kg, building a system that was able to sustain and move the tungsten collimator over a surface which determines the (x, y) coordinates of the interaction, in an automated and precise manner, posed a challenge. Details on this (x, y)-positioning system, e.g. how the movement of the collimator is controlled and its interplay with the data acquisition system, is described in Appendix A.

Two 2 mm slits in between horizontal tungsten collimators surround the germanium detector and restrict coincidence measurements between the germanium detector and ancillary Bismuth-Germanate, *BGO*, scintillator detectors to Compton scattering angles of $\sim 90°$. The BGO detectors, on loan from Gammapool and originally from the EUROBALL inner ball BGO detectors, are arranged in two rows of ten in a quarter of a circle outside of the horizontal collimators as shown in Fig. 3.3(b) and (c). Mounted on a dedicated 3D-printed frame, each row of BGO detectors sits at the height of the center of a slit and

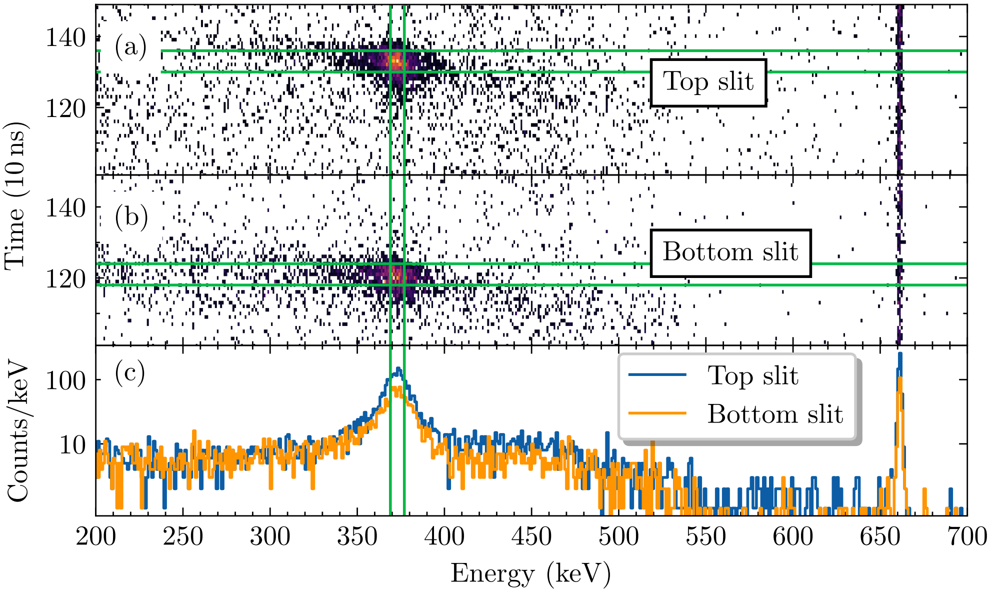

Figure 3.4: Germanium detector energy-time correlations for the top (a) and bottom slits (b) and their projections onto the energy axis (c). Green horizontal and vertical lines indicate the time and energy gates applied to extract 90°-scatter coincidence events.

only sees the germanium detector through the respective slit. Aided by the known energy deposition in the $\sim 90°$-scattering events (373 keV followed by 288 keV), two z coordinates, one from each slit, may be extracted during the same measurement from detected coincidences.

Different coincidence conditions and shielding configurations were evaluated in order to achieve best signal-to-background ratio. Due to the poor energy resolution of the BGO detectors, correlations between the deposited energy in the germanium detector and the associated digitised time with respect to trigger served as the way to extract the 90°-scatter coincidence events. This is shown in Fig. 3.4(a) and (b). Here the energy-time correlations display a distinct region of high yields for the top and the bottom slit. These peaks represent the 90°-scatter coincidence events. Random coincidence events, stemming from scattered γ rays which in different ways reach the ancillary BGO detectors, surround the peaks of interest. The coincidence yield as well as the signal-to-background ratio are lowest for the bottom slit which can be seen in Fig. 3.4(c). This may be explained by the larger amount of germanium material, the original and the scattered γ ray, had to traverse to reach the BGO detectors. In order to extract as clean data as possible, a tight energy gate of [369, 377] keV and time gates, typically 60 ns wide, set individually per slit and (x, y) coordinate, were applied. These are indicated by the green horizontal and vertical lines in Fig. 3.4.

In addition to arranging the horizontal tungsten collimators such that as much material was present above and below the BGO detectors, complementary lead bricks were placed underneath the tungsten, as depicted in Fig. 3.3(c). Their purpose is to further suppress the random background coincidences. In its final configuration, from the bottom up, the horizontal tungsten collimators (which have a depth of 50 mm) have a thickness of; 19 mm, 13 mm, 13 mm and 19 mm. The two slits, between the first and second, and second and third collimators, are created with 2.0 mm thick aluminium spacers resulting in a distance of 15 mm between the centres of the slits.

For the study of the Compex detector, two sets of measurements were finally undertaken with the Lund scanning system. These are reported in Paper II. In a front-face scan, the detector crystal geometry could be verified in detail. In addition, a homogeneous detection efficiency across the front face of the detector, including the corners, could be probed. In a coincidence scan, the pulse-shape response of a Compex germanium crystal was characterised by investigating the rise time, defined as the time it takes for the pulse to rise from 10% to 90% of its amplitude, at different positions within the crystal. In combination with source measurements, in which distributions of pulse rise times at three different energies were determined, it was concluded that the Compex detector has pulse shapes typical for that of a coaxial detector with no indications of incomplete charge collection.

3.3 Compex's energy resolution and efficiency

Energy resolution and detection efficiency of the Compex detector was studied by means of source measurements. During factory acceptance tests conducted at the *Mirion Technologies (Canberra)* Lingolsheim facility, spectroscopic performance of all the crystals in the four Compex detectors were evaluated. Full-energy peak efficiency measurements as functions of energy were performed for one Compex detector in Lund. In the current section, the main results of the source measurements, presented in Paper II, are compiled in a different format. The comparison with another Clover germanium detector, previously used with TASISpec, is highlighted.

One of the main results from the measurements in the factory acceptance tests,

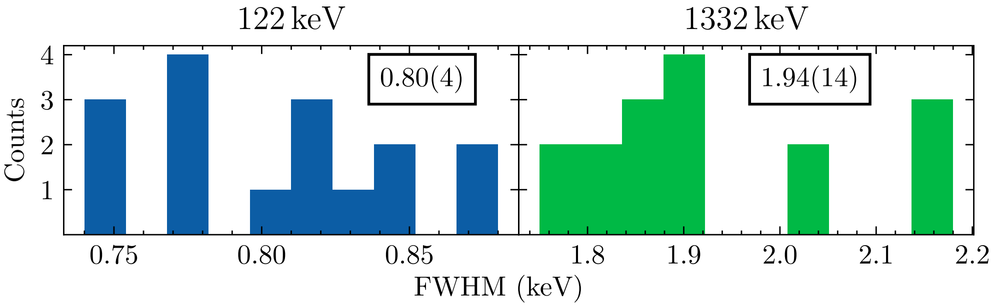

Figure 3.5: Energy resolution for all crystals of the four Compex detectors at 122 keV and 1332 keV. Values in boxes are computed mean where the uncertainties given have been calculated as the standard deviation from the mean.

which were carried out with analogue electronics, are given in Fig. 3.5. Here the distributions of energy resolutions at 122 keV and 1332 keV for each individual crystal of the four Compex detectors are shown. The resolution obtained at low energy is in general better than other Clover detectors previously used with TASISpec, e.g. the EUROGAM II [34] with 1.03(2) keV at 122 keV while at 1332 keV it is comparable. This is in large thanks to the lower capacitance of the Compex crystals which in turn is mainly explained by a shorter length, namely their 50 mm in respect to the 70 mm in the crystals of the Clover detectors.

Precise measurements of the full-energy peak efficiency of the Compex detector were performed in Lund with the so-called external trigger method [47]. In the external trigger method, by using a ^{60}Co source and a reference detector, the absolute full-energy peak efficiency at 1332 keV, at 25 cm from the end-cap, was determined. The yield of coincident 1173- and 1332-keV γ rays to non-coincidences were compared and a correction factor, since the γ rays have angular correlations, was included. Derivation of the method along with a description of how the correction factor was determined in simulations can be found in Appendix B.

Efficiency curves for the Compex detector were also determined in the Lund measurements. This was achieved by taking spectra with ^{152}Eu and ^{133}Ba sources and extracting the relative efficiency of several transitions by normalising to tabulated intensities [48]. The function introduced in Ref. [49]:

$$\ln \varepsilon(E_\gamma) = ((A + B \cdot x + C \cdot x^2)^{-G} + (D + E \cdot y + F \cdot y^2)^{-G}))^{-1/G}, \tag{3.1}$$

where $x = \ln(E_\gamma/100), y = \ln(E_\gamma/1000)$, and E_γ is in keV, was then fitted to the data. Following the fit, the points and the fitted function were normalised to the absolute value at 1332 keV, determined in the external trigger method.

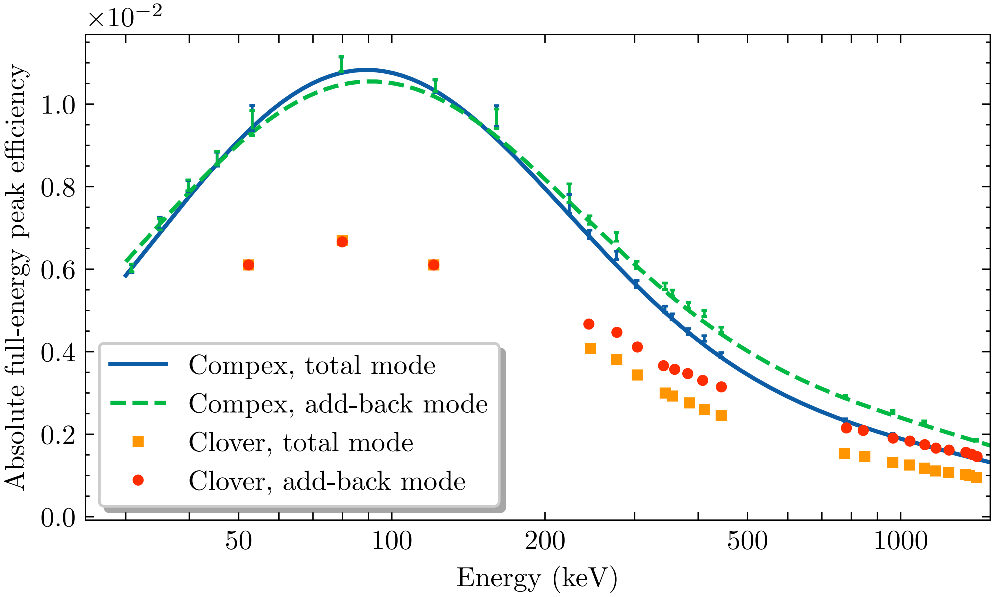

Figure 3.6: Full-energy peak efficiency curves in the total and add-back modes of detection for the Compex detector compared to the Eurogam II Clover detectors. For the Compex detector, error bars represent the data points while the lines stem from fits. The curves for the Clover detectors have been adapted from Fig. 3 in Ref. [34].

Figure 3.6 compares the obtained efficiency curves for the Compex detector in the total and add-back detection modes to the corresponding data of the Eurogam II Clover. In the total mode, each crystal works as an individual detector and their efficiencies are summed. In contrast, in the add-back mode, if multiple hits are coincident within 100 ns, their energies are added and the efficiency is then given for the whole detector. It is quite evident from the curves that the Compex detector provides a considerable improvement in detection efficiency up to ∼ 1 MeV. Furthermore, the fitted function for the Compex detector in the add-back mode has a difficulty to reproduce the data at ∼ 80 keV.

At 1332 keV, the Compex and the Eurogam II Clover assume values of $1.48(2) \cdot 10^{-3}$ and $1.02(3) \cdot 10^{-3}$, in the total mode, respectively. This relatively large discrepancy can be mainly attributed to difference in solid angle coverage. The four crystals of the Clover detectors have a tapered cylindrical surface (50 mm diameter before tapering) tailored for use in a spherical detector geometry. This reduces their solid angle of coverage with germanium considerably compared to the Compex detector which has a front face of $50 \times 50\,\mathrm{mm}^2$. It should further be noted, that the Clover detector has a length of 70 mm and sees a gain in efficiency at higher γ-ray energies. In contrast, the 50 mm length of the Compex detector is optimal for best efficiency up to $\sim 1.5\,\mathrm{MeV}$.

The resolution together with measured peak shapes of the Compex detectors, demonstrate the potential boost in spectroscopic performance attainable with Lundium. The measured efficiency curves further indicate the success of the Compex design.

3.4 Prospects

The use of the Compex detectors in Lundium promises an improved energy resolution and a substantial increase in detection efficiency at low-to-intermediate photon energies. Ongoing work with the Lundium chamber revolves around efforts to to further increase sensitivity by suppressing different sources of background signals.

Operation with higher rates of decays in the silicon detectors, which can be anticipated with increased beam intensities, may increase randomly correlated chains and/or aggravate the search for decay chains with longer correlation times. To overcome these challenges, the pitch size of the new 0.3 mm thick implantation DSSSD will be decreased from 1.8 to 1.0 mm: 32×32 strips become 58×58.

The germanium detector placed behind the implantation silicon detector, experiences by far the highest rate of radiation as it to a large degree sits in direct view of the radiation induced by the reactions from the target station. Add-back of energies deposited in neighbouring crystals may then be performed with unrelated randomly coincident hits and result in impaired data. As a mean to confront this potential problem, the Compex detector which will sit at this position will be electrically segmented into four segments at the outside of the crystals. Aided by an improved positional resolution possible with this detector, optimal add-back routines will be characterised in conjunction with the scanning system in order to suppress add-back of randomly coincident hits.

Installations of passive and active shielding serve as other means to suppress background radiation. In the original TASISpec setup, the germanium detectors were exposed to high background radiation fields induced by the intense heavy-ion beam incident on the actinide target and, especially, the beam dump inside TASCA. The radiation includes fast and slow neutrons, which induces defects which then trap charge carriers in the germanium detectors and degrades their performance in a dose-dependent manner. Minimising the effects of neutron damage involves the installation of passive shielding in TASCA. Firstly, a concrete wall, able to absorb neutrons has been installed in the TASCA experiment cave. Secondly, a combination of plastic and lead in a pre-chamber connecting the TASCA outlet and the decay spectroscopy setup provides further shielding. For long-term use, the Compex detector cryostats are equipped with heating elements, such that annealing can be readily performed via service and pumping ports and restore the damage caused by neutrons. It is worth noting that since each crystal in the Compex detectors is encapsulated, they are significantly easier to maintain and, for instance, in the case one crystal breaks. Another important effect of the passive shielding is their intrinsic background suppression of the hits in the germanium detectors. As a consequence, the expected number of germanium hits stemming from random photons will be reduced during the periods of beam off in the pulsed structure of the UNILAC beam at GSI, cf. Fig. 4.3.

Yet another effort to improve the signal-to-background ratio in the Compex detectors is the installation of BGO anti-Compton suppression shields. As a consequence of Compton scattering, some γ rays avoid full absorption and only deposit a fraction of their full energy in a crystal. Those unwanted events may be vetoed by surrounding BGO detectors in an active shield. GEANT4 simulations have been guiding the design of the anti-Compton shield [50], and experimental measurements yield an improved signal-to-background ratio of $\sim 50\%$ for a ^{137}Cs source for a BGO-shielded Compex detector [51]. At the time of writing, the Lundium chamber is in active development. The first prototype sees its commissioning at GSI in 2022 [52].

Chapter 4

Experiment

Tools & Settings to Produce the Best Data

A successful experiment relies on the quantity and quality of the data acquired. To understand what good data quantity and quality means for the current work, it is necessary to know the experimental objectives. There were three central objectives listed in the proposal to obtain beam time at the accelerator facility [53]:

- Define precise Q_α values along ^{287,289}Fl decay chains by means of high-resolution α-photon coincidence spectroscopy and settle a proposed α branch into ^{277}Hs [24].
- Search for and eventually discriminate $E1$ γ-ray transitions or K X rays stemming from highly K-converted $M1$ transitions along the ^{287,289}Fl decay chains.
- Search for the decay chain of the hitherto unknown $N = 176$ isotope ^{290}Fl, to probe the evolution of shell-stabilizing effects at proton number $Z = 114$ towards $N = 178$ and $N = 184$ [54].

In order to achieve the experimental objectives, the more Fl-decay chains produced the better. To facilitate and strengthen nuclear structure interpretations

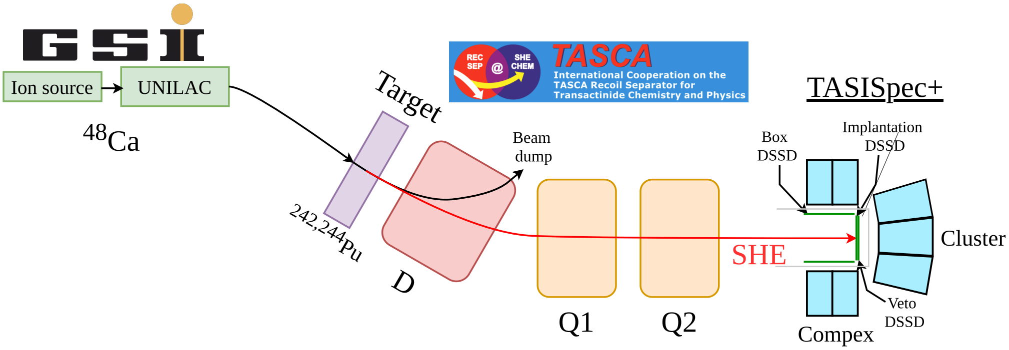

Figure 4.1: Schematic of the flerovium experiment. The GSI accelerator facility provided a high intensity beam of ^{48}Ca. In the TASCA experimental hall, the beam impinged on a plutonium foil mounted on a target wheel. The TASCA separator, comprising a dipole (D) and two quadrupole (Q) magnets, was used to pre-select the produced superheavy-element (SHE) ions following the rare fusion events. The SHE 114, flerovium, was implanted into a DSSD of the decay station TASISpec+. By detecting charged particles in the DSSDs and photons in surrounding germanium detectors (Compex and Cluster), the flerovium decays were identified and investigated in detail. See Chapter 4 for more details.

drawn from the acquired data, as much relevant information as feasible should be collected, in particular along the observed Fl-decay chains. In parallel, conflicting data from background sources should be kept to the minimum. The current chapter highlights efforts related to the setup employed and the settings applied, made to assure a successful experiment.

The experiment was conducted at the GSI Helmholtzzentrum für Schwerionenforschung, Darmstadt, Germany, and a schematic overview is given in Fig. 4.1. Ions of ^{48}Ca^{10+} were extracted in the Electron Cyclotron Resonance (ECR) ion source and accelerated with the Universal Linear Accelerator (UNILAC). The accelerated beam ions were directed to the TASCA experimental hall and its target station. Thick layers of the rare actinide isotopes ^{242,244}Pu were deposited onto four arc-shaped segments of a target [55]. To allow for a high beam intensity, the target wheel was rotated synchronously with the pulsed beam structure of UNILAC [56]. Flerovium isotopes were produced following ^{48}Ca+Pu fusion-evaporation reactions. The flerovium evaporation residues (EVRs) recoiled out of the target and into the TASCA gas-filled separator [57] filled with 0.8 mbar of helium. By means of TASCA's magnetic dipole field, the sea of unwanted beam-like and target-like nonfusion reaction products were separated from the precious flerovium ions based on their different magnetic rigidities. Following the dipole magnet, two quadrupole magnets focussed the EVRs such that they could be efficiently transmitted into the TASISpec decay station. Here the flerovium ions were implanted into one of its double-sided silicon strip detectors (DSSDs). The characteristic radioactive nature of the flerovium nuclei, i.e., sequences of α decays terminating with spontaneous fission, served as the fundamental principle of their identification. Simultaneous to the identification, the particle-photon spectroscopy performed with TASISpec provided the insight into the nuclear structure along the Fl-decay chains, forming the main objective of the experiment.

For a thorough and well-written introduction to the full experimental setup, the reader is recommended Chapter 4 of Ulrika Forsberg's thesis [2]. The data set of that experiment on element 115, moscovium, decay chains, was used in an analysis forming Paper I. The current chapter aims to complement the previous work by specifically emphasise relevant parts for this flerovium experiment. An upgraded version of the setup, *TASISpec+*, was employed in the current experiment. It is the topic of Sec. 4.1, which describes its improved sensitivity and means to veto background sources as well as tools to aid the understanding of the acquired data. A revised *beam shut-off routine*, important to preserve a low-background environment during the decays of candidate Fl chains, is introduced in Sec. 4.2. For the remaining part of the chapter (cf. Sec. 4.3), the experiment beam time is described. After a general introduction, the validation of experimental parameters using Pb and Hf targets in so-called *parasitic mode* is presented. The validation of the quadrupole magnet settings, central to assure the optimal transmission of the produced Fl nuclei through TASCA, is emphasised. The main part of the experiment rounds off the chapter. Beam energy and intensity at the Pu target, both crucial in the production of the Fl nuclei, are in focus. Finally, first results of the experiment are summarised and the operation of the beam shut-off routine is evaluated.

4.1 TASISpec+

The TASISpec version employed in the current experiment, had evolved from the original [2, 33] [see Fig. 3.1(a)], on the way towards its final upgrade Lundium (cf. Chapter 3). It is therefore denoted TASISpec+ in this context. The core of TASISpec+, as for its predecessor, is a cube-like arrangement of silicon detectors as shown in Fig. 4.2(c). Ions of the superheavy nuclei were implanted into a 0.31-mm thick (0.52 mm thickness in the previous experiment [26]), 32×32-strip DSSD, hence denoted *implantation-DSSD*. Four additional 0.97 mm thick, 16×16-strip DSSDs were placed upstream, denoted *box DSSDs*. An addition to TASISpec+ was a second 0.31-mm thick, 32×32-strip DSSD placed behind the

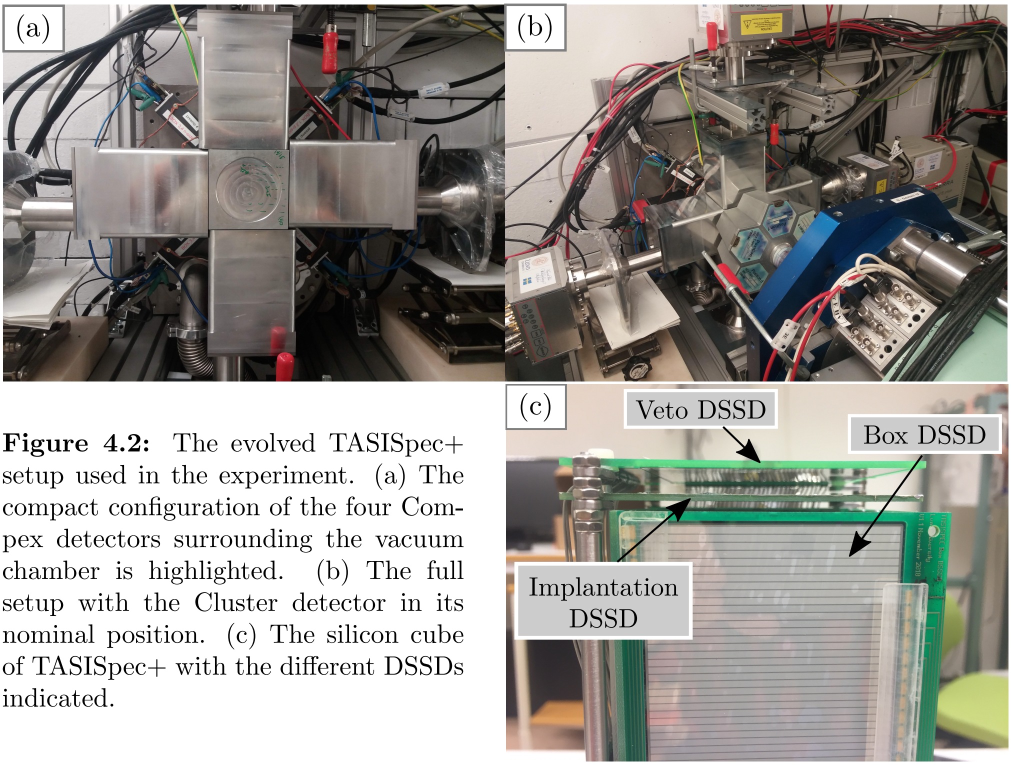

Figure 4.2: The evolved TASISpec+ setup used in the experiment. (a) The compact configuration of the four Compex detectors surrounding the vacuum chamber is highlighted. (b) The full setup with the Cluster detector in its nominal position. (c) The silicon cube of TASISpec+ with the different DSSDs indicated.

central implantation DSSD (rotated and slightly offset). This detector is denoted as the *veto DSSD* since it allowed to veto unwanted background radiation. It could be β decays of nonfusion reaction products during beam-off periods as well as other punch-through events induced by scattered particles of the gas in the separator from signals of implanted ions and their decays [Sec. 3.1. Paper III, Sec. III. B. Paper V].

Five composite germanium detectors were placed closely behind each of the five sides of the DSSD cube outside the vacuum chamber. As before, a seven-crystal Cluster detector [36] sat behind the implantation DSSD. The biggest change to TASISpec+, was the use of four novel Compex detectors [Paper II, Chapter 3] behind each of the box DSSDs. This configuration, with anticipated increased photon-detection efficiency, is shown in Fig. 4.2(a-b).

The signals from the 256 DSSD channels were processed with custom-made 32-channel charge sensitive preamplifiers [58] such that the linear dynamic range was $\sim 35\,\text{MeV}$, $\sim 16\,\text{MeV}$ and $\sim 8\,\text{MeV}$ for the implantation, box and veto DSSDs, respectively. The readout of the preamplified signals was performed with the GSI-developed FEBEX [59], version 3B, 50-MHz, 14-bit sampling

ADCs. Energy and time from its FPGA were recorded along with 80-µs long traces of the preamplifier signals. The 23 germanium detector channels were processed by five commercial 16-bit, 100-MHz SIS3302 sampling ADCs[1]. While, it is in principle possible to write the raw preamplified germanium signals to disk, only flat-top energy, baseline, time, and a pile-up recognition flag were recorded, due to known issues with long dead times of the whole data acquisition system.

The data acquisition system was based on the GSI Multi-Branch System (MBS) [60]. List-mode data was generated following two types of triggers for the main experiment: (i) a strip of the implantation DSSD registered a signal of $\gtrsim 150\,\mathrm{keV}$. (ii) a strip in one of the four box DSSDs detected a signal in excess of $\sim 5\,\mathrm{MeV}$. The latter, which was a new addition in the present experiment, was implemented in order to avoid missing events within which α particles emitted upstream and then entering the box DSSDs, due to them potentially depositing an energy below a $\sim$ 500-keV threshold in the implantation DSSD set in previous TASISpec experiments. A sophisticated solution was required since there was no option to implement different thresholds for passive and active triggers in the FEBEX firmware. All the channels of the box detector n-side strips were duplicated using CERBERUS cards[2]. One output took the standard route connected to a FEBEX card, while the other was connected to a *mesytec* MSCF module[3] which generated this special trigger signal. The energy threshold was calibrated by means of a $\sim 5\,\mathrm{MeV}$ peak of a four-line α source (^{148}Gd, ^{239}Pu, ^{241}Am, ^{244}Cm). Due to the possibility to operate with low trigger thresholds at $\sim 150\,\mathrm{keV}$ in the implantation DSSD, this box high-energy trigger turned out to be redundant in the current experiment. It is worth noting that signals above a threshold of $\approx 150\,\mathrm{keV}$ for strips in the box DSSDs were recorded once an event triggered. This allowed for the measurement of low-energy internal conversion electrons emitted into box DSSDs. Their detection played a major role in the outcome of the experiment.

General event information, such as beam-on or beam-off status, target segment, trigger type, and chopper[4] in or out were written to the data stream with an input/output register module[5]. A scaler module[6] was also included in the data acquisition system with which rates of various types of events could be investigated in more detail. Figure 4.3 presents the rate of events in the DSSDs

---

[1] https://www.struck.de/sis3302.htm

[2] https://github.com/fmessi/DataSheet_Cerberus

[3] https://www.mesytec.com/products/nuclear-physics/MSCF-16_F_V.html

[4] An electrostatic deflector near the ion source capable of cutting off the beam as quickly as possible.

[5] https://www.caen.it/products/v977/

[6] https://www.caen.it/products/v830/

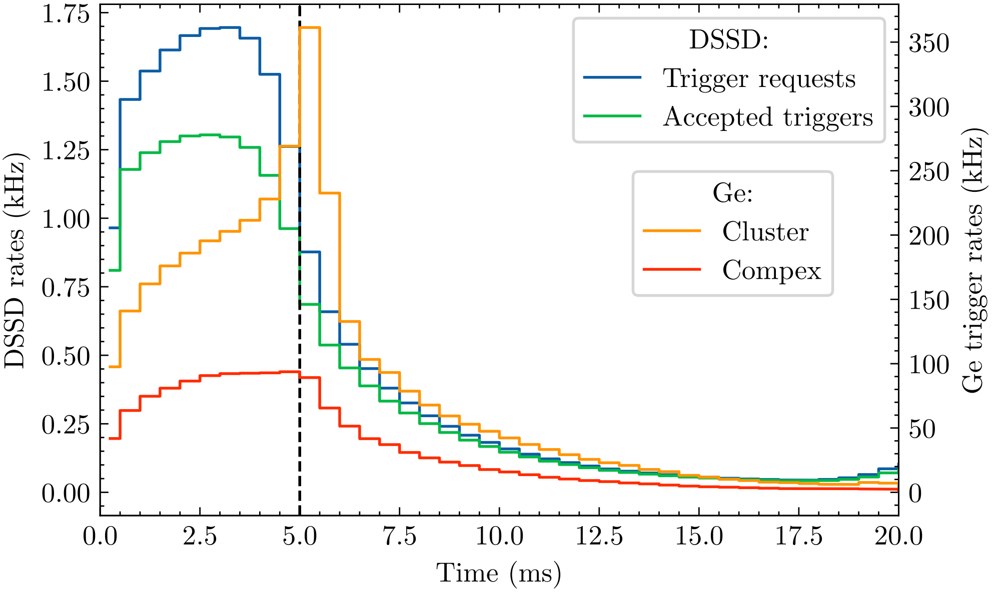

Figure 4.3: Rate of trigger requests and accepted triggers of the DSSDs (left axis) and Ge-trigger rates (right axis) for single crystals in the Cluster and Compex detectors as a function of time after the start of the beam pulse. End of beam pulse is denoted by the dashed vertical line. The beam was pulsed at 45 Hz with a $\sim 3.2\,\mathrm{p}\mu\mathrm{A}$ intensity on the Pu target.

and single crystals in the Cluster and Compex Ge-detectors as a function of time after the start of the beam pulse (5 ms beam on, 15 ms beam off) for the main part of the experiment. Here, *trigger requests* are those signals sent to the data acquisition system when a signal fulfills the trigger thresholds discussed in the previous paragraph. Unless the system is busy writing data from a previous event due to *dead time* (Δt_{dead}), it will generate an *accepted trigger* signal and process the current event. The difference between the rate of trigger requests N_{request} and accepted triggers N_{accept} can be used to determine the system dead time according to eq. (4.1).

$$N_{\mathrm{request}} - N_{\mathrm{accept}} = N_{\mathrm{request}} \cdot N_{\mathrm{accept}} \cdot \Delta t_{\mathrm{dead}} \tag{4.1}$$

Based on the DSSD data for beam-on periods, a dead time of 120 µs was obtained for the experiment. This dead time is longer than desired for an optimal data acquisition system, but could provide a consistent explanation for missing implantation and α-decay signals as described in Sec. III. A. of Paper V. The Ge-trigger measurements provided an important understanding of background and random correlations of photons with respect to the event time following the beam pulse. A conclusion from these measurements was that due to many expected random correlated photons during beam-on periods and within 5 ms after the beam pulse, these were not included in the final interpretation of the decay chains. Thanks to the pulsed beam structure of the UNILAC beam, the background rates in both the germanium detectors as well as the silicon detectors, were suppressed significantly. As a means to further ensure a low background environment when the decays of the flerovium nuclei took place, the beam could be removed based on a beam shut-off routine as part of the data acquisition system.

4.2 Beam shut-off routine

The identification of superheavy nuclei is contingent on the detection of decay chains with certain characteristics. It is therefore desirable to suppress the background to the largest extent possible during candidate events. For the present work, this involves using an electrostatic chopper to bend the beam off axis near the ion source and thus stop further implantation events.

Experiments at TASCA first utilised, what is here denoted a *beam shut-off routine*, for experiments running 2012. During and close to the beam pulse of the UNILAC accelerator, germanium detectors are overloaded with background radiation, cf. Fig. 4.3. The beam shut-off routine was therefore crucial to minimise randomly correlated photons in the nuclear spectroscopy experiments along element 115, moscovium, decay chains [25, 26, 61] conducted at the time. Upon detection of an [8.5,11.0] MeV α-particle like signal during periods of beam off in an n-side strip of the implantation-DSSD, the 2012 routine to shut off the beam was activated. In contrast to the previous TASISpec experiment in 2012, all the channels of TASISpec+'s DSSDs now employed FEBEX digitiser cards for readout[7]. FEBEX firmware upgrades (trapezoidal energy filter implemented on the FPGA) and technological developments (card for input/output communication), opened the door for a more sophisticated routine in the current experiment.

In order to establish the non-randomness of Fl-decay chains, it is crucial to detect the fission event terminating the chain at times without beam. This was noted in Ref. [25] when applied to ^{289}Mc-decay chains, which similar to the Fl chains, typically only have one or two α-decay steps, but in addition can have long first

---

[7] In the 2012 TASISpec experiment, the n-side channels of the DSSDs were processed with mesytec analogue electronics on the VME branch of the data acquisition system.

correlation times, of several seconds. For the Fl-decay chains, the implemented routine thus has less chances to shut off the beam before the fission terminates the chain, in contrast to the case of the five-α long ^{288}Mc-decay chains. For the new routine, this requires a high efficiency to identify Fl-decay chains while at the same time it should only minimally trigger on background signals. It is worth noting, that experiments employing continuous-beam rely on the fact that a preceding α to the fission has triggered a routine to shut off the beam, while for the pulsed UNILAC beam there is in any case at least a 75% chance that the fission will occur during the calm beam-off periods.

By means of correlated implantation signals on the pixel level and subsequent α decays, combined with tailored energy and time conditions, separate for periods of beam on and beam off, the refined routine is able to allow longer correlation times without excessive false triggers. Furthermore, by employing neighbour-strip add-back and a simple box reconstruction procedure, the routine is more efficient. Appendix D reports on the identification efficiency of Fl-decay chains in the current experiment wherein the impact of the beam shut-off routine is demonstrated.

Aside from being implemented into the main readout routine of the MBS data acquisition system, the beam shut-off routine was implemented into a testing framework wherein the logics of the routine could be scrutinized. Being an ingredient in the MBS program which writes data to disk, it was furthermore essential that it could be checked for errors. The routine was therefore integrated into the data analysis software, Go4 (see Chapter 5). This further enabled optimisation and detailed monitoring of the routine's input parameters based on the 2012 TASISpec data. As another means to verify the routine's functionality, candidate Fl-decay chains were printed to the screen during the experiment, which also meant that their detection could be followed live from the control room. Some details on hardware and software implementations related to the beam shut-off routine can be found interested readers in Appendix C.

4.3 Beam time

The beam time was conducted in two experimental runs; the first in 2019 and the second in 2020. The timelines for the two experiments are illustrated by the average beam current in Fig. 4.4. Prior to the two days of setting up the TASISpec+ decay station for the beam time, so-called *dry-runs* were conducted. In these dry-runs, radioactive sources were installed inside TASISpec+'s vacuum chamber, basic consistency checks were made, firmware parameters were tuned

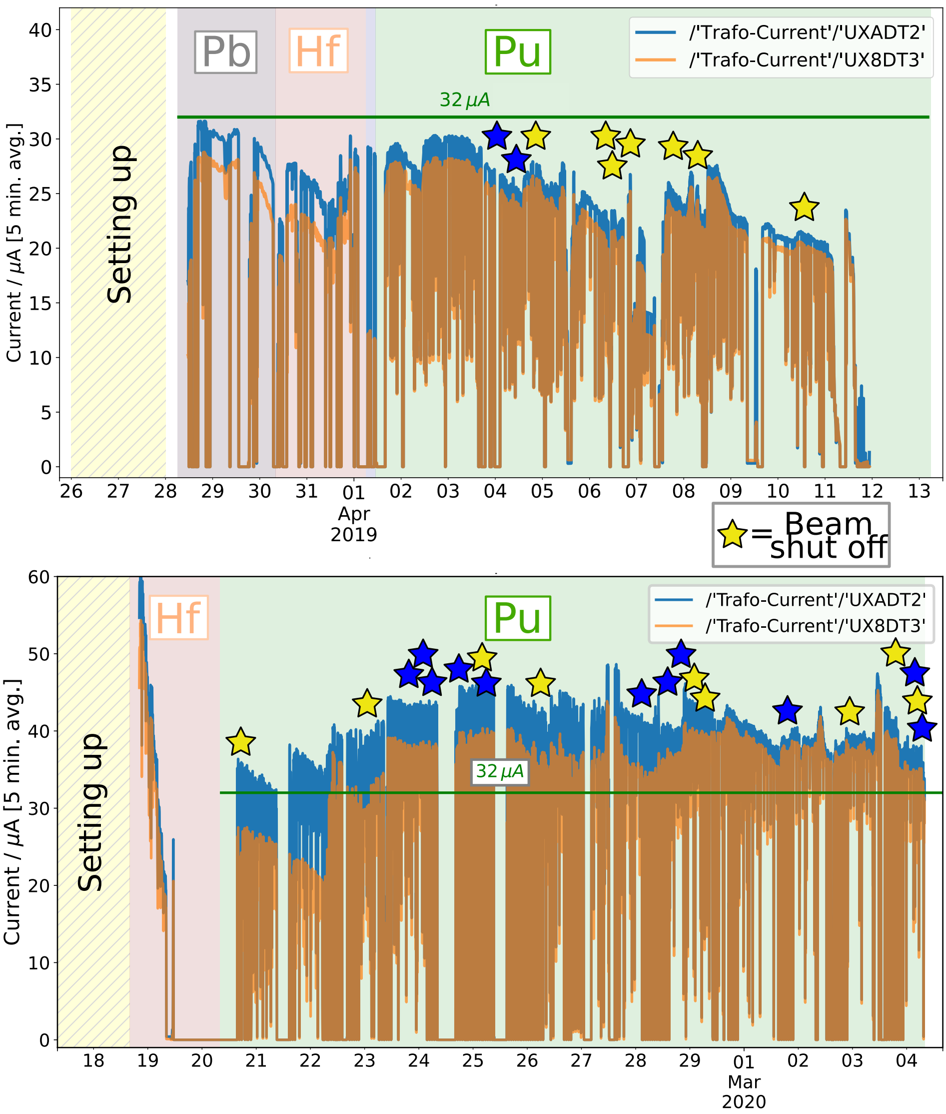

Figure 4.4: Experiment timeline illustrated by means of the average pulsed beam current throughout the first run in 2019 (top) and second run 2020 (bottom). The blue (UXADT2) and orange (UX8DT3) coloured lines represent the current measured with induction coils before the TASCA experimental cave and the target wheel, respectively. The green horizontal line illustrates a reference current of 32 μA. Coloured background indicates different parts of the experiment and for which different target materials were installed. Yellow (blue) stars represent identified Fl-decay chains which did (did not) activate the beam shut-off routine.

and calibration data was acquired. These subjects form parts of Chapter 5, parts of Paper III and most of Paper V.

Throughout the experiments, the beam current, which is displayed in Fig. 4.4, was monitored using two induction coils. These were located just outside the TASCA experimental cave, and inside, close to the target wheel, denoted *UX-ADT2* and *UX8DT3*, respectively. The beam was pulsed at a total frequency of 50 Hz, such that it was on for 5 ms and off for 15 ms. With a typical beam current of 32 μA measured at UX8DT3[8], an intensity of 5×10^{12} particles per second, time averaged over the pulsed beam structure, was attained on the installed targets. Starting the first run, fusion-evaporation reactions of ^{48}Ca on Pb and Hf targets during so-called *parasitic beam* were measured for two days each. For the main part of the two runs, the Pu material was installed on the target wheel during what is denoted *main beam* operation. In contrast to parasitic beam, where typically 5 Hz is directed to the actual experimental hall, during main beam operation it corresponds to 40-45 Hz[9].

4.3.1 Parasitic beam - Pb and Hf target

Central for the parasitic beam time was the validation of the TASCA quadrupole magnet settings and target segment information, together with the evolution of the digital signal processing of TASISpec+'s silicon detectors. These topics form the major part of Paper III.

The first experiment on superheavy elements at the TASCA gas-filled recoil separator combined with experiments investigating flerovium's chemical nature have been, alike the current experiment, performed using the ^{48}Ca+^{244}Pu reaction [24, 62–64]. The magnetic rigidity of Fl has therefore been established at 2.27 Tm. As part of a campaign preparing the nuclear spectroscopy experiment of Mc-decay chains in 2012, optimal quadrupole settings to focus and transmit fusion-evaporation recoils into TASISpec had been established [2]. Since the 2012 experiment, power supplies of TASCA's quadrupole magnets have been replaced and a new shield wall between the separator and focal plane have been constructed requiring TASISpec+ be moved downstream with respect to the focal plane of TASCA. The focussing scheme of the quadrupole magnets thus has to be reassured. The ^{206,207}Pb(^{48}Ca, 2n)^{252,253}No reaction was used and the

---

[8] The intensity of the ^{48}Ca^{10+} ions were attenuated with a factor 0.85(5) between the UX8DT3 measuring station and the target wheel. Thus, actual beam-on-target particle intensity (pμA) is obtained by multiplying with $0.85 \cdot 10^{-1}$.

[9] Either one or two other experiments run in parasitic mode with 5 Hz in parallel to the main experiment.

resulting settings are presented in parts in Paper III.

To explore which of the ^{287}Fl- or ^{289}Fl-decay chains revealed most promising nuclear structure results, a mixed target wheel of ^{242}Pu and ^{244}Pu segments was used in the main part of the first experimental run. In order to avoid isotopic assignment[10], i.e. relying solely on the decay characteristics measured in the observed Fl-decay chains, it was therefore important to correlate each implantation event with a specific target segment. Another purpose for the parasitic beam was hence to evaluate correlations between target segment and implanted nuclei. Comparing ^{252,253}No yields in the ^{48}Ca+^{206,207}Pb reaction served this purpose [Sec. 2., Paper III]. It turned out, that this correlation did hold, but not on a sufficiently high level to clearly be able identify the target wheel segment for a given implantation [Sec. II., Paper V].

The use of digital electronics for the preamplified signals of all silicon detector channels of TASISpec+ opens up access to decay characteristics of α-decaying nuclei with half-lives on the order of microseconds. For the present context, this possibility was first explored in the analysis of the 2012 moscovium data. Several microsecond α-decaying nuclei located North-East of Pb on the nuclear chart were produced in non-fusion beam-(actinide)target reactions. Nuclear structure studies along the ^{219}Ra-^{215}Rn-decay chain resulted in Paper I. Aside from that publication, being able to properly extract the energy and time of the so-called pile-up signals, played an important role for the current work from the following perspectives: (i) Resolving the decay characteristics of these implanted nuclei, and allowing for use of further reliable energy calibration points throughout the experiment. (ii) The understanding of their α-decay chains also facilitate the interpretations of the Fl-decay chains as e.g. *intruder decays*, i.e. background radiation detected within the correlation times of a Fl-decay chain, can be explained [Sec. III. B., Paper V]. (iii) Decays of elements $Z > 118$ may produce pile-ups [65]. Thus, in preparation for the search of new elements a well-developed digital sampling system is a key ingredient.

In the last two days of the parasitic beam time in 2019, a target of ^{nat}Hf[11] was used to produce nuclei in the region of ^{221}Th where there are several long α-decay chains with half-lives down to sub-microseconds. Facilitated by this data set, the digital signal processing of the pile-up signals was further refined, see Refs. [[66], Paper I, Paper III] and their supplemental material. Furthermore, this exploratory test now paves the way for a future experiment aiming for "Discovery and Spectroscopy of Neutron Deficient Pu isotopes and their Alpha-

---

[10] The most common $4n$ and $3n$ fusion-evaporation channels produce ^{286}Fl and ^{287}Fl for target segments of ^{242}Pu while correspondingly ^{288}Fl and ^{289}Fl for target segments of ^{244}Pu.

[11] In the 2020 run, a ^{50}Ti beam was used but only for a very limited time.

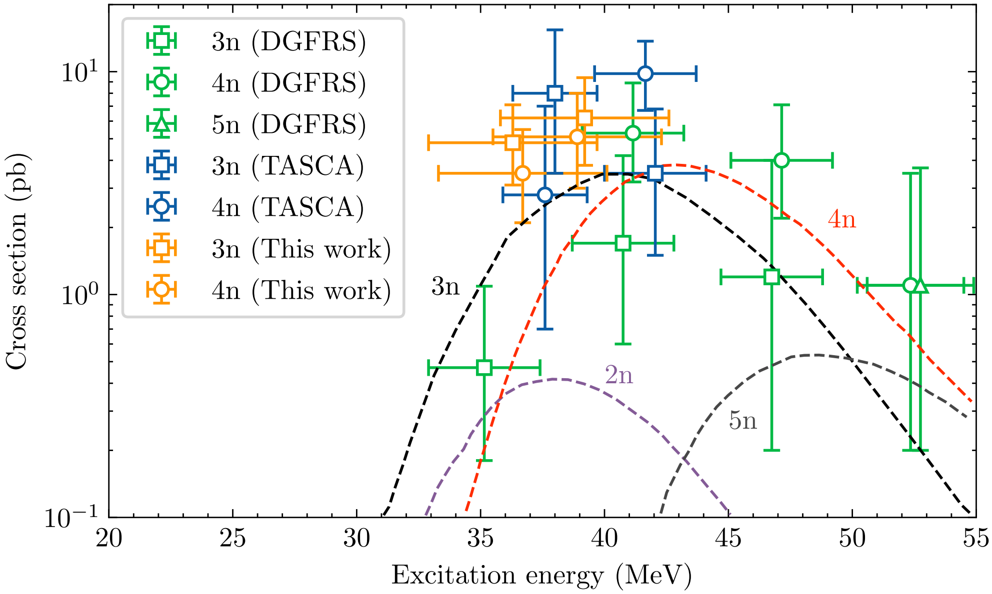

Figure 4.5: Cross sections for the production of various Fl isotopes in the ^{244}Pu(^{48}Ca, xn) reaction. Measured values and predictions have been taken from Refs. [62, 67, 68], while predictions, as well as measured points not found in the given references, have been digitised. Separate exit channels at similar excitation energies have been shifted to lower or higher energies for a better visual. The uncertainty in the cross section is statistical [69], while the uncertainties in the excitation energy have been taken from the range of energies probed through the thickness of the Pu target foil.

decaying daughters" [52].

4.3.2 Main beam - Pu target

The beam energy at the centre of the target is crucial to assure an appropriate excitation energy and therefore an optimised production cross section of flerovium nuclei. Suitable excitation energies were already known due to previously conducted measurements using the ^{48}Ca+^{244}Pu reactions performed at TASCA [62], but also ^{48}Ca+^{242}Pu reactions at the DGFRS in Dubna [67]. Figure 4.5 presents measured and predicted excitation functions in the ^{244}Pu(^{48}Ca,xn) reaction. It includes the measured cross sections from the present experiment. Those calculations are described in Sec. II. of Paper V, while the identification efficiency of Fl-decay chains used there is detailed in Appendix D. Aiming to produce first and foremost the odd-A ^{287}Fl and ^{289}Fl isotopes, the chosen excitation energies (cf. uncertainties given in Fig. 4.5) in this work were set to cover the maximum of the $3n$-evaporation channel while suppressing the $4n$. Using such an excitation energy would mean that the maximum of the $2n$ channel being explored simultaneously. This would produce the hitherto undiscovered isotope ^{290}Fl.

Due to an incident at GSI in 2018 (which actually postponed the current experiment), the UNILAC could only provide specific beam energies. Our experiments were bound to $E_{\text{beam}} = 6.02\,\text{MeV/A}$. Hence, foils were manufactured at the GSI target laboratory and installed such that the beam energy was degraded to reach a desired beam energy at the centre of the Pu-target foil, and thus excitation energy. Two sets of degrader foils were manufactured and used in the main part of the experiment to probe two excitation energies (see Fig. 4.5). Established procedures [2] based on SRIM [70] were used in determining the thickness of all degrader foils. For further details, Tables 1XXX in Paper IV, Paper V and Paper VI provide an overview of thicknesses of degrader foils, target backing foils, and target layers, as well as derived mid-target beam energies and collected beam integrals. It is worth mentioning, that under the current UNILAC operating conditions the beam focussing was both faster and saw a higher transmission throughout the accelerator complex.

The main experiment with the Pu target was conducted over a total of roughly 23 days, eleven in 2019 and twelve in 2020. Throughout these days the ^{48}Ca-beam intensity on the Pu target was the final decisive ingredient to guarantee a high production rate of flerovium nuclei. Here the efforts made by the GSI staff, responsible for the operation of the ion source and the accelerator, was imperative. Due to the ion source not working optimally, the beam intensity was poor during the first run in 2019, as can be observed in Fig. 4.4. This was compensated for in 2020 (2019) as a considerably larger beam intensity at UX8DT3 of $\sim 35\,\mu$A ($\sim 17\,\mu$A) was obtained which rendered a larger beam-particle integral of 4.9×10^{18} (2.1×10^{18}). In total 9 and 20 decay chains were measured in 2019 and 2020, respectively, which could be unambiguously assigned to isotopes of Fl. For the case of directly produced ^{289}Fl, this meant that with the current experiment the global data set of was extended from 9 to 24 decay chains.

Altogether, 16 of the 29 Fl-decay chains triggered the beam shut-off routine. The majority of the chains which did not trigger the beam shut-off (7 of 13) were attributed to events missed by the data acquisition system (see Appendix C and Chapter 5). Furthermore, the beam was shut off 462 times throughout the full experiment, which roughly corresponds to a rate of once per hour. Combined, these results demonstrate the successful implementation of the beam shut-off routine. Due to the low-background rate of α-decay signals in the energy range

[9.5,10.5] MeV during beam-off periods, a future improvement to the routine would be to not require preceding implantation signals (current bottleneck for false triggers due to their high rates) for beam-off α-decay events. This would make the routine less sensitive to missed implantation events.

Chapter 5

Data Analysis and Simulations

Enhancing and Extracting Data – Facilitating Interpretations

The main part of the data analysis was performed using the Go4 analysis framework [71]. The flow of the data analysis performed here builds on Refs. [2, 72]. Its main constituents are illustrated in Fig. 5.1. The implementation divides the data processing into three steps; unpacking, analysis, and correlation analysis. In the experiment (cf. Chapter 4), the MBS data acquisition generated binary List-Mode Data files (LMD) which were written to disk, $\sim 28\,\mathrm{TB}$ in total. As a first step, the binary contents were mapped into C++ data structures, in what was denoted *Unpack*. The files were dominated by the recorded pulses of the preamplifier signals, denoted traces, of all 256 channels of the DSSDs. These were processed in the unpacking step, thus making it the most computationally exhaustive part of the analysis. Therefore, this step was first run separately, to compress and save the data as ROOT TTrees, which could be directly read by the following analysis step. Each entry of the ROOT TTrees held general information on the event; beam status, time of event, event trigger type, and file name together with the collection of hits from all detector channels. These hits, corresponding to a preamplifier pulse, included most importantly a unique detector id, (uncalibrated) energy, and time with respect to trigger.

In the second, denoted *analysis* step, different efforts were undertaken to pre-

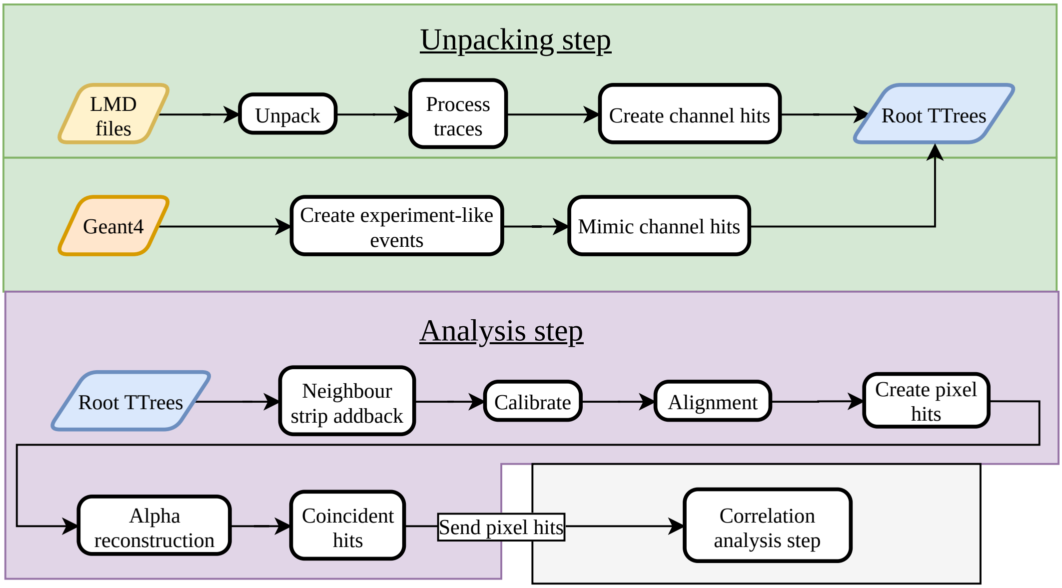

Figure 5.1: Flow of data analysis in Go4.

pare the data, focussing on the DSSDs, for the final correlation analysis. First, the energy of coincident hits in neighbouring strips of the DSSDs were added back while the strip with the smallest term was removed. Both DSSDs and germanium detectors were calibrated. Then, to account for a possible variation of the response of the detector channels over the course of the long experiments, a process denoted *alignment* was implemented such that best spectroscopic performance could be assured. The alignment provides a valuable enhancement of the data, which facilitates and strengthens nuclear structure interpretations. Different alignment procedures, not covered in detail in the papers, along with resulting systematic and statistical energy uncertainties are the centre of attention for the first part of the current chapter, Sec. 5.1. Moving on from the alignment procedures, hits of all strips in the DSSDs were then translated into corresponding pixel hits. In the following process, full energies of escaping α-particles, interacting in both implantation and a box detector, were reconstructed in an established procedure using SRIM [70], determined pixel-by-pixel deadlayers, and geometrical factors [2]. Concluding the analysis step, coincident hits in the box detectors and germanium detectors were connected to each pixel hit in the implantation DSSD before sending these into the correlation analysis.

The last step of the analysis, which is briefly introduced in Sec. 5.2, is the final essential means to extract candidate Fl-decay chains from the large data set. The most important and fundamental outcome of the data analysis is the tables summarising the information on identified correlated α-decay chains which were associated with decays of isotopes of flerovium. A great deal of events along the candidate decay chains were investigated manually "with a fine-tooth comb". This procedure, combined with statistical assessments of different event rates, facilitated interpretations and laid the foundation for all information provided in the tables. This is focussed in Sec. 5.2. Subsequent nuclear structure interpretations on the compiled data were then confronted with GEANT4 simulations in Sec. 5.3. These provided further means to facilitate the interpretations and brought confidence to the scientific claims. By tuning the parameters in the simulations, the experimental conditions were imitated. Integrated as another Go4 analysis step, parallel to the unpacking step, the simulated data was shaped into the experiment ROOT TTrees (cf. Fig. 5.1). Consistency between the simulation and experiment was established by investigation of the ^{211}Bi decay, having decay properties particular suitable for evaluating spectroscopic characteristics. Finally, efforts to provide accurate implantation depths of the flerovium nuclei are described in Sec. 5.4.

5.1 Alignment

In order to assess the performance of the detection of α particles along Fl-decay chains, with typical energies within $[9.0, 10.5]$ MeV, peaks in the implantation-DSSD energy spectrum of several well-known α-decaying nuclei with mass numbers $A \sim 220$ produced in nonfusion reactions were investigated. The energy spectrum was crowded with peaks in the $[6.0, 9.0]$ MeV region, many of them overlapping. The best, single and clean peak was the ^{213}Po peak at ~ 8.5 MeV together with the ^{212}Po peak at ~ 11.7 MeV. These lines were chosen for monitoring potential energy drifts in all implantation-DSSD channels as the experiment progressed. It should be noted that without the advancement of the digital signal processing extracting information from pile-up signals (see also Sec. 4.3.1), it would not have been possible to use the ^{213}Po peak due to its $\sim 4\,\mu$s half-life.

A special treatment of the energies extracted from pile-up signals was implemented in order to align them with those stemming from the common single-pulse signals. To exemplify this treatment, the data set in Paper I is used. As shown in Fig. 5.2(a), a trend between the energy of the second α particle in the pile-up signal, denoted E, and the time difference to first α particle, denoted Δt, in the pile-up signal was observed. A slope for $\Delta t \leq 15\,\mu$s along with an offset, $m = 30$ keV, with respect to the single-pulse signals (cf. $\Delta t > 70\,\mu$s) could be identified. Notable is that a similar trend was not seen for α_1, which points to

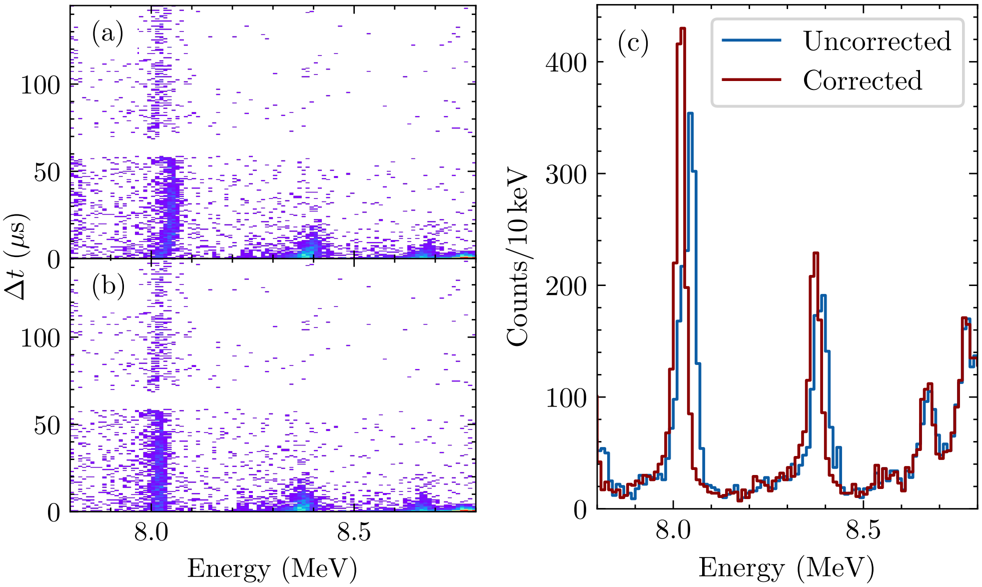

Figure 5.2: The time difference between two α-particle signals presented as a function of the energy of α_2 without (a) and with correction applied (b). The data acquisition system is in deadtime in the interval $\sim 60-70$ µs. (b) Uncorrected and corrected energy spectra compared.

the behaviour most likely being an artefact of an imperfect deconvolution step of the MWD routine [66]. The corrected energy following the implementation in Paper I is given in equation (5.1) and the improved spectroscopic quality is demonstrated in Fig. 5.2(b) and (c).

$$E' = \begin{cases} \frac{\Delta t}{15} \cdot m + E & \Delta t \leq 15\,\mu\mathrm{s} \\ m + E & 15 < \Delta t \leq 60\,\mu\mathrm{s} \end{cases} \tag{5.1}$$

Two different methods to align the ^{213}Po peak at ~ 8.5 MeV and the ^{212}Po peak at ~ 11.7 MeV for all channels as a function of experiment duration were investigated. The data set was either split into batches such that about all channels had one count in the ^{212}Po peak, or the data set was simply split with respect to the experimental run. Alignment factors for each peak and channel were calculated by taking the ratio of the centroid of the peak for the entire implantation-DSSD and the mean energy of the limited counts within a set energy range for the respective channel. It should be noted, that taking the mean of the small amount of counts in each channel was superior to determining the centroid by fitting Gaussians. Width of the peaks after applying the

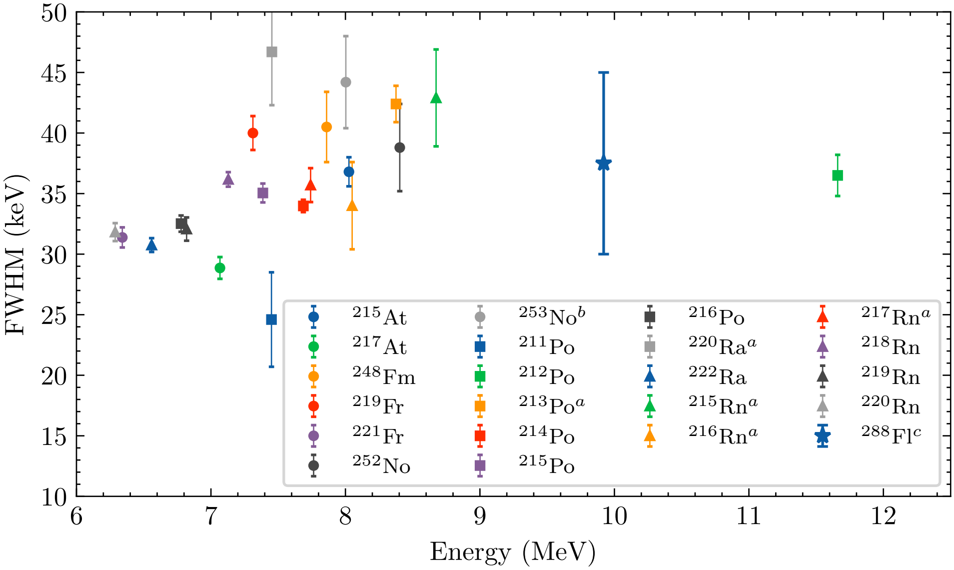

Figure 5.3: Full Width at Half Maximum (FWHM) of an ensemble of α-decay lines in the [6,12] MeV energy range. Legend indicates α-decay parent.

---

[a] α decay either first or second pulse in pile-up signal.

[b] Peak fitted from spectrum gated on photons.

[c] Fit on "Gaussian smeared" spectrum, cf. Fig. 2(j) of supplemental material in Paper IV.

alignment were visually investigated. The alignment following the data set split into batches with respect to the experimental run was deemed the best, likely due to its larger statistics.

High-energy ($[40, 400]$ MeV) alignment could be achieved by monitoring a bump in the energy spectrum around 300 MeV likely produced from the primary beam. Furthermore, special care was taken to align the full energy in reconstructed events with respect to the box detector the α particle escaped to for in-source measurements (cf. Ref. [61]) as well as centroid alignments to the full-energy peaks of the events, i.e. those when the α particle solely deposit its energy in the implantation detector for in-beam experimental data.

Except for the ^{212}Po line situated at ~ 11.7 MeV, the majority of peaks were smeared out in the $[6.0, 9.0]$ MeV energy range due to overlapping α-energy peaks. By means of α_1-α_2 correlations, tailored for the decay paths of interest, spectra clean from contaminating peaks could be extracted from the data set (see also Paper I) to determine statistical uncertainties. Figure 5.3 presents the Full Width at Half Maximum (FWHM) for an ensemble of peaks from the main part of the experiment. Three peaks with lower statistics, namely ^{248}Fm, ^{252}No and ^{253}No*, from the parasitic beam time with the Pb target as well as the ^{288}Fl peak, are included. The peak properties, centroid, volume and FWHM accompanied with errors were obtained with the program *tv* [73]. It can be seen that the FWHM increases from 31 to 42 keV and that the ^{288}Fl peak is in line with the trend. Furthermore, the performance of the digital signal processing of pile-ups is demonstrated as those peaks land on comparable widths to the rest. Reconstructed events were extracted by means of the same method. The "reconstructed peaks", processed by the reconstruction routine, showed an approximately constant behaviour at FWHM $\sim$ 150 keV across the whole energy range. Finally, the systematic uncertainty for α-decay energies were thoroughly assessed in conjunction with determining the so-called *recoil fraction*. This is detailed in Sec. III. E of Paper V.

All crystals - seven of the Cluster detector and sixteen of the Compex detectors - were operated in coincidence with charged-particle decays triggering the data acquisition. As their signals were processed by 100-MHz, 16-bit sampling ADCs, the parameters of its firmware trapezoidal routine to determine energy had to be optimised prior to the experiment. Several values of the averaging width and gap length, corresponding to the rise time of the trapezoid and the length of the flat top, respectively, were scanned while spectroscopic performance of the detectors were investigated. The decay constants of the preamplifiers were also thoroughly investigated, but later set to their factory values. The processing of the germanium data was done in line with what has been previously described in Refs. [72, 74].

The germanium detectors were calibrated with two-split linear functions based on several ^{152}Eu source measurements performed during the experiment. In-beam energy recalibrations were achieved by monitoring the 139.7 keV and the 1779.0 keV lines from (n,γ) reactions of ^{74}Ge and ^{28}Al, respectively, together with the 511.0-keV e^+e^- annihilation peak, all during beam-off periods and at least 10 ms after the beam pulse. Figure 5.4(a) shows the energy drift of most unstable channel in the Cluster germanium detector. In order to correct for its behaviour, first a reference mean within an energy range covering the peak centroid, here $[504, 514]$ keV, for a time interval with limited energy drifts was calculated. Then, for every bin on the x axis, the mean within the same energy range was calculated and associated with an alignment factor determined as the ratio of the reference mean to this value. The result of the rough alignment is illustrated in Fig. 5.4(b). Most importantly, the procedure shifts the peak such that it aligns with the other channels. This is shown in Fig. 5.4(c), where the "wiggly" channel is compared to a typical Cluster and Compex detector

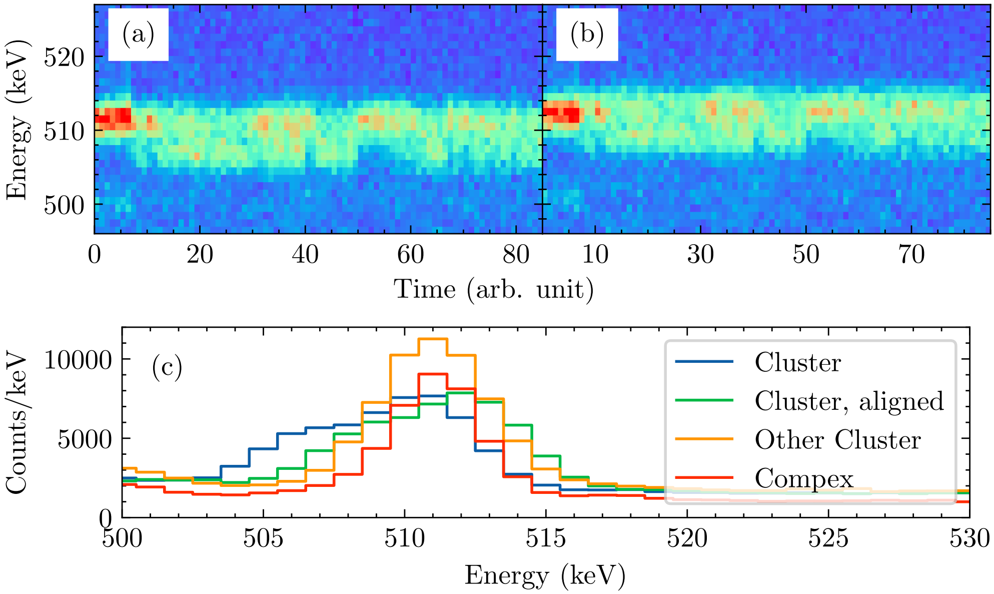

Figure 5.4: Drift of 511 keV peak for a channel in the Cluster germanium detector as a function of time throughout the second run of the experiment before (a) and after alignment (b) illustrated in a two-dimensional histogram. Each bin on the x axis represents the accumulated spectrum of 100 lmd files. (c) Energy spectrum zoomed in on the 511 keV peak for the Cluster channel depicted in (a-b) compared to another Cluster channel as well as a channel of a Compex detector.

channel.

Under experimental conditions with several potential sources of electronic noise as well as high count rates, the spectroscopic performance of the germanium detectors are not expected to perform in line with their specifications. In-beam, the Compex detectors typically had FWHM energy resolutions of ~ 1.5 and ~ 3.0 keV at 139.7 and 1779.0 keV, respectively, while corresponding values for the Cluster was ~ 2.0 and ~ 3.5 keV. The calibrated channels were evaluated on ^{73}Ge peaks at 595.9, 867.9 and 1204.2 keV and obtained centroids were by margin within the assigned systematical uncertainty of ±1 keV of the tabulated values, while a conservative uncertainty of 2 keV was assigned drifting channels.

5.2 Extracting Fl-decay chains

The signals of implanted recoiling ions and those of subsequent emissions of α-particles or terminating spontaneous fission events in the same detector pixel served as a tagging technique in the identification of decay chains stemming from flerovium isotopes created in fusion-evaporation reactions. The search criteria, i.e., the energy and time windows, used to discriminate the correlated events related to flerovium decay chains, are presented in Paper V. For further information on this well-established method, the reader is referred to e.g. Chapter. 6.6 of Ref. [2]. In addition, all fission events as well as promising α decays (without requiring preceding implantation events) during beam-off periods were investigated in more detail by looking forward or backward in time for pixel-correlated recoil signals and decay signals possibly resembling Fl-decay chains. The outcome of this analysis were 32 candidate Fl-decay chains.

Events connecting the EVR implantation event and the fission within an implantation-detector pixel were tracked along all the candidate Fl-decay chains. The data, i.e., pulse shapes, hits in the DSSDs and Ge-detectors, and general event information, for all events along a decay chain, was compiled into pdf documents. Six of the chains were missing EVR implantation events. For these chains a reasonable time window was opened to also view potential EVR implantation candidate events. An example of an event from these documents is presented in Appendix E.

The detailed information following all events comprised in these documents were scrutinized. The constituents of the Fl-decay chains were determined, namely whether an event corresponded to an EVR implantation, an α decay or spontaneous fission, or if it was missing. For the decay chains which triggered the beam shut-off routine and those starting at ^{286,288}Fl, this was often straight forward. However, for the ^{289}Fl-decay chains with long correlation times, several intruder events occurred in the tracked implantation-DSSD pixel.

During beam-on periods the intruder events comprised for instance $\sim 5\,\mathrm{MeV}$ punch-through events of light ions and $\sim 70\,\mathrm{MeV}$ implantation signals of non-fusion reaction products. α, and mainly β radiation, stemming from decays of implanted nuclei dominated periods outside the beam pulse. The α decays could often be associated with known emission energies of radioactive nuclei in the region near $A \sim 220$ and ~ 240. In contrast, the β decays, typically manifested in events for which low-energy signals in the implantation detector were observed in prompt coincidence with low-energy signals in the box or veto DSSDs. Proving the usefulness of the veto DSSD, these events could be discriminated from so-called *escape-α* candidate events, otherwise not possible. In escape-α events, the emitted α particle of an implanted nucleus deposits only part of its energy in the implantation DSSD, while not entering any of the four upstream box DSSDs, comprising $\sim 20\,\%$ of the cases. Such events were further investigated with GEANT4 simulations in which their minimum energy deposition, for instance, could be determined.

A thorough analysis of event rates form the main part of Paper V. Here the characterisation of escape-α candidate events together with reconstructed events aided by GEANT4 simulations (see also Sec. 5.3) is a key ingredient. Furthermore, the analysis of trigger rates, introduced in Chapter 4.1, forms the basis to explain missed implantation and α-decay events along the Fl-decay chains as well as randomly correlated hits in the germanium detectors. As a final aid in the interpretation, the expected number of random chains due to fluctuations in the background of the same character as the candidate Fl-decay chains with its constituents, were determined using measured rates of different event types per pixel in the implantation DSSD.

5.3 Geant4 simulations

GEANT4 simulations of TASISpec [30] have been performed before, and Chapter 5.1-2 in Ref. [72] introduces them well. The experimental setup was adjusted to accommodate the current TASISpec+. The four Compex detectors were added along with the veto DSSD. Accompanying this change, the position of the implantation DSSD along the beam-direction with respect to the box DSSDs had to be adjusted. The pixel-by-pixel deadlayer thicknesses for all DSSDs, which had been estimated for the current experiment, were updated. The primary particle, i.e., the radioactive nucleus, was placed according to the measured fusion-evaporation implantation 2D profile [2] inside the implantation DSSD at a certain implantation depth, which is discussed further in Sec. 5.4.

To reproduce experimental conditions as close as possible, further measures were included mainly to the GEANT4 unpacking step of the Go4 analysis, see Fig. 5.1. Within a time window of $0.2\,\mu$s, energy depositions in all detector volumes were accumulated in the GEANT4 simulations. This corresponds to the minimum time difference the pile-up routine is able to identify separate pulses. In GEANT4, one event comprises all the energy depositions induced by the primary particle. As part of the GEANT4 Go4 step, all hits within the sensitive time window for the recorded DSSD traces, i.e., $70\,\mu$s, were sorted into one event. Correspondingly, a $7\,\mu$s time window, with respect to the first hit

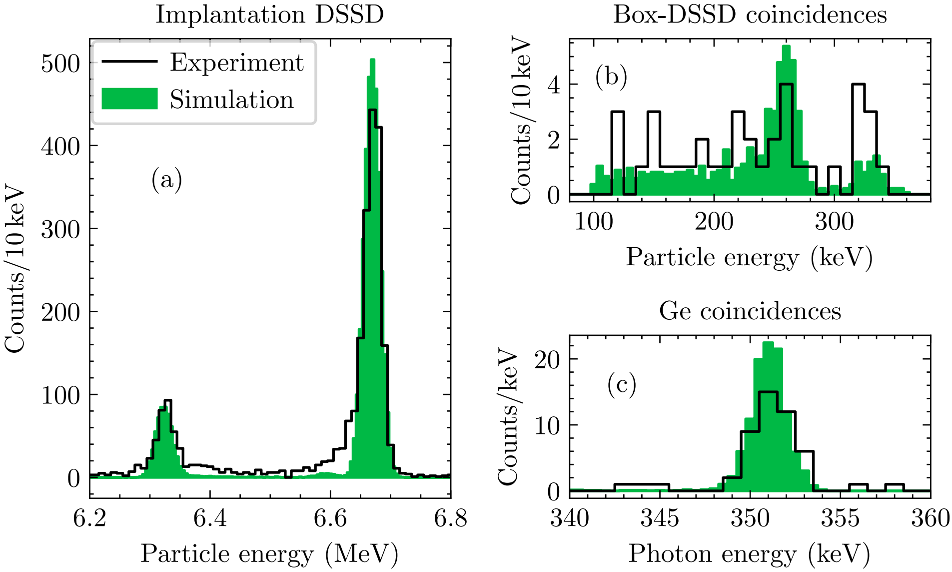

Figure 5.5: Experiment and GEANT4 simulated particle implantation DSSD (a), box-DSSD coincidence (b) and photon coincidence (c) spectra for the ^{211}Bi decay. Energy ranges of most relevance are shown.

in the event, was implemented for the germanium detector channels. Using the detector identifiers provided by the GEANT4 data, DSSD pixel hits were transformed into hits in strips, and germanium crystal hits were converted into channel hits, thus shaping the GEANT4 data into experimental form. All hits below the experimental thresholds were removed. Furthermore, the measured energy resolution for all detectors as introduced in Sec. 5.1 was implemented to reproduce peak widths. For the simulated DSSD, it is always the full energy registered, e.g. Q_α, and using the recoil fraction (see Sec. III. E of Paper V) experimental energies were obtained or experimental energies were transformed into E_α. Except for the calibration and alignment procedures, as part of the Go4 analysis step, the prepared GEANT4 data was processed identically to the experimental data.

Before confronting the scarce experimental spectra derived from the observed Fl-decay chains, the virtual GEANT4 experiments were cross-checked to experimental cases. The α decay of ^{211}Bi produced prominent peaks in the experimental spectrum. Its decay characteristics, as established by the end of the 1960s [75], has two main branches, $E_\alpha = 6.62$ and 6.28 MeV, entering the ground state and an excited state at 351 keV in ^{207}Tl, respectively. The excited state connects to the ground state via a mixed $M1(E2)$ 351 keV γ-ray transitions with a total internal conversion coefficient of 0.243 [40]. Since ^{211}Bi is primarily created through the ^{219}Fr-^{215}At α-decay chain it was possible to efficiently separate out its decays and obtain rather clean spectra by means of a correlation search. All of these aspects combined made ^{211}Bi an ideal spectroscopic test case to verify the simulation input parameters.

Figure 5.5 shows the comparison between the experimental and simulated data for the ^{211}Bi decay. Due to the lifetime of ^{215}At ($t_{1/2} \sim 100\,\mu s$) being close to the data acquisition dead time (in the range $\sim [70, 190]\,\mu s$ with respect to the first ^{219}Fr decay), its decay was not required in the correlation search. The simulated spectra were normalised based on the measured intensity of the 6.62 MeV peak. Peak shapes in the α-decay spectrum correspond well to those experimentally observed, particularly relevant for the 6.28 MeV peak comprising α-electron summing events. The 260 keV and 335 keV conversion electron peaks for the K and L shells, respectively, are well reproduced in the coincident box-DSSD spectrum. Due to an overestimated photon detection efficiency in the simulation, it was attenuated such that it matched original TASISpec. As can be seen, despite this attenuation, the intensity in the 351 keV does not match very well. However, further test cases, namely the decay of ^{219}Rn as well as ^{253}No, showed consistent yields.

Observed α-electron coincidences in the experiment laid the foundation for important nuclear structure interpretations. It was therefore desirable to better understand the electrons measured in the box DSSDs, cf. Fig. 5.5(b). In further simulations, electrons with kinetic energies 200, 400 and 600 keV were emitted from the 5.0(6) µm within the implantation DSSD (see Sec. 5.4). First of all, due to multiple scattering, emitted electrons may deposit parts of their energy in several DSSDs. This could be established by inspecting GEANT4 tracking information. This process provides an explanation to the low-energy tails of the electron peaks, and it will affect full-energy electron peak efficiencies. The proportion of counts in the full-energy peak with respect to the full spectrum yield above the 100 keV threshold in the box DSSDs was determined. Values around 65%, 50% and 45% were obtained for the different kinetic energies, in ascending order. Furthermore, the total full-energy peak efficiencies in the box DSSDs (implantation DSSD) were roughly 25% (35%), 25% (20%) and 20% (5%) at the 200, 400, and 600 keV, respectively.

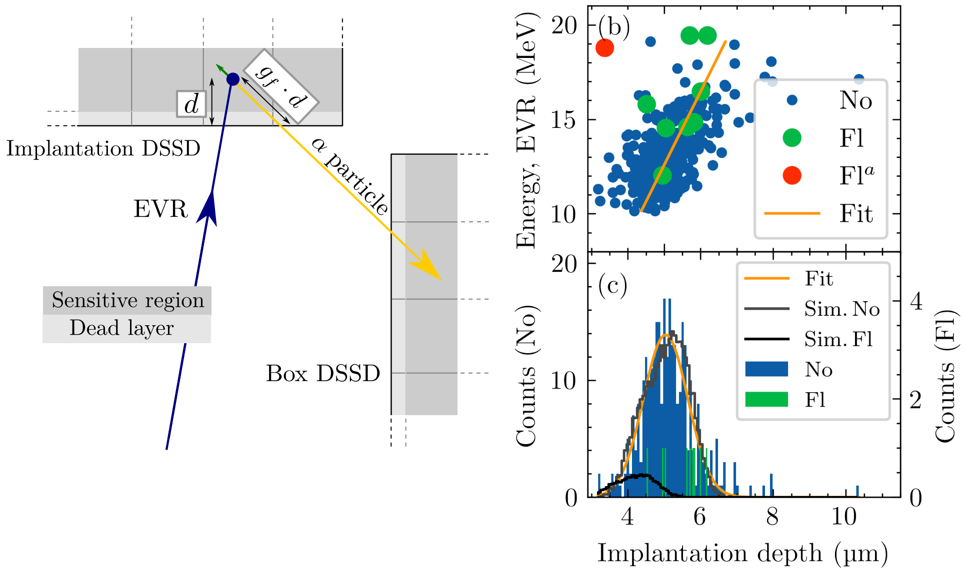

Figure 5.6: (a) Schematic of a reconstructed α-decay event in a two-dimensional representation. (b) Implantation depth as deduced from reconstructed α decays as a function of measured energy of the recoil as it was implanted for ^{252}No and Fl-decay chains. A linear fit based on the ^{252}No data is also shown. (c) X-axis projection of (b), i.e., distribution of implantation depths for ^{252}No and Fl-decay chains. Note that the Fl-decay chains missing an EVR have also been included. A 5.0(6) µm Gaussian fit to the ^{252}No distribution is included as well as simulated distributions for ^{252}No and ^{289}Fl (see text for details).

---

[a] EVR implantation candidate event in chain 30 which was disregarded.

5.4 Implantation depth

Following the fusion-evaporation reaction, the EVR recoils out of the target with kinetic energy of typically $\sim$ 40 MeV and is implanted into the implantation DSSD. The implantation depth plays a decisive role for the energy deposited in the DSSDs by particles emitted following radioactive decays and for the outcome of the Geant4 simulations [76]. This is particularly so for the case of escaping α particles, and primarily to determine a threshold for their energy depositions. As an example, 10-MeV α particles traversing 1 µm of the silicon material lose roughly 100 keV. Means to provide a more detailed input to the simulations were therefore investigated.

In about 30% of α decays of implanted nuclei in TASISpec [33], parts of their energy is deposited in the implantation detector and the remaining in one of the box DSSDs positioned upstream. A schematic two-dimensional representation of such an event is illustrated in Fig. 5.6(a). The full α energy can be *reconstructed* by correcting for energy losses in dead layers, present both when leaving the implantation DSSD pixel and when entering the box DSSD pixel. In the reconstruction routine, so-called geometrical factors, g_f, accommodate the angle-dependent additional track length (compared to emission in the upstream direction) the α particle needs to travel between the pixel in the implantation DSSD and the pixel in the box DSSD. In cases where the initial energy of the α particle is known, and the energy deposited in the implantation DSSD before escaping into the box DSSD is measured, it is possible to determine the implantation depth. Using α-particle stopping powers in SiO_2 in a python framework built from *pysrim*[1] (based on SRIM [70]), and the measured energy deposition in the implantation DSSD before escaping into the box DSSD (subtracted by the assumed detected energy of the recoiling nucleus [Sec. III. E., Paper V]), the track length in the sensitive region of the implantation detector could be determined and consequently the implantation depth, d, following the summing with the pixel dead layer thicknesses.

This routine was explored on the ^{252}No $E_\alpha = 8.40\,\mathrm{MeV}$ decays produced in the ^{206}Pb(^{48}Ca,2n)^{252}No fusion-evaporation reaction, extracted based on the correlation search outlined in Sec. 2, Paper III. Figures 5.6(b-c) present the results deduced from the analysis, including events available from the Fl-decay chains and their correlations to the measured EVR energy following their implantation. As expected, there is a clear trend between the implantation depth and the EVR energy. However, the width of the implantation depth distribution in Fig. 5.6(c), 5.0(6) µm, is first and foremost dominated by other effects. This can be further exemplified by the implantation depths determined based on two reconstructed events which are part of the same Fl-decay chain (No. 17). These are 5.7 µm and 6.2 µm for the first and second α decay, respectively. This difference cannot be explained solely by the recoil of the α-decaying nucleus at some 200 keV, which at most can contribute to 0.05 µm. As the α particles escape to different box DSSDs in the above example, impaired geometrical factors caused by inaccurate geometrical assumptions provide a reasonable explanation for the observed deviation and width of the implantation depth distribution.

The implantation depth provides yet another mean to interrogate the candidate Fl-decay chains. For instance, an implantation candidate event in chain 30 could be disregarded based on such arguments. Note that the implantation depths derived for the disregarded chains are marked Fl^a in Fig. 5.6(b). The recoil energy for the candidate implantation event was 18.8 MeV, while the obtained implan-

---

[1] `https://gitlab.com/costrouc/pysrim`

tation depth was merely 3.5 µm. This would yield a point strongly deviating from the observed correlations shown in Fig. 5.6(b). Therefore, the event was deemed unlikely to stem from an EVR of a fusion-evaporation reaction.

It is of relevance to compare the obtained implantation depths to those predicted by calculations based on the kinematics and stopping powers of the nuclei being implanted. In order to handle ions and targets with $Z \geq 92$, the effective charge [77, 78] and the general Bethe-Bloch relationship, respectively, were utilised to extrapolate the stopping-power functions [70]. Combined with detailed information on thicknesses of degrader foils, target backing foils, and target layers given in Table 1 in Paper V, together with masses of compound nuclei [79, 80], average kinetic energies after the target were derived. Neutron evaporation of the compound nucleus was assumed isotropic and energy losses in TASCA were assumed negligible. Obtained post-target average kinetic energies of 37(3) MeV and 35(3) MeV resulted in implantation depths of 5.6(4) µm and 4.8(4) µm for ^{252}No and ^{289}Fl, respectively. Here, the average is derived from assumed compound nucleus formation at the center of the target layer while the given uncertainties represent the corresponding values at the target edge-points. For ^{252}No, this value is larger than the experimentally measured 5.0(6) µm obtained above.

The transmission mode of TASCA imposes an angle of incidence of the implanted EVR, as can be seen in Fig. 4.4 of Ref. [2]. The implantation depth distribution was therefore simulated. The angular spread was assumed negligible along the horizontal direction, while following the uniform distribution $\mathrm{unif}(-\pi/2, \pi/2)$ vertically. EVRs of ^{252}No and ^{289}Fl with kinetic energies following the $N(37, 3)$ and $N(35, 3)$ MeV normal distributions were implanted, respectively. The resulting simulated distributions, included in Fig. 5.6(c), reproduced the experimental distribution well in the ^{252}No case. However, there was a considerable discrepancy between the simulated and experimental data for the Fl-decay chains. The 5.0(6) µm distribution agreed better, and therefore it was finally used in the Geant4 simulations.

Chapter 6

Results

And why $Z = 114$ is unlikely to be the next magic number

The spectroscopy experiment led to the observation of a total of 29 flerovium-decay chains. Twelve of these were associated with the decay of ^{288}Fl, two with ^{286}Fl, and up to 15 with the decay of ^{289}Fl. The current chapter describes three highlights from the experimental results, one from each flerovium isotope:

- ^{288}Fl: Discovery of the ^{280}Ds isotope as a consequence of the α-decay branch of ^{284}Cn in Sec. 6.1.
- ^{286}Fl: Discovery of an excited state in ^{282}Cn in Sec. 6.2.
- ^{289}Fl: Presence of fine structure in ^{289}Fl α-decay chains in Sec. 6.3.

The main nuclear structure results of the even-even ^{286,288}Fl chains are presented in Paper IV. The odd-A ^{289}Fl results are subject of a forthcoming publication drafted as Paper VI. Tables II and III in Paper V present the comprehensive spectroscopic information of the ^{286,288}Fl and ^{289}Fl decay chains, respectively, including the background information on the analysis and statistical assessments.

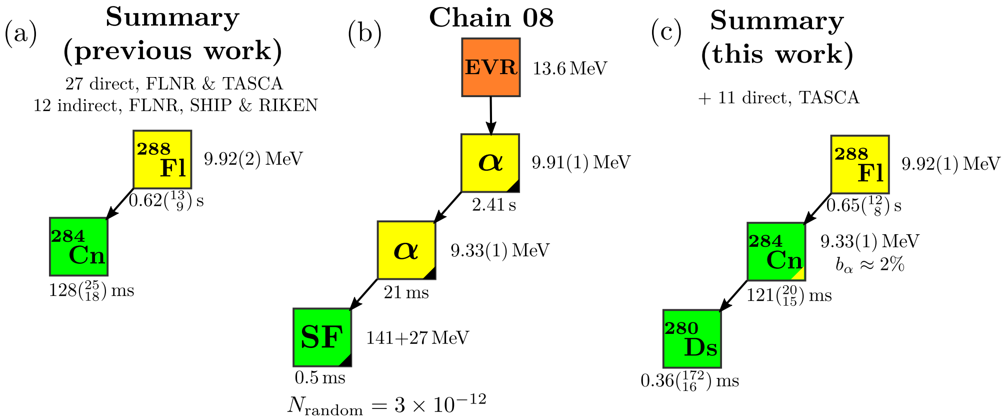

Figure 6.1: (a) Summary of decay energies and half-lives associated with ^{288}Fl-decay chains, compiled from direct and indirect production of previous work at indicated laboratories and separators. (b) Measured energy (with systematical uncertainty in the case of α decays) as well as time differences between events associated with chain 08. Events with a black triangle at the lower right corner of the box, occurred during beam-off periods. The expected number of random chains, N_{random}, for this type of chain is given at the bottom. (c) Same as (a), but including eleven energy ^{288}Fl-decay chains of this work. Data taken from Table 2 in Paper IV and its Supplemental Material.

Figure 6.2: ^{288}Fl α-decay spectra compiled from previous work (a), this work (b), and all combined (c). For a single entry, a Gaussian with integral one and a width compliant with its measured uncertainty was added into the respective spectrum. The numbers at the right of each panel are the (α-decay) energies extracted by computing the histogram mean in the interval [9.5, 10.3] MeV. The number of available data points for each spectrum is given behind the hashtag, #. Adapted from Fig. 2 in the Supplemental Material of Paper IV.

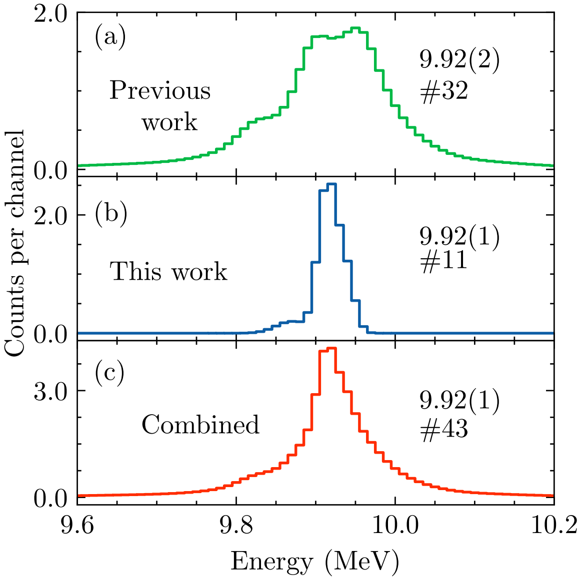

6.1 ^{288}Fl

Historically, ^{288}Fl was observed to α decay with an average $E_\alpha = 9.92(2)$ MeV as shown in Fig. 6.1(a). However, compiling all data points of previous experiments into a decay spectrum seemed to hint at the existence of α-decay fine structure. This spectrum is presented in Fig. 6.2(a). There appears to be two overlapping peaks ($\Delta E \approx 0.1$ MeV) of similar strengths. This odd observation triggered discussions [7], but from the nuclear structure of even-even nuclei, it was difficult to explain. The relatively large amount of data points from the present work yielded one distinct peak of the ^{288}Fl α-decay spectrum, as can be seen in Fig. 6.2(b). Thus, this work's high spectroscopic quality (cf. Fig. 5.3) in combination with the relatively large amount of data points allowed to resolve the puzzling observations. It further demonstrates the importance of spectroscopic performance for nuclear structure interpretations, as emphasized in Chapter 5.

Figure 6.1(b) presents the events associated with chain 08. The chain started with a recoil implantation of 13.6 MeV. It was followed by an α-decay event with $E_\alpha = 9.91(1)$ MeV, after 2.408 s during a beam-off period. This event triggered the beam shut-off routine. After 21 ms, another α-decay event occurred, now with $E_\alpha = 9.33(1)$ MeV. Finally, 0.5 ms later, the decay chain terminated with a fission event, in which 141 MeV and 27 MeV were deposited in the implantation and a box DSSD, respectively. The number of random chains of this kind expected due to fluctuations in the background in our experiment was as low as 3×10^{-12}. Comparing Fig. 6.1(a) and (b), the first α-decay energy and both first correlation times are consistent with those of ^{288}Fl and ^{284}Cn from previous work. We therefore concluded to have for the first time observed an α-decay branch of ^{284}Cn with a branching ratio $b_\alpha = 1/51 \approx 2\,\%$ and $Q_\alpha = 9.46(1)$ MeV. This also meant that the isotope ^{280}Ds, which decayed by spontaneous fission with a half-life of $0.36(^{172}_{16})$ ms, had been firmly discovered. The updated decay characteristics of ^{288}Fl following this work, are presented in Fig. 6.1(c).

In previous experiments, $Q_\alpha = 10.79(4)$ MeV for the decay of ^{292}Lv (element 116) was determined [16, 81, 82]. With the newly discovered α-decay branch of ^{284}Cn, this meant that for the first time a high-resolution Q_α sequence across the anticipated $Z = 114$ proton magic number could be established. It could be noted that, previous experiments on even-odd as well as odd-odd decay chains starting from ^{293}Lv [16] and ^{288}Mc [17] do cross $Z = 114$. However, due to α-decay fine structure problematics, as described in Chapter 2, Q_α deduced from these experiments are associated with a larger degree of uncertainty. The newly established Q_α sequence is shown in Fig. 6.3(b). A smooth trend can be observed with the experimental data points. $^{288}_{114}$Fl$_{174}$ is about ten neutrons short of the

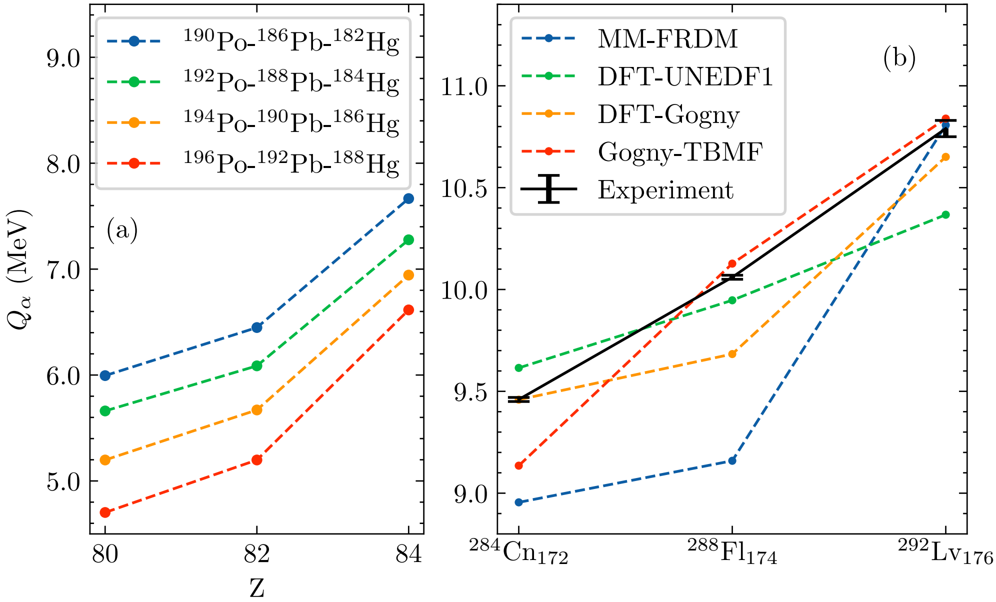

Figure 6.3: (a) Several Q_α sequences across the magic number $Z = 82$, about twenty neutrons away from doubly magic $^{208}_{82}$Pb$_{126}$. (b) Comparison of experimental and theoretically predicted Q_α values for the α-decay sequence ^{292}Lv→^{288}Fl →^{284}Cn. The theoretical numbers are from one macroscopic-microscopic model, MM-FRDM [83], two axially symmetric density functional theory calculations, DFT-UNEDF1 [84] and DFT-Gogny [85], and one triaxial beyond-mean-field calculation, Gogny-TBMF [86].

anticipated doubly-magic $^{288}_{114}$Fl$_{184}$. As such, what can these results tell about the strength of a shell gap at $Z = 114$? Figure 6.3(a) shows Q_α decay sequences across the proton magic number $Z = 82$ for neutron deficient Po-Pb-Hg decay chains about 20 neutrons away from the neutron magic number $N = 126$. It is clear, that a *kink* in the Q_α sequence is characteristic for a pronounced shell gap. Hence, there seems to hardly be any shell gap at $Z = 114$ and it is unlikely to be the next proton magic number.

Figure 6.3(b) also compares the experimental Q_α trend with theoretical predictions from a selection of models. The MM-FRDM [83] model displays a clear kink and it predicts a shell gap at $Z = 114$. In contrast, the axial-symmetric DFT-Gogny [85] does not predict a shell gap at $Z = 114$, but still predicts a kink. The DFT-UNEDF1 [84] model, which prefers $Z = 120$ as the next proton magic number, predicts a smooth trend, but is deviating in slope and absolute values. The last prediction included are beyond-mean-field model calculations, which include triaxial shapes, denoted Gogny-TBMF [86]. The Gogny-TBMF values agree well in the case of ^{292}Lv and ^{288}Fl, while it shows a bigger deviation for ^{284}Cn. These contemporary calculations are demanding and it actually takes about two weeks (similar to the experiment) for each data point to be computed. One important outcome of the study in Ref. [86], was that several even-even Fl ground states assume triaxial shapes. It demonstrates the need to account for these shape degrees of freedom in future predictions of superheavy nuclei. In conclusion, the experimental trend now provides a stringent test on theoretical predictions.

6.2 ^{286}Fl

Chain 02, as shown in Fig. 6.4(b), began with a recoil implantation of 13.6 MeV. It was followed by an α-decay event of 9.60(1) MeV 52.6 ms later during a beam-off period. The α event triggered the beam shut-off routine. A fission event, deposited 239 MeV in the implantation DSSD, concluding the chain after an-

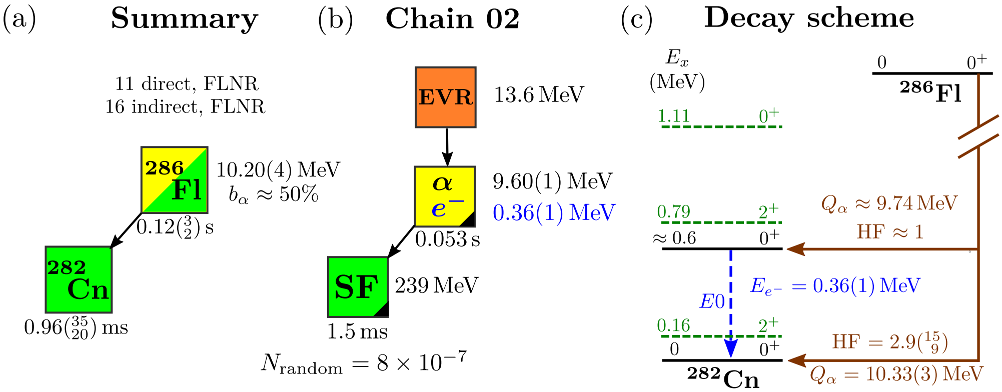

Figure 6.4: (a) Summary of decay energies and half-lives associated with ^{286}Fl-decay chains, compiled from direct and indirect production of previous work at indicated laboratories and separators. (b) Events associated with chain 02. Measured energies as well as time differences between events are given. The 0.36(1)-MeV electron (blue) was measured in a box DSSD in prompt coincidence with the 9.60(1)-MeV α event in the implantation DSSD. α and electron energies are given with a systematical uncertainty. Events with a black triangle at the lower right corner of the box, occurred during beam-off periods. The expected number of random chains, N_{random}, for this type of chain is given at the bottom. For (a) and (b), data was taken from Table 2 in Paper IV and its Supplemental Material. (c) Suggested decay scheme of ^{286}Fl. The excited state at ≈ 0.6 MeV has been deduced from chain 02 and has a proposed tentative spin-parity assignment, as well as depopulating electromagnetic transition. Predicted [86] excitation energies, E_x, are shown in green. See text for details.

other 1.48 ms. The number of expected random chains with these decay characteristics was determined to $N_{\text{random}} = 8 \times 10^{-7}$. Previously measured average decay characteristics of ^{286}Fl-decay chains are presented in Fig. 6.4(a). Both correlation times, i.e. the recoil-α and α-SF, agree well with the half lives of the ^{286}Fl reference decay chain. However, the 9.60(1) MeV α energy is ≈ 0.6 MeV below the average value, $E_\alpha = 10.20(4)$ MeV.

The detection of a 0.36(1) MeV signal in a pixel of one of the box DSSDs in prompt coincidence, $\Delta t < 50$ ns, with the 9.60(1)-MeV event in the implantation DSSD makes this decay chain unique. Through further analyses described in Paper V, it was concluded that the only explanation for the observed event was an α-(conversion) electron coincidence. Electron binding energies for the K and L shells in Cn are $B_{e,\text{K}}(\text{Cn}) \approx 190$ keV and $B_{e,\text{L}}(\text{Cn}) \approx 40$ keV, respectively [37]. The energy released in the decay, $[9.60(1) + 0.36(1)] + B_{e,\text{K,L}}(\text{Cn}) \approx 10.15$ MeV for K conversion and ≈ 10.00 MeV for L conversion, matches that of ^{286}Fl rather well. In conjunction with the very short correlation times compared to other Fl-decay chains, an explanation for this observation is an $E_\alpha \approx 9.6$ MeV branch with $b_\alpha = 1/29 \approx 3\,\%$, which connects the 0^+ ground state of ^{286}Fl with an excited state in ^{282}Cn. Based on Q_α values of ≈ 9.74 MeV and 10.33(2) MeV for the decay branches, the energy of the excited state becomes ≈ 0.6 MeV (cf. Table 2 in Paper IV). In this scenario, the 0.36(1) MeV electron stems from a converted electromagnetic transition. Ultimately, the event marked the first observation of an excited state in a superheavy even-even nucleus beyond $Z = 108$. It also demonstrates the advantages of using low-energy thresholds for the box DSSDs.

Figure 6.4(c) depicts a suggested decay scheme for the ^{286}Fl decay going through the ≈ 0.6 MeV excited state in ^{282}Cn. A hindrance factor of HF ≈ 1 [87] was determined for the $Q_\alpha = 9.74$ MeV decay branch. This indicates that the involved states in the α decay have similar structural properties and that the angular momentum carried by the α particle is most likely zero, $\ell_\alpha = 0$. It is therefore reasonable to make a 0^+ spin-parity assignment of the excited state. Since many theoretical models predict the first 2^+ state significantly below 600 keV (see Paper IV and references therein), an $E2$ cascade down to the ground state would be the intuitive conclusion. Such a decay scenario was put forward in Paper IV. In Paper V, additional possible decay scenarios of the excited state were investigated in more detail by means of GEANT4 simulations and transition strengths predicted by the Gogny-TBMF model. It turned out that the very high monopole transition, $E0$, probability for superheavy nuclei [37] combined with its purely converted character rendered such a transition the most likely reproducing the measured 360 keV signal in the box DSSD. The results, reinforced the $I^\pi = 0^+$ assignment of the excited state.

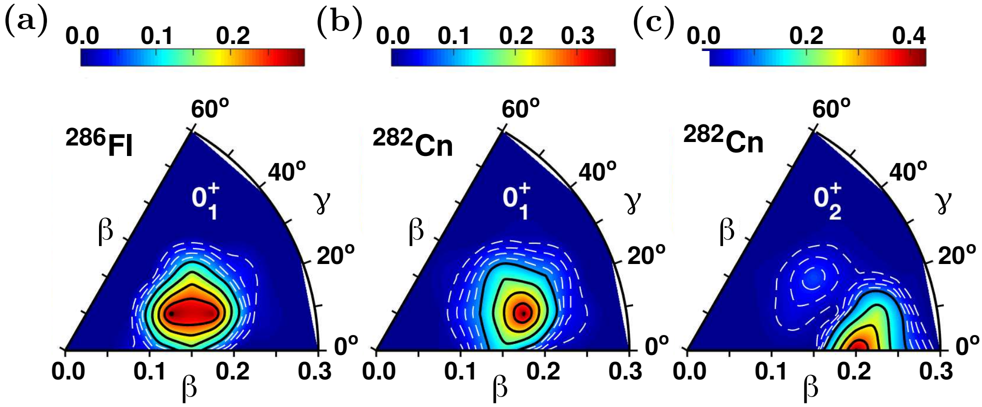

Figure 6.5: (a)-(c) Predicted [86] squared collective wave functions of the 0_1^+ ground states of ^{286}Fl and ^{282}Cn and the excited 0_2^+ state in ^{282}Cn. The color code differs slightly for the different panels. The dashed white contours display probability densities of 0.02, 0.04, 0.06, and 0.08, while the solid black lines uniformly cover the range between 0.10 and the maximum value. Figure with courtesy of J.L. Egido.

Excitation energies in ^{282}Cn, predicted with the contemporary Gogny-TBMF calculations mentioned earlier [86], are included in Fig. 6.4(c). These calculations are novel in the sense that they take into account configuration mixing as well as triaxial shapes which have been shown to be important in order to make reliable predictions of nuclei in the superheavy regime [86]. Indeed a low-lying 0^+ state at $E_x = 1.11\,\text{MeV}$ is predicted. Figure 6.5 shows squared wave functions in the (β, γ) plane for the involved states in the ^{286}Fl-decay predicted with the Gogny-TBMF. As can be seen, triaxial shapes are predicted for the 0_1^+ ground states in ^{286}Fl and ^{282}Cn, while the excited 0_2^+ assumes a prolate shape. The situation is somewhat similar to what have been observed for excited 0^+ states in neutron deficient even-even nuclei around ^{186}Pb. Remarkably in ^{186}Pb, a spherical 0^+ ground state coexists with both a prolate 0^+ and an oblate 0^+ excited state within ≈ 600 keV [88]. These states find their explanation in multi-quasiparticle excitations in which the nucleus gains significant binding energy through deformation. For the doubly-magic $^{208}_{82}$Pb$_{126}$ such an excitation requires ≈ 5 MeV [75]. However, the excitation energies of the 0^+ states decrease to reach a minimum for nuclei with neutron numbers in the middle between the closed neutron shells, $N = 82$ and $N = 126$ [89]. Since $^{282}_{114}$Cn$_{168}$ is anticipated to be located rather close to the next spherical magic numbers, as such, the low-lying 0_2^+ state in ^{282}Cn corroborates the absence of a pronounced shell gap at $Z = 114$.

6.3 ^{289}Fl

The average decay characteristics of ^{289}Fl chains from previous experiments are compared to two of the fifteen directly produced ^{289}Fl-decay chains from this work in Fig. 6.6. Closing in on the center of the Island of Stability, half-lives of nuclei are expected to increase. As shown in Fig. 6.6(a), the half-lives along the most neutron rich Fl-decay chains, i.e., those starting from ^{289}Fl, are ≈ 2 s, ≈ 30 s and ≈ 13 s for the first three decay steps, respectively. The implantation and decay sequence of chain 28 in Fig. 6.6(c) illustrates the experimental conditions well. It started with a 14.0-MeV recoil implantation and was followed by a beam-off α-decay event, $E_{\alpha_1} = 9.79(1)$ MeV, after 1.30 s which triggered the beam shut-off routine. More than four minutes later, $\Delta t = 252$ s, another full-energy α_2 event combined with a spontaneous-fission event short thereafter ($\Delta t = 1.36$ ms) concluded the chain. Owing to the 300-s long beam shut-off period, the last three events were measured in a very low background environment in which the 0.36-MeV signal could be confidently assigned as an escape-α, see Sec. III. B. in Paper V. Furthermore, a small number of expected random chains with these decay characteristics could be determined, $N_{\text{random}} = 2 \times 10^{-8}$.

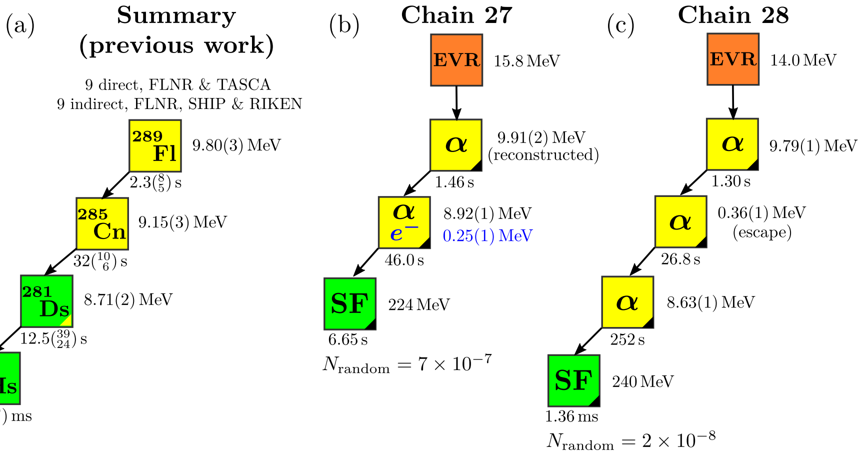

Figure 6.6: (a) Summary of decay energies and half-lives associated with ^{289}Fl-decay chains, compiled from direct and indirect production of previous work at indicated laboratories and separators. Data taken from the Supplemental Material of Paper VI. Measured energy as well as time differences between events associated with chain 27 (b) and chain 28 (c). α and electron energies are given with a systematical uncertainty. Events with a black triangle at the lower right corner of the box, occurred during beam-off periods. The expected number of random chains, N_{random}, for this type of chain is given at the bottom.

The relatively short decay chains with long correlation times, makes the detection of the ^{289}Fl-decay chains challenging to separate out from random decays in the background with the implantation-decay technique. The beam shut-off routine plays a decisive role. However, their successful identification is primarily owed to the low-background environment during the beam-off periods of the UNILAC beam at GSI, which has been noted earlier in Refs. [90, 91]. Finally, this experiment's sensitivity to these types of chains may be demonstrated with the increase in the half-life of ^{285}Cn from 32 s based on previous work to 51 s in the current work, see Table II in the Supplemental Material of Paper VI.

In chain 27, shown in Fig. 6.6(b), the recoil implantation-α_1 correlation triggered the beam shut-off routine, although the 9.91(2) MeV α being reconstructed. Before the chain was concluded with spontaneous fission, an 8.92(1)-MeV α_2 decay of ^{285}Cn was detected in coincidence with a 0.25(1) MeV electron in a box DSSD. Similarly to what was discussed for the ^{286}Fl α-electron coincidence in Sec. 6.2, the 0.25-MeV box-DSSD signal most likely stems from an internal conversion electron. Corroborated by the $E_{\alpha_2} = 8.92\,\mathrm{MeV}$ being $\approx 300\,\mathrm{keV}$ lower in energy compared to the $E_{\alpha_2} = 9.15(3)\,\mathrm{MeV}$ of the main decay branch in Fig. 6.6(a), this event provides strong evidence for the presence of an electromagnetic transition in ^{281}Ds. A measured α(escape)-electron-(K X-ray candidate)-photon coincidence in chain 26 for the ^{285}Cn decay further supports the claim.

Actually, the α energy of the ^{289}Fl decay in chain 27, $E_{\alpha_1} = 9.91(2)$, also deviates from the corresponding $E_{\alpha_1} = 9.80(3)\,\mathrm{MeV}$ of the main branch. In fact, several α-decay energies which strongly deviate from those of the main decay path exist in the data sets of both the current and previous experiments, see Supplemental Material of Paper VI. $E_{\alpha_1} = 9.56(1)\,\mathrm{MeV}$ in chain 22 as well as $E_{\alpha_1} = 9.99(2)\,\mathrm{MeV}$ and $E_{\alpha_2} = 9.30(2)\,\mathrm{MeV}$ from chain 17, are two further examples from the current experiment. These chains are suggested to form separate independent decay paths, connecting isomeric α-decaying states along the ^{289}Fl-decay chains. The current experiment thus provides evidence for the existence of both α-decay fine structure, as well as independent decay paths, for the odd-A Fl-decay chains as predicted by theory and discussed in Chapter 2. Based on the high-quality spectroscopic data of the ^{289}Fl in this work, decay schemes could for the first time be created along the ^{289}Fl-decay chains. In Paper VI, the decay schemes, which were confronted by GEANT4 simulations, are described in more detail.

Finally, for two of the fifteen ^{289}Fl-chains, including chain 28 introduced earlier, α decays of ^{281}Ds were observed. These measurements confirmed the *long* chain ending in ^{277}Hs measured only once before at TASCA [24, 62]. Based on predicted cross sections for the 2n channel, see Table I in Paper V and Fig. 4.5, it is possible that chains starting from ^{290}Fl have already been observed. Being an odd-A isotope, ^{277}Hs has a rather short spontaneous fission half-life of $18(^{25}_{7})$ ms, deduced by including the two measured chains in the current experiment as presented in the Supplemental Material of Paper VI. In Paper V, along with chain 17 briefly introduced earlier, the chains ending in ^{277}Hs were considered to possibly start from ^{290}Fl. Based on theoretical calculations on spontaneous fission half-lives, neither ^{290}Fl options were considered very likely. Furthermore, as decay energies and times of the long chains are fully consistent with starting from ^{289}Fl (see Supplemental Material of Paper VI), it further disfavours this option. Nevertheless, future mass-number measurements in experimental investigations with the BGS-FIONA apparatus [28] may be able to shed some light on this matter.

To conclude, the fifteen new ^{289}Fl-decay chains were able to give valuable insights into all the experimental objectives listed in the beginning of Chapter 4. However, the numerous possible decay sequences as well as potentially missing electromagnetic transitions also call for further nuclear spectroscopy experiments using the ^{48}Ca+^{244}Pu reaction.

Chapter 7

Concluding Remarks

And what is next?

An experiment was conducted behind the TASCA separator at GSI Darmstadt with the aim to perform high-resolution spectroscopy along decay chains of element 114, flerovium. With twelve new chains starting from the even-even ^{288}Fl, a precise Q_α value was derived resolving puzzling observations from previous experiments. For the first time, an α-decay branch was observed for ^{284}Cn, the second decay step of ^{288}Fl. This led to the discovery of the isotope ^{280}Ds, but most intriguing the first high-resolution Q_α sequence across Fl. The Q_α sequence, now completed with a firm data point at ^{284}Cn, was found to provide a stringent test of model predictions. It furthermore showed that there hardly seems to be any shell gap at the next anticipated proton magic number, $Z = 114$.

Two decay chains were associated with the production of ^{286}Fl. One ^{286}Fl α particle was detected with about 0.6 MeV lower energy compared to the main decay branch. The event came in coincidence with an electron and was presumed to be a result of a converted electromagnetic transition in ^{282}Cn. This marked the first observation of an excited state in an even-even nucleus produced in the ^{48}Ca hot-fusion reactions with radioactive and rare actinide targets. The state at ≈ 0.6 MeV in excitation energy was assigned a spin-parity of $I^\pi = 0^+$. The existence of the excited state provides a unique anchor point for nuclear theory.

First, in the presence of shape coexistence, the first excited $I^{\pi} = 0^{+}$ state has a different shape compared to the ground state, and as such presents a rich testing ground for theory. Second, it gives a first insight into collective phenomena at the heaviest extreme of the nuclear chart. Third, because of the lower level density in even-even nuclei, the excited state imposes a stronger constraint on both experimental interpretations and theoretical models.

The main objective of the current experiment was to study ^{289}Fl-decay chains. The measurement of 15 new chains resulted in a doubling of the global data set for this isotope. The successful identification and investigation of their long-lived decays was owed to the unique advantages of the pulsed GSI UNILAC beam combined with the implemented beam shut-off routine. As part of the second ^{285}Cn-decay step another α-electron coincidence was observed, thus revealing the presence of α-decay fine structure and an electromagnetic transition in ^{281}Ds. Combined with energy correlations deviating from the most common branch, elaborate decay schemes could for the first time be created for the ^{289}Fl-decay chains. The decay scheme indicates the presence of independent decay paths as been predicted for the decay chains of odd-A nuclei in this region. Two additional α decays of ^{281}Ds were observed, confirming a suggested decay branch into ^{277}Hs. Being an odd-A isotope, its rather short spontaneous fission half-life stimulated discussions and it is likely to be the subject of future experimental investigations.

Following the results in Paper IV, one referee concluded: "Future technical developments should allow to wring out tantalizing physics from compound nucleus production data where cross-sections are in the picobarn range." Throughout this thesis, the novel Compex germanium detectors saw their successful development. They will form a key ingredient in the future Lundium decay station, the completion of which is underway at the time of writing. A significant increase in sensitivity is foreseen for implantation-decay spectroscopy with Lundium. Its commissioning experiment is scheduled for 2022 at GSI [52]. First superheavy explorations with Lundium may aim to continue investigations on ^{286,287}Fl-decay chains. Measured ^{287}Fl-decay chains this far show the potential for α-photon-electron coincidences and yet unresolved decay paths. More observations of the new decay branch of ^{286}Fl will allow to derive a more precise hindrance factor. Combined with additional photon and electron coincidences, the decay of the $\approx 0.6\,\mathrm{MeV}$ excited state can be further constrained and lead to an increased understanding of the involved nuclear states.

The search for the next proton magic number now aligns with the search for new elements as the next main candidate being the yet undiscovered element 120. Attempts to discover new elements have already been made [65], with experiments at TASCA having employed what is seen as the most promising reactions so far. In month-long irradiations sensitivities of $\approx 100\,\mathrm{fb}$ were reached in reactions with a beam of ^{50}Ti and targets of ^{249}Bk and ^{249}Cf aiming to produce element 119 and 120, respectively [92]. Throughout the last years, efforts have been, and are being made or planned, across the world to further improve experimental capabilites. Perhaps most noteworthy, experiments at the newly constructed “Superheavy Element Factory” in Dubna, Russia, have already taken up the hunt for the prestigious discovery of new elements [93]. In Germany, the development of a continuous wave linear accelerator for use in heavy-element research is foreseen within the nearest future at GSI [94], and first experiments behind the separator-spectrometer setup, S^3, within the SPIRAL2 project of Ganil, France, will be running by 2025 [22, 95].

At the heaviest extreme of the nuclear chart, open questions and challenges remain. For instance, only in the last couple of years, contemporary theoretical calculations have predicted a “super-assymetric fission” [96] or cluster decay [97]. In this process, which is predicted to be present for nuclei in the region around ^{284}Cn, the heavy decay residue is found close to ^{208}Pb. Electron-capture decays have been a hot topic in the field for some time [65, 98]. Recent experiments behind the separator SHIP at GSI, demonstrated the feasibility to detect electron-capture decays in the heavy-element region [99, 100]. The detection principle relies on the measurement of delayed coincidences between characteristic X rays or internal conversion electrons (possible when excited states are populated) following the electron-capture, with subsequent α particles or spontaneous fission events. It is essential, the detection setup sit in a very low-background environment. Lundium installed behind SHIP and equipped with a dedicated triggering system, presents a great way to continue these investigations. The novel adsorption-based nuclear spectroscopy with the set-up ANSWERS is another option [101]. Though this technique lacks the signal from the implantation event, it is suitable for low-background, and efficient decay spectroscopy measurements of longer-lived nuclei while also being perfectly capable to identify the above-mentioned cluster decay. Finally, the (p, xn) and (α, xn) fusion-evaporation channels have been of recent attention, both theoretically [102] and experimentally [103, 104]. Similar to electron-capture decays, they provide the attractive possibility to produce more neutron rich nuclei. They present alternative routes to reach isotopes closer to the Island of Stability while also enabling to fill the uncharted territory on the nuclear chart between nuclei produced in the cold and hot fusion-evaporation reactions.

The experimental results of the present work underline the benchmarking capability of nuclear spectroscopy experiments in the superheavy element regime.

Notably, the two highlights on the even-even ^{286,288}Fl-decay chains were unexpected. They are a good example that we have so far only started exploring this part of the nuclear landscape. As such, I look forward to exciting results following the recent technical developments in near-future experimental endeavours as we close in on the long-sought Island of Stability.

Appendix A

Using the Lund Scanning System

This appendix is directed to users of the Lund Scanning System. Details on the collimator and the (x, y)-positioning system, shown in Fig. A.1(a), are presented. Manufacturing and component details and properties are also provided. Information on how the scanning system is operated concludes the appendix.

The tungsten collimator[1], constituting a source holder, a collimating piece and a lock, has a total height of 160 mm and a diameter of 100 mm. The source is mounted such that the γ rays are collimated through a 1-mm diameter and 100-mm long hole. In order to speed up the scanning measurements, the γ-ray source needs to be very active. During and after its installation, a 1.2 GBq strong ^{137}Cs source calls for radiation safety precautions. A Geant4 simulation of the collimator was performed and a count rate of roughly 120 Bq/cm^2 outside the collimator was obtained. This roughly corresponds to 20 kBq around the collimator, which compares well with a standard calibration source. Once installed it was concluded safe to work around the collimator. However, care for an increased activity at the height of the source should be taken.

A vertically elevated plate of steel[1] with a hole of $120 \times 120\,\mathrm{mm}^2$ was constructed and installed to support the positioning system above the BGO scintillators to relieve these from a large load. The height of this plate was made as small as possible to minimise the distance between the collimator exit hole and the germanium crystal and thus minimise the beam divergence. A tailor-made

---

[1] Manufactured by http://svemek.com/

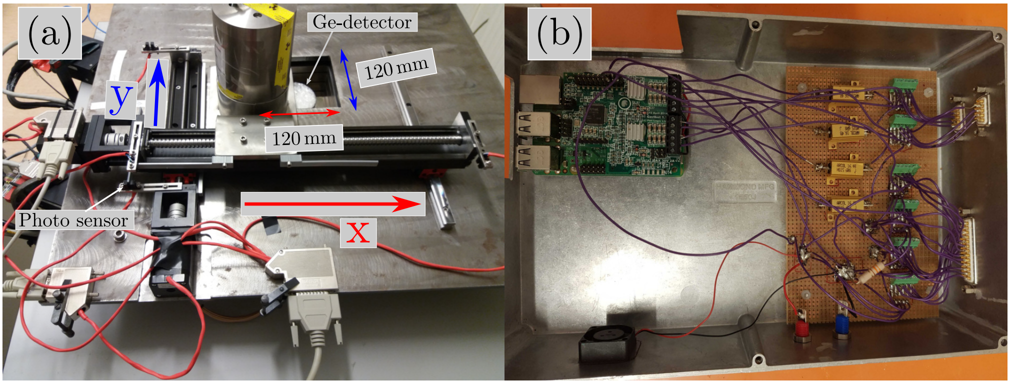

Figure A.1: **(a)** The (x, y)-positioning of the Lund scanning system. Key measurements and components are indicated. **(b)** Raspberry Pi - Gertbot interface.

height-adjustable table[2] sustain the large load from the tungsten horizontal collimators[3] and steel material. The height is manually adjusted with a handle. In the coincidence scan of the Compex detector, the relative height with respect to the germanium detector was monitored by measuring the distance from the end-cap to the elevated steel plate with a caliper.

The two-dimensional movement is accomplished with ball-screw linear units, wagons and guides[4]. One linear unit (`KK5002C-250A1-F3S0`), in the y direction, is placed in parallel to a linear railway (`HGR15RC`). The railwas carries a mounted wagon (`HGW15CCZ0C`). On top of this, another linear unit (`KK6005C-400A1-F5S0`) is mounted perpendicular to the previous units, thus in the x direction, fixed onto the wagons. Onto the top linear unit an extending arm made of stainless steel[5] is installed to hold the collimator.

Two NEMA 17 stepper motors of model `17H261-02S/D`[6] are installed in the motor housings of the linear units. Both stepper motors are controlled via a `Raspberry Pi`[7] `- Gertbot`[8] interface as illustrated in Fig. A.1(b). The output current to the stepper motors is controlled with four 6.7 Ω, 5.5 W resistors. Power to the motors are led through D-Sub 9-pin cables. The power itself is supplied from a `TDK-Lambda Gen 50-30` unit which provides a voltage of 8.5 V

---

[2] Manufactured by `https://gigant.se/`

[3] See footnote 1

[4] Purchased from `https://www.aratron.se/sv/`

[5] See footnote 1

[6] Purchased from `https://compotech.se/`

[7] Raspberry Pi 3 Model B purchased from `https://r-pi.se/`

[8] Purchased from `https://se.rs-online.com/`. For documentation see `https://www.gertbot.com/`

and a large current of ~ 2 A. The power supply is remotely controlled from the `Raspberry PI` via an `RS232` communication protocol. The power is switched on/off at operation.

Four photo sensors of model `OPB990T51Z`[9] act as optical switches. Whenever activated, via cables connected to the Gertbot, power to the stepper motor that activated the end stop is turned off. The purpose of the sensors is to keep the collimator in a predetermined safe region, and perhaps more importantly to reproduce scans accurately. The photo sensors are also powered via the `TDK-Lambda Gen 50-30` unit while the current to the diodes is here limited with a $330\,\Omega$ resistor. Both power and signals are led through a D-Sub 25-pin cable.

The linear units in the x and y directions have lead-values of 2 and 5 mm, respectively, corresponding to the length of one revolution. The stepper motors have a stepping angle of 1.8° and a step accuracy of 0.05°. The photo sensors are very accurate. It is therefore reasonable to assume that a precision of ≤ 0.05 mm (cf. step length of 0.03 mm) should at least be attained for the unit with lead 5 mm.

The detector scans are initiated and controlled from a data acquisition system running off the GSI, C-based, Multi Branch System (MBS)[10]. Within the main `f_user_readout()` function, which is called at every acquired event, data files are closed, the collimator is moved and new files are open, all based on the acquisition duration. By forking the process of `ssh` calls to the `Raspberry Pi` unit and waiting for the process id to finish, the data acquisition is frozen during collimator operations. In turn, the collimator operations are managed from a python-based framework[11] on the `Raspberry Pi`, within which in addition to moving the collimator, (x, y) grids and related logs are generated, and certain communication with the data acquisition is achieved by creating and deleting files via `ssh`.

---

[9] Purchased from https://www.elfa.se/

[10] https://www.gsi.de/en/work/research/experiment_electronics/data_processing/data_acquisition/mbs.htm

[11] Interested coder is referred to https://gitlab.com/ASamarkRoth/MoveCollimator

Appendix B

Absolute Efficiency with the External Trigger Method

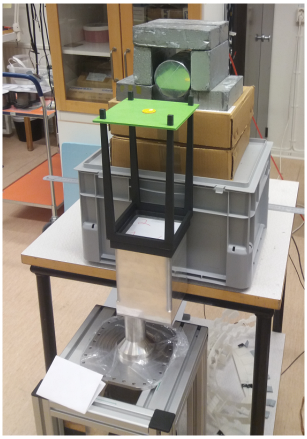

Figure B.1: Setup for efficiency measurements with the external trigger method.

Precise measurements of the full-energy peak efficiency of the Compex detector were performed in Lund with the so-called external trigger method. In this method, the efficiency is determined independently of potentially unreliably calibrated γ-ray sources. The experimental setup depicted in Fig. B.1 was used. A ^{60}Co source was placed on a holder, centred, and at a distance of 25 cm with respect to the Compex end-cap. A standard $7.68 \times 7.68\,\text{cm}^2$ NaI detector, mounted at an angle of 90° with respect to the Compex detector, was used as a reference detector.

In the external trigger method, comparing the yield of coincident 1173- and 1332-keV γ rays to non-coincidences may be used to determine the absolute efficiency of a detector. The intensity of the full-energy peak, I_{fe}, along with the probability to end up in the full-energy peak, P_{fe}, are described as follows:

$$I_{fe} = I_0 \cdot \Omega \cdot \epsilon_{eff} \qquad \propto \qquad P_{fe} = \Omega \cdot \epsilon_{eff}$$

where I_0 is the intensity emitted by the source, ϵ_{eff} is the full-energy peak efficiency, and Ω the solid angle covered by detector with respect to the source.

From the probability to detect the coincident full energy of each γ ray in the germanium and the NaI detectors vs. detecting the 1332 keV peak in the NaI detector, the following can be derived:

$$\begin{aligned} \frac{P_{fe}(Ge|1332 \,\&\, NaI|1173)}{P_{fe}(NaI|1173)} &= \frac{\Omega_{Ge} \cdot \epsilon_{eff}(Ge|1332) \cdot corr_\theta \cdot \Omega_{NaI} \cdot \epsilon_{eff}(NaI|1173)}{\Omega_{NaI} \cdot \epsilon_{eff}(NaI|1173)} \\ &= corr_\theta \cdot \Omega_{Ge} \cdot \epsilon_{eff}(Ge|1332) \end{aligned} \tag{B.1}$$

In practice, the number of coincidences, $I_{fe}(Ge|1332 \,\&\, NaI|1173)$, as well as the intensity of the full-energy peak in the NaI detector, $I_{fe}(NaI|1173)$, is measured, hence:

$$\Omega_{Ge} \cdot \epsilon_{eff}(Ge|1332) = \frac{I_{fe}(Ge|1332 \,\&\, NaI|1173)}{corr_\theta \cdot I_{fe}(NaI|1173)} \tag{B.2}$$

A correction factor, $corr_\theta$, due to the angular correlation between the two ^{60}Co γ rays, has to be taken into account. The probability, per unit solid angle, that two successive γ-rays are emitted at an angle θ is proportional to a function $W(\theta)$. The first emitted γ ray of 1173 keV, determines the quantisation axis and the following 1332 keV γ ray assumes an angular distribution according to [105]:

$$W(\theta) = 1 + \frac{1}{8}\cos^2\theta + \frac{1}{24}\cos^4\theta \tag{B.3}$$

The correction factor for the angular correlation was determined via Monte-Carlo simulations based on the detector setup in Fig. B.1. Random γ rays were generated from an isotropic spherical distribution. In a first simulation, the number of rays incident on the surface of one detector was counted and the solid angle, Ω, covered by the detector was determined. In a second simulation, the azimuthal angle was instead sampled from the distribution in eq. (B.3). $\theta = 0$ was defined by the quantisation axis, i.e. the angle to the other detector. In a simular procedure, a reduced solid angle, Ω', of the same detector could be determined. The correction factor, $corr_\theta$, was finally determined by resampling 100 data sets in a bootstrapping approach, where the estimate was calculated as $corr_\theta = \Omega'/\Omega$. A correction factor of 0.937(10) was obtained.

Appendix C

Beam Shut-off Routine Implementation

This appendix sheds some more light on the details of the beam shut-off routine used in the flerovium spectroscopy experiment.

Figure C.1[1] shows the readout flow of the beam shut-off routine. It is implemented into the `f_user_readout` function on the FEBEX branch of the MBS[2] data acquisition system. The readout flow of FEBEX events is depicted at the bottom left of the figure.

At initialisation, a set of parameters, for example energy gates and time windows, which may be different for periods of beam on versus beam off, are read. It is these parameters that form the condition statements (diamond shapes in the flow chart) of the routine. For reference, an excerpt from the configuration file, wherein these user parameters are set, is presented in C.2.

In a thorough testing framework, based on CATCH2[3], tailored events may be tested to ensure that the logic of the routine works properly. The beam shut-off routine has been integrated into the GO4[4] data analysis. It is from here the parameters of the routine were evaluated and optimised on experimental data.

---

[1] Drawn with **draw.io**: https://drawio-app.com/

[2] https://www.gsi.de/en/work/research/experiment_electronics/data_processing/data_acquisition/mbs.htm

[3] https://github.com/catchorg/Catch2

[4] https://go4.gsi.de

C.1 Flow chart

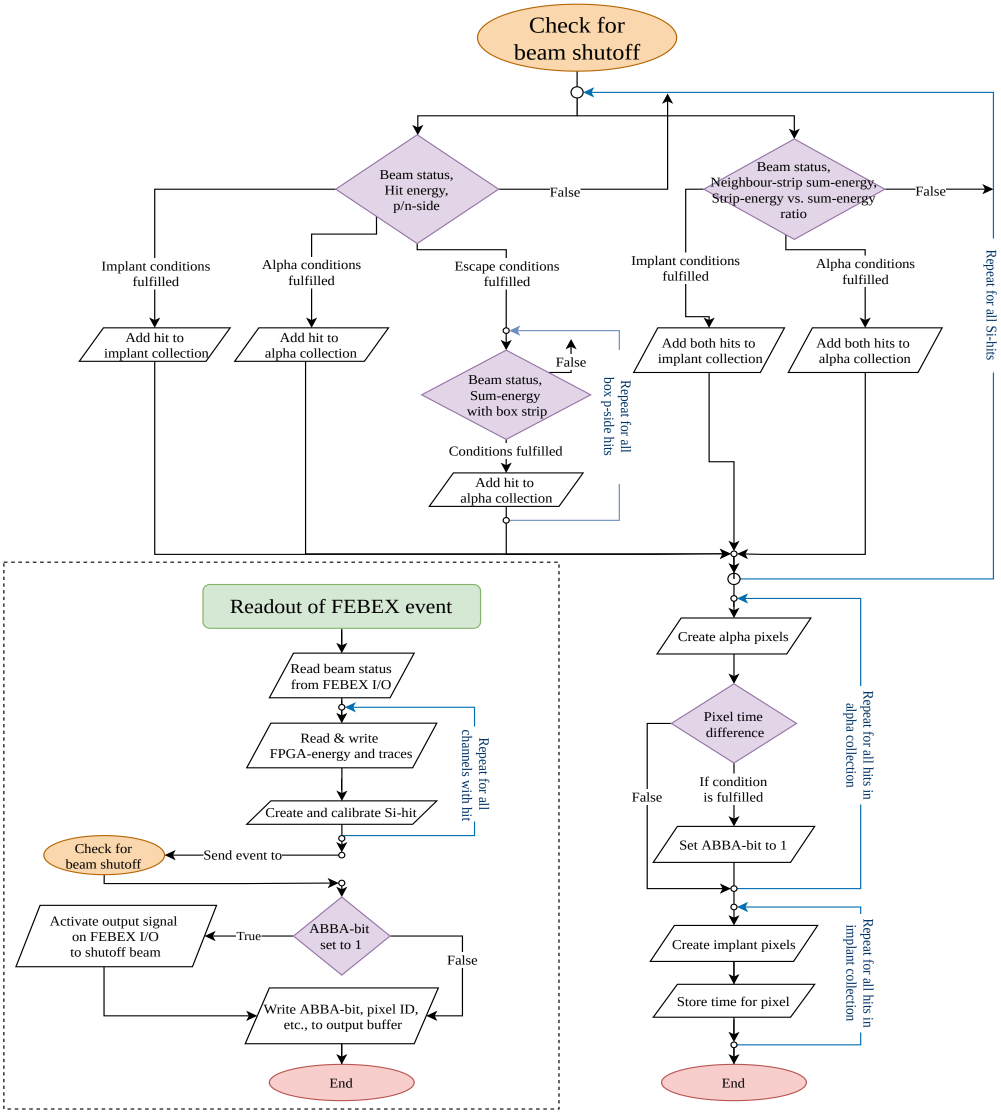

Figure C.1: Diagram showing the readout flow of the beam shut-off routine. The full FEBEX readout routine is depicted at the bottom left, within which the beam shut-off routine is invoked. Decisions are based upon the list of arguments within the diamond shapes. For instance, in the case of α neighbour-strip add-back, conditions with respect to the beam status, the sum energy of the neighbouring strips and the ratio of the individual strip energy versus the sum energy, need to be fulfilled in order to add the strips to the α-candidate collection.

C.2 User parameters

```
*Shutoff parameters for t049 and 288,289,290Fl
*Energies given as calibrated (MeV)
*Times are given as seconds
* -------------------------------------------------------
*
* ### Shutoff durations ###
*
*imp-alpha1 correlation
ia1_shutoff_dur 300.0
*
*imp-alpha1-alpha2 correlation
ia1a2_shutoff_dur 0.0
*
*alpha1-alpha2 correlation
a1a2_shutoff_dur 0.0
* -------------------------------------------------------
*
* ### n-side energy gate scaling factors ###
*
*n_side_scale_factors
n_side_scale_low 0.95 1.05
* -------------------------------------------------------
*
* ### IMPLANT EVENT ###
*
*Implant energy window
IE 11.0 19.0
*
*Implant Strip Sum Ratio
IStripSumRatio 0.2
* -------------------------------------------------------
*
* ### ALPHA1 EVENT - Beam OFF ###
*
* Fl288: E=9.93, T=0.62 s, Fl289: E=9.83, T=2.3 s
*First energy window beam OFF
E1Off 9.5 10.3
*
*First energy window escape alpha, beam OFF
E1esc_Off 0.5 4.0
*
*First energy window reconstructed with box, beam OFF
E1rec_Off 8.5 9.5
*
*Alpha1 Strip Sum Ratio, beam OFF
A1StripSumRatio_Off  0.1
*
*Time window1 imp-alpha1 beam OFF
delta_Tia1OFF  20.0
* -------------------------------------------------------
*
* ### ALPHA1 EVENT - Beam ON ###
*
*First energy window beam ON
E1On 0.0 0.0
*
*First energy window escape alpha, beam ON
E1esc_On 1.0 3.0
*
*First energy window reconstructed with box, beam ON
E1rec_On 8.8 9.5
*
*Alpha1 Strip Sum Ratio, beam On
A1StripSumRatio_On  0.1
*
*Time window imp-alpha1 beam ON
delta_Tia1ON  0.0
*
*Time window imp-alpha1 box summing beam ON
delta_Tia1OB  4.0
```

Appendix D

Identification Efficiency of Fl-decay Chains

In this appendix, decision trees, with which the identification efficiency of Fl-decay chains was determined, are introduced.

The method may be exemplified with Figure D.1[1] which presents the decision tree for the ^{286,288}Fl-decay chains. The top and bottom half of the decision tree depicts *EVR*-α-*SF* scenarios where the recoil (EVR) signal is caught or missed, respectively. At a rate of 45 Hz, during the periods of 5 ms and 15 ms within (Beam ON, 22.5%) and outside (Beam OFF, 77.5%) the beam pulse, 14% and 6% of the events are missed due to dead time, respectively as explained in Sec. III. A, in Paper V. A special case is spontaneous fission (SF) during periods of Beam ON, where instead of 14%, 30% of the events are missed motivated by the more restricted energy conditions applied here. For detected α decays, the full-energy is measured in the cases when the α particle is detected solely in the Imp-DSSD (50%) or through reconstruction when it escapes into a box-DSSD (30%). In the remaining cases (20%), the α particle escapes full detection.

Decay chains of a certain character for which a large number of random chains [Sec. III. D, Paper V] are expected, namely > 0.2, are disregarded. An example of such decay chains is *EVR*-α(Escape, Beam ON)-*SF*(beam ON), and these are marked specifically *disregarded*. Furthermore, all decay chains lacking a spontaneous fission event are disregarded. *Escape* and *Missed* α-decay events are grouped together. This is because both types of events contribute to a similar degree to the number of random chains.

---

[1] Drawn with **draw.io**: `https://drawio-app.com/`

The parameters of the beam shut-off routine, detailed in Appendix C, plays a decisive role. If activated, the routine creates a low-background environment in which it is virtually impossible to miss the fission event. It should further be noted that, during beam-ON periods, restricted energy and time conditions were applied in the beam shut-off routine. This motivates an efficiency for reconstructed events at 80% for the ^{286}Fl- and ^{288}Fl-decay chains while at 60% for the ^{289}Fl-decay chains. The latter is further limited due to longer lifetimes, and in particular in the second α-decay step.

The summary at the bottom right of the figure presents the identification efficiency for scenarios with, missed and detected recoil events, and in total. Figure D.2 holds the decision tree for the ^{289}Fl-decay chains. The identification efficiency of ^{286}Fl- and ^{288}Fl-decay chains at 88% is slightly superior to the ^{289}Fl-decay chains at 85%, despite the latter type of chains including more decay steps. This can largely be attributed to its long lifetimes, as indicated above. It necessitates the disregard of e.g. decay chains of type *EVR*-α(Escape, Beam ON/OFF)-α(Escape, Beam ON/OFF)-*SF*(Beam ON/OFF) due to too many expected random chains. Finally, it is worth noting that the number of missed/detected events due to dead time was determined at relatively high beam intensity ($\sim 3.3\,\mathrm{p\mu A}$ compared to an average of $\sim 2.7\,\mathrm{p\mu A}$ on the Pu target) and it may thus result in an underestimated identification efficiency. For reference, assuming that only 7% and 3% of the events are missed during Beam ON and OFF, respectively, results in an increased identification efficiency from $\sim$ 88% to $\sim$ 92% and from $\sim$ 85% to $\sim$ 88%. This variation lays the foundation for the uncertainties of the final identification efficiencies assigned the ^{286,288}Fl- ^{289}Fl-decay chains, which were modified and set to 90(3)% and 86(3)%, respectively.

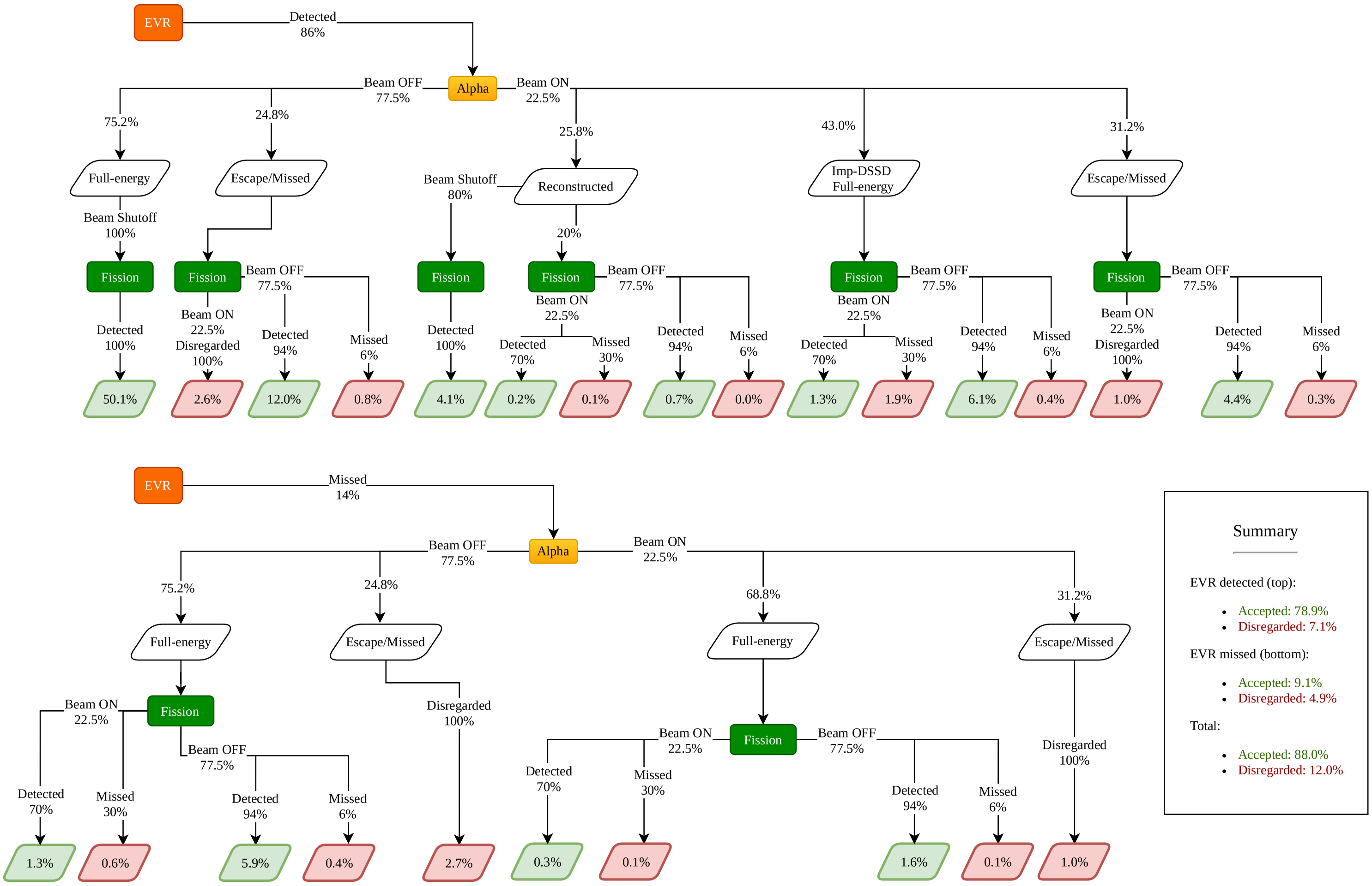

Figure D.1: Decision tree deducing identification efficiency of ^{286,288}Fl -decay chains.

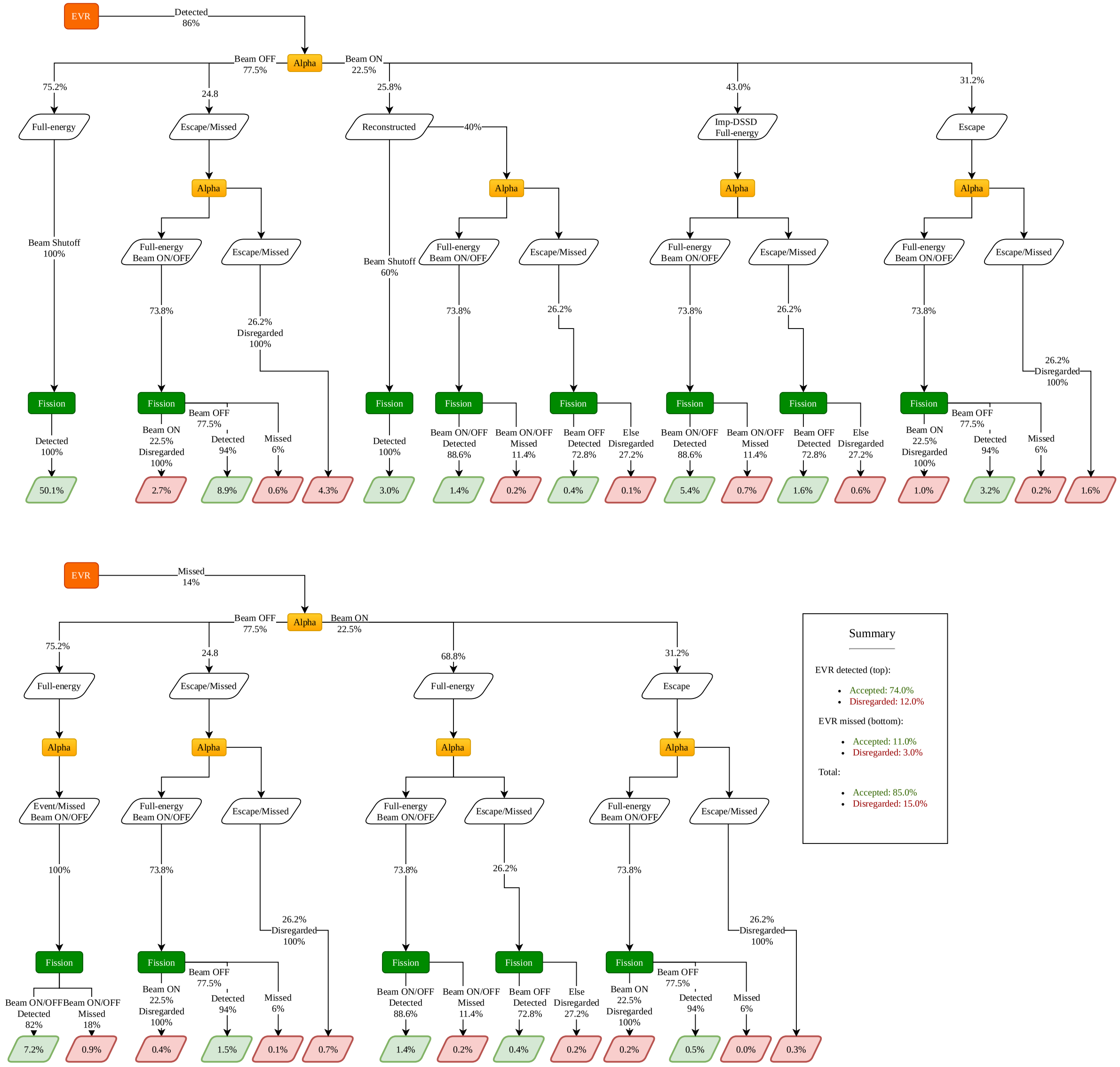

Figure D.2: Decision tree deducing identification efficiency of ^{289}Fl -decay chains.

Appendix E

Trace PDF

Events connecting the recoil implantation event and the fission within an implantation-detector pixel were tracked along all candidate Fl-decay chains. The data, i.e. pulse shapes, hits in the DSSDs and Ge-detectors, and general event information, for all events along a decay chain, was compiled into pdf documents. Six of the chains were missing an recoil implantation event and for these chains a reasonable time window were opened to also view potential recoil implantation candidate events. Figure E.1 depicts an example of an event from these documents where notations are explained. Each event has been assigned a tentative label; None, implant, alpha, escape, or fission.

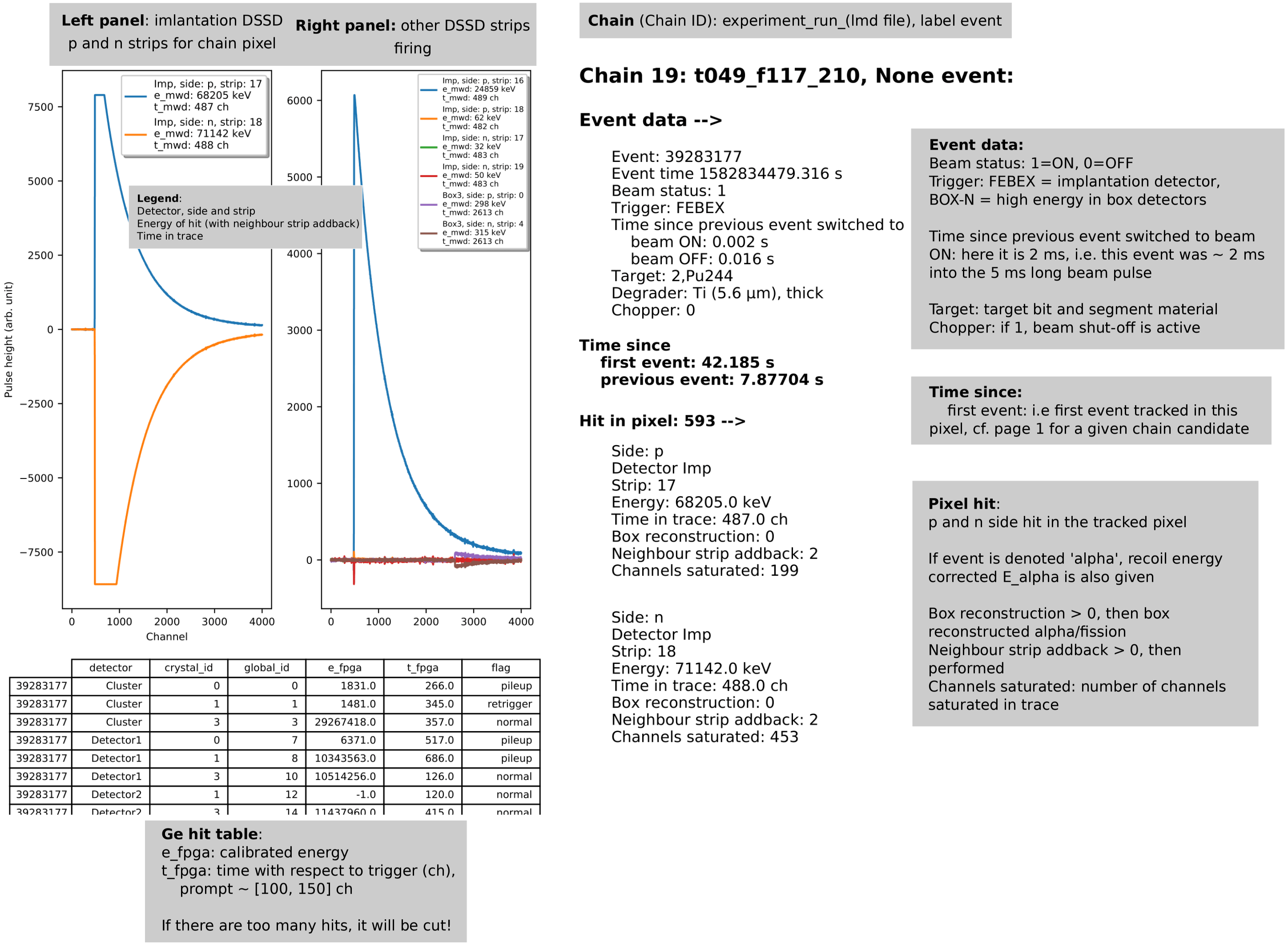

Left panel: imlantation DSSD p and n strips for chain pixel

Right panel: other DSSD strips firing

Legend:
Detector, side and strip
Energy of hit (with neighbour strip addback)
Time in trace

	detector	crystal_id	global_id	e_fpga	t_fpga	flag
39283177	Cluster	0	0	1831.0	266.0	pileup
39283177	Cluster	1	1	1481.0	345.0	retrigger
39283177	Cluster	3	3	29267418.0	357.0	normal
39283177	Detector1	0	7	6371.0	517.0	pileup
39283177	Detector1	1	8	10343563.0	686.0	pileup
39283177	Detector1	3	10	10514256.0	126.0	normal
39283177	Detector2	1	12	-1.0	120.0	normal
39283177	Detector2	3	14	11437960.0	415.0	normal

Ge hit table:
e_fpga: calibrated energy
t_fpga: time with respect to trigger (ch),
prompt ~ [100, 150] ch

If there are too many hits, it will be cut!

Chain (Chain ID): experiment_run_(lmd file), label event

Chain 19: t049_f117_210, None event:

Event data -->

Event: 39283177
Event time 1582834479.316 s
Beam status: 1
Trigger: FEBEX
Time since previous event switched to
beam ON: 0.002 s
beam OFF: 0.016 s
Target: 2,Pu244
Degrader: Ti (5.6 µm), thick
Chopper: 0

Time since
first event: 42.185 s
previous event: 7.87704 s

Hit in pixel: 593 -->

Side: p
Detector Imp
Strip: 17
Energy: 68205.0 keV
Time in trace: 487.0 ch
Box reconstruction: 0
Neighbour strip addback: 2
Channels saturated: 199

Side: n
Detector Imp
Strip: 18
Energy: 71142.0 keV
Time in trace: 488.0 ch
Box reconstruction: 0
Neighbour strip addback: 2
Channels saturated: 453

Event data:
Beam status: 1=ON, 0=OFF
Trigger: FEBEX = implantation detector,
BOX-N = high energy in box detectors

Time since previous event switched to beam ON: here it is 2 ms, i.e. this event was ~ 2 ms into the 5 ms long beam pulse

Target: target bit and segment material
Chopper: if 1, beam shut-off is active

Time since:
first event: i.e first event tracked in this pixel, cf. page 1 for a given chain candidate

Pixel hit:
p and n side hit in the tracked pixel

If event is denoted 'alpha', recoil energy corrected E_alpha is also given

Box reconstruction > 0, then box reconstructed alpha/fission
Neighbour strip addback > 0, then performed
Channels saturated: number of channels saturated in trace

Figure E.1: Compiled event data used to scrutinize events tracked along candidate Fl-decay chains. Notations used are explained.

References

[1] K. Chapman, *Superheavy: Making and Breaking the Periodic Table* (Bloomsbury Sigma, 2019), ISBN 978-1472953896.

[2] Ulrika Forsberg, PhD thesis, Lund University (2016), ISBN 9789176238127 (pdf), `https://lup.lub.lu.se/search/ws/files/7495513/thesis.pdf`.

[3] W.D. Myers and W.J. Swiatecki, Ark. Fys. **36**, 343 (1967).

[4] U. Mosel and W. Greiner, Z. Phys. **217**, 256 (1968).

[5] S.G. Nilsson *et al*, Nucl. Phys. A **131**, 1 (1969).

[6] P.H. Heenen *et al*, Nucl. Phys. A **944**, 415 (2015).

[7] F.P. Heßberger, EPJ Web Conf. **131**, 02005 (2016).

[8] Ch.E. Düllmann, R.-D. Herzberg, W. Nazarewicz, and Y. Oganessian, Nucl. Phys. A **944**, 1 (2015), `https://www.sciencedirect.com/journal/nuclear-physics-a/vol/944`.

[9] D. Rudolph, EPJ Web Conf. **131** (2016), `https://www.epj-conferences.org/articles/epjconf/abs/2016/26/contents/contents.html`.

[10] S. Hofmann, EPJ Web Conf. **131**, 06001 (2016).

[11] K. Morita, Nucl. Phys. A **944**, 30 (2015).

[12] V. Utyonkov *et al.*, EPJ Web Conf. **131**, 06003 (2016).

[13] R.-D. Herzberg and P.T. Greenlees, Prog. Part. Nucl. Phys. **61**, 674 (2008).

[14] M. Asai, F.P. Heßberger and A. Lopez-Martens, Nucl. Phys. A **944**, 308 (2015).

[15] NuDat2 database, *Advanced Cross-Variable Plot*, `https://www.nndc.bnl.gov/nudat2/`.

[16] S. Hofmann *et al.*, Eur. Phys. J. A **48**, 62 (2012).

[17] D. Rudolph *et al.*, J. Radioanal. Nucl. Chem. **303**, 1185 (2015).

[18] M. Block, Nucl. Phys. A **944**, 471 (2015).

[19] Y. Ito *et al.*, Phys. Rev. Lett. **120**, 152501 (2018).

[20] P.T. Greenlees *et al.*, Phys. Rev. Lett. **109** (2012).

[21] R.-D. Herzberg, EPJ Web Conf. **131**, 02004 (2016).

[22] D. Ackermann, Nucl. Phys. A **944**, 376 (2015).

[23] Y.T. Oganessian and V.K. Utyonkov, Nucl. Phys. A **944**, 62 (2015).

[24] Ch.E. Düllmann *et al.*, Phys. Rev. Lett. **104**, 252701 (2010).

[25] U. Forsberg *et al.*, Nucl. Phys. A **953**, 117 (2016).

[26] D. Rudolph *et al.*, Phys. Rev. Lett. **111**, 112502 (2013).

[27] J.M. Gates *et al.*, Phys. Rev. C **92** (2015).

[28] J.M. Gates *et al.*, Phys. Rev. Lett. **121** (2018).

[29] Y. Shi, *et al.*, Phys. Rev. C **90**, 14308 (2014).

[30] L.G. Sarmiento, L.-L. Andersson, and D. Rudolph, Nucl. Instrum. Meth. A **667**, 26 (2012).

[31] K.S. Krane, *Introductory Nuclear Physics* (John Wiley & Sons, 1988), 2nd ed, ISBN 978-0-471-80553-3.

[32] S. Ćwiok, W. Nazarewicz, and P.H. Heenen, Phys. Rev. Lett. **83**, 1108 (1999).

[33] L.-L. Andersson *et al.*, Nucl. Instrum. Meth. A **622**, 164 (2010).

[34] G. Duchêne *et al.*, Nucl. Instrum. Meth. A **432**, 90 (1999).

[35] F.A. Beck, Prog. Part. Nucl. Phys. **28**, 443 (1992).

[36] J. Eberth *et al.*, Prog. Part. Nucl. Phys. **28**, 495 (1992).

[37] T. Kibédi *et al.*, At. Data. Nucl. Data Sheets **98**, 313 (2012).

[38] H. Moseley, Philos. Mag. **26**, 1024 (1913).

[39] A. Såmark-Roth, *Transformation from TASISpec to Lundium* (2020), `https://zenodo.org/record/4011523`.

[40] T. Kibédi *et al.*, Nucl. Instrum. Meth. A **589**, 202 (2008).

[41] G. Gilmore, *Practical Gamma-ray Spectrometry* (John Wiley & Sons, Ltd., 2008), 2nd ed., ISBN 978-0-470-86196-7.

[42] G. Knoll, *Radiation Detection and Measurement* (John Wiley & Sons, Inc., 2000), 3rd ed., ISBN 0-471-07338-5.

[43] S. Akkoyun *et al.*, Nucl. Instrum. Meth. A **668**, 26 (2012).

[44] M.R. Dimmock *et al.*, IEEE Trans. Nucl. Sci. **56**, 2415 (2009).

[45] F. Crespi *et al.*, Nucl. Instrum. Meth. A **593**, 440 (2008).

[46] C. Domingo-Pardo *et al.*, Nucl. Instrum. Meth. A **643**, 79 (2011).

[47] N. Lalović *et al.*, Nucl. Instrum. Meth. A **806**, 258 (2016).

[48] M.-M. Bé *et al.*, *Table of radionuclides. Monographie BIPM-5*, `http://www.lnhb.fr/nuclear-data/nuclear-data-table/`.

[49] D.C. Radford, Nucl. Instrum. Meth. A **365**, 297 (1995).

[50] Daesung Cho, Bachelor thesis, Lund (2019), `http://lup.lub.lu.se/student-papers/record/8984456`.

[51] Y. Hrabar *et al.*, Nucl. Instrum. Meth. A (to be published).

[52] D.M. Cox *et al.*, *UNILAC Proposal: Discovery and Spectroscopy of Neutron-Deficient Pu Isotopes and their Alpha-Decay Daughters* (2020).

[53] D. Rudolph *et al.*, *UNILAC Proposal: Spectroscopy of Flerovium Decay Chains & Discovery of* ^{290}*Fl* (2017).

[54] M. Bender *et al.*, Phys. Rev. C **60**, 034304 (1999).

[55] J. Runke *et al.*, J. Radioanal. Nucl. Chem. **299**, 1081 (2014).

[56] E. Jäger *et al.*, J. Radioanal. Nucl. Chem. **299**, 1073 (2014).

[57] A. Semchenkov *et al.*, Nucl. Instrum. Meth. B **266**, 4153 (2008).

[58] P. Golubev *et al.*, Nucl. Instrum. Meth. A **723**, 55 (2013).

[59] J. Hoffmann *et al.*, GSI Scientific Report, PHN-IS-EE-03 (2011), `https://repository.gsi.de/record/53520`.

[60] H.G. Essel and N. Kurz, IEEE Trans. Nucl. Sci. **47**, 337 (2000).

[61] Johan Jeppsson, Master thesis, Lund University (2012), `http://www.nuclear.lu.se/fileadmin/nuclear/Grundlaeggande/Theses/Jeppsson.pdf`.

[62] J.M. Gates *et al.*, Phys. Rev. C **83** (2011).

[63] A. Yakushev *et al.*, Inorg. Chem. **53**, 1624 (2014).

[64] A. Yakushev, Nat. Chem. **13**, 213 (2021).

[65] Ch.E. Düllmann, EPJ Web Conf. **131**, 08004 (2016).

[66] Anton Roth, Master thesis, Lund University (2016), `http://lup.lub.lu.se/student-papers/record/8882017`.

[67] Y. Ts. Oganessian *et al.*, Phys. Rev. C **70**, 064609 (2004).

[68] Y. Oganessian, J. Phys. G: Nucl. Phys. **34** (2007).

[69] K.H. Schmidt *et al.*, Z. Phys. A **316**, 19 (1984).

[70] J.F. Ziegler, M.D. Ziegler, and J.P. Biersack, Nucl. Instrum. Meth. B **268**, 1818 (2010).

[71] J. Adamczewski-Musch, H.G. Essel, and S. Linev, IEEE Trans. Nucl. Sci. **58**, 1477 (2011).

[72] Christian Lorenz, PhD thesis, Lund University (2019), `https://portal.research.lu.se/portal/sv/publications/quantumstate-selective-nuclear-decay-spectroscopy(b2c3fa5f-2dd0-4182-935e-91019457701f).html`.

[73] J. Theuerkauf *et al.*, Program Tv; Institute for Nuclear Physics, Cologne, `https://www.ikp.uni-koeln.de/~fitz/`.

[74] D. Rudolph *et al.*, Acta Phys. Pol. B **45**, 263 (2014).

[75] Evaluated Nuclear Structure Data File (ENSDF) (2021), `http://www.nndc.bnl.gov/ensdf/`.

[76] F.P. Heßberger *et al.*, Eur. Phys. J. A **48**, 75 (2012).

[77] P. Sigmund, Phys. Rev. A **56**, 3781 (1997).

[78] D. Wittwer *et al.*, Nucl. Instrum. Meth. B **268**, 28 (2010).

[79] M. Wang *et al.*, Chinese Phys. C **41** (2017).

[80] W.D. Myers and W.J. Swiatecki, Nucl. Phys. A **601**, 141 (1996).

[81] Yu. Ts. Oganessian *et al.*, in JINR, E7-2004-160 (2004), p. 128, `http://www1.jinr.ru/Preprints/2004/160(E7-2004-160).pdf`.

[82] D. Kaji *et al.*, J. Phys. Soc. Jpn **86**, 034201 (2017).

[83] P. Möller *et al.*, At. Data. Nucl. Data Sheets **109-110**, 1 (2016).

[84] E. Olsen and W. Nazarewicz, Phys. Rev. C. **99** (2019).

[85] M. Warda and J.L. Egido, Phys. Rev. C **86**, 014322 (2012).

[86] J.L. Egido and A. Jungclaus, Phys. Rev. Lett. **125**, 192504 (2020).

[87] C. Qi *et al.*, Phys. Rev. C **80**, 044326 (2009).

[88] A.N. Andreyev *et al.*, Nature **405**, 430 (2000).

[89] J.M. Yao, M. Bender, and P.H. Heenen, Phys. Rev. C **87**, 034322 (2013).

[90] J. Khuyagbaatar *et al.*, Phys. Rev. Lett. **112**, 172501 (2014).

[91] J. Khuyagbaatar *et al.*, Phys. Rev. C **99**, 054306 (2019).

[92] J. Khuyagbaatar *et al.*, Phys. Rev. C **102**, 064602 (2020).

[93] S. Dmitriev, M. Itkis, and Y. Oganessian, EPJ Web Conf. **131**, 08001 (2016).

[94] W. Barth *et al.*, Proceedings of IPAC2013, Shanghai, China TH-PWO007 (2013), `https://accelconf.web.cern.ch/ipac2013/papers/thpwo007.pdf`.

[95] J. Piot, EPJ Web Conf. **178**, 02027 (2018).

[96] M. Albertsson *et al.*, Eur. Phys. J. A **56**, 46 (2020).

[97] M. Warda, A. Zdeb, and L.M. Robledo, Phys. Rev. C **98**, 041602(R) (2018).

[98] P. Sarriguren, J. Phys. G: Nucl. Part. Phys. **47**, 125107 (2020).

[99] F.P. Heßberger *et al.*, Eur. Phys. J. A **52**, 328 (2016).

[100] F.P. Heßberger *et al.*, Eur. Phys. J. A **52**, 192 (2016).

[101] J. Khuyagbaatar, *Island of the stability: back to the future* (2021), `https://webmaster.ncbj.gov.pl/events/superheavy-elements/program`.

[102] J. Hong, G.G. Adamian, and N.V. Antonenko, Phys. Lett. B **764**, 42 (2017).

[103] A. Lopez-Martens *et al.*, Phys. Lett. B **795**, 271 (2019).

[104] F.P. Heßberger, Eur. Phys. J. A **55**, 208 (2019).

[105] E.L. Brady and M. Deutsch, Phys. Rev. **78** (1950).

Printed by Media-Tryck, Lund 2021 NORDIC SWAN ECOLABEL 3041 0903

Spectroscopy along Decay Chains of Element 114, Flerovium

> "Anders had, for as long as he could remember, dreamed of exploring the world of nuclear physics, that is, the edges of the Chart of Nuclides. He was sitting on the ferry that had just left the harbor on the shores of Lead Peak. The course was aimed for Actinide Island, the starting point for this world's discoverers. His dream was finally about to come true."

And so *Expedition Flerovium* begins. The short popular science story takes you through the highlight of this PhD thesis. In a spectroscopy experiment aiming to study atomic nuclei of element 114, flerovium, new insights were gained into the Island of Stability. This island is a region on the Chart of Nuclides where the possible existence of long-lived superheavy elements has tantalized nuclear physicists ever since the first predictions in the 1960s.

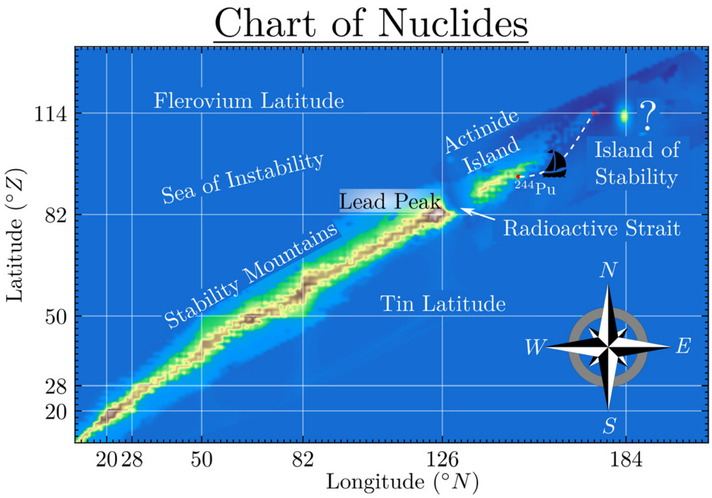

LUND UNIVERSITY

Faculty of Engineering
Department of Physics

ISBN 978-91-7895-835-1